

MEMOIRS
OF THE
FACULTY OF ENGINEERING
OSAKA CITY UNIVERSITY

VOL. 60

DECEMBER 2019

PUBLISHED BY THE
GRADUATE SCHOOL OF ENGINEERING
OSAKA CITY UNIVERSITY

This series of Memoirs is issued annually. Selected original works of the members of the Faculty of Engineering are compiled in the first part of the volume. Abstracts of papers presented elsewhere during the current year are compiled in the second part. List of conference presentations delivered during the same period is appended in the last part.

All communications with respect to Memoirs should be addressed to:

Dean of the Graduate School of Engineering
Osaka City University
3-3-138, Sugimoto, Sumiyoshi-ku
Osaka 558-8585, Japan

Editors

Akira TERAJ

Hayato NAKATANI

Masafumi MURAJI

Daisuke MIYAZAKI

Hideki AZUMA

Tetsu TOKUONO

Toru ENDO

**MEMOIRS OF THE FACULTY OF ENGINEERING
OSAKA CITY UNIVERSITY**

VOL. 60

DECEMBER 2019

CONTENTS

Regular Articles 1

Urban Engineering

Urban Design and Engineering

Current and Future Situations of Automatic Driving in China and Japan

HAINAER BULATAI and Takashi UCHIDA 1

Evaluation of Road Space Reallocation Arrangement and Rest Space Installation for Pedestrians and Cyclists Using the Level of Service Concept on Midosuji Boulevard

Haruka KAWACHI, Nagahiro YOSHIDA, Pola BERENT 13

Vital Reactions as a Measure of Stress Levels in Bicycle Riders According to Degree of Task

Katsumasa TATSUNO and Nagahiro YOSHIDA 19

Abstracts of Papers Published in Other Journals	27
<i>Mechanical and Physical Engineering</i>	
<i>Mechanical Engineering</i>	29
<i>Electronics and Informatics</i>	
<i>Applied Physics and Electronics</i>	38
<i>Electric and Information Engineering</i>	50
<i>Applied Chemistry and Bioengineering</i>	
<i>Applied Chemistry and Bioengineering</i>	52
<i>Urban Engineering</i>	
<i>Architecture and Building Engineering</i>	70
<i>Urban Design and Engineering</i>	73
List of Presentations at International Conferences	85
<i>Mechanical and Physical Engineering</i>	
<i>Mechanical Engineering</i>	87
<i>Electronics and Informatics</i>	
<i>Applied Physics and Electronics</i>	88
<i>Applied Chemistry and Bioengineering</i>	
<i>Applied Chemistry and Bioengineering</i>	92
<i>Urban Engineering</i>	
<i>Urban Design and Engineering</i>	97

MEMOIRS
OF THE
FACULTY OF ENGINEERING
OSAKA CITY UNIVERSITY

VOL. 60

DECEMBER 2019

PUBLISHED BY THE
GRADUATE SCHOOL OF ENGINEERING
OSAKA CITY UNIVERSITY

Current and Future Situations of Automatic Driving in China and Japan

HAINAER BULATAI* and Takashi UCHIDA**

(Received October 31, 2019)

Synopsis

Conducting social acceptance surveys in Japan and China requires understanding of the current situation of automatic driving technology and the difficulties posed by transmission of future technologies. To analyze the status quo and to assess differences in automatic driving in China and Japan, this research begins with assessment of the three basic technologies of automatic driving. Then identification technology, programming technology, and control technology are analyzed by comparing the equipment of intelligent auxiliary systems of companies in China, Japan, and the United States. By analyzing the current state of development, the company plans can indicate the future of automatic driving.

KEYWORDS: Automatic driving, Control, Planning, Recognition technology, V2X

1. Research Background

Transportation services have evolved over time and have greatly affected people's lives and urban activities. Automatic driving technology, including artificial intelligence technology, is expected to be realized in the future. Most fatal accidents result from driver error. The practical use of automatic driving is therefore expected to reduce driver-related traffic accidents considerably. Two main types of automatic driving technologies are expected to reduce traffic congestion and to strengthen international competitiveness. "Automatic" driving uses sensors and cameras attached to the car while sensing pedestrians and obstacles, along with road surface information such as roads, signs, and signals. "Infrastructure cooperation" can hold the city together and protect safety.

Comparison of self-regulated cars developed by Alphabet Inc. and Uber Technologies Inc. shows that the coordination type is more dependent on the construction of infrastructure. Smart city infrastructure is being built in several countries. Shanghai particularly has launched a new smart city construction policy. Current automatic driving technologies cannot cope with complex traffic conditions. All problems cannot be solved by each vehicle. Therefore, automatic driving technology and transportation systems should be regarded together. In economically developed countries, road development and infrastructure development are fundamentally completed. Maintenance is almost impossible. Viewed in that light, infrastructure development has not been completed in China and other intermediate countries that are expected to realize "automatic" automatic driving. Nevertheless, in China, where there is a demand for urban development, it is reportedly more efficient to develop it as a set with automatic operations as a whole. Furthermore, using not only visual information such as green and red traffic lights, but also information such as signal change timing and road congestion, vehicles will be able to adjust speed efficiently. The best automatic driving technology method must be chosen based on infrastructure development and road development in Japan and China.

2. Research Purpose and Method

By grasping the main technologies for automatic driving, technologies that can be realized in 10 years are

* Student, Master Course of Department of Urban Engineering

** Professor, Department of Urban Engineering

predicted by the roadmap of companies in Japan and China. For different regions in Japan (city, region) and China (observation, center, northwest region), infrastructure development, inputs of social capital, traffic demand, etc. can be predicted. Future difficulties posed by dissemination of automatic driving technology are forecast. Future studies will administer social acceptance surveys of Japan (city, region) and China (coastal, central, and northwest) after assessment of the current status of automatic driving technology and difficulties faced by future technology transmission. For this study, based on the present circumstances in each country¹⁾⁻³⁾, literature search, and analyses of the automatic driving technology used by each company⁴⁾⁻¹⁰⁾, the potential for future systems is predicted.

3. Main Technology of Automatic Driving

The automatic driving system senses the surrounding environment of the vehicle based on the environment sensing technology, and independently controls the steering and speed of the vehicle through the vehicle center computer according to the information obtained by the sensing, so that the vehicle can safely and reliably travel and reach the predetermined destination.

The key technologies of automatic driving are recognition technology and control technology. Recognition technology is the basis of driverless driving. Vehicle control technology is the core of driverless driving, including trajectory planning and control execution. The two technologies complement each other to form the key technology of intelligent driving vehicles. The system composition is shown in Figure 1.

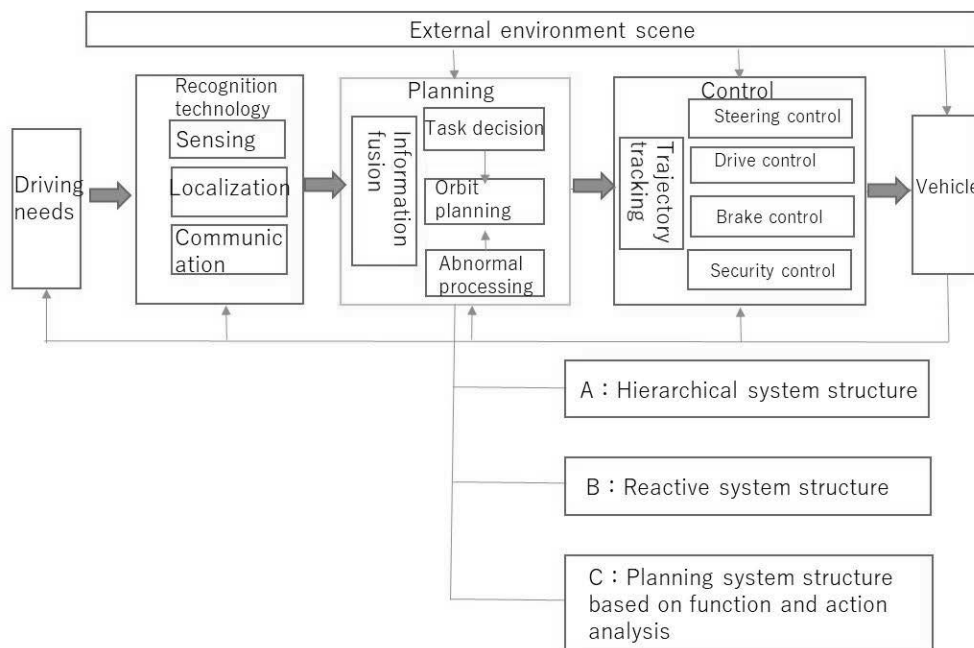


Figure 1: Overall relevance of automatic driving technology.

3.1 Recognition technology

Automatic driving technology acquires and processes environmental information mainly for state recognition and V2X (Vehicle-to-everything .communication is the passing of information from a vehicle to any entity that may affect the vehicle, and vice versa. It is a vehicular communication system that incorporates other more specific types of communication as V2I (vehicle-to-infrastructure), V2N (vehicle-to-network), V2V (vehicle-to-vehicle), V2P (vehicle-to-pedestrian), V2D (vehicle-to-device) and V2G (vehicle-to-grid).) network communication, which uses the latest communication and network technology to enable information sharing, interconnection, and control coordination between automatic vehicles and external infrastructure and equipment. State recognition collects and processes ambient and local environmental information via onboard sensors, mainly including traffic conditions and vehicle conditions.

Realization of a traffic condition recognition function depends on the sensors and corresponding detection technologies. Depending on how the traffic environment information is obtained, these sensors are classifiable into two types:

- 1) Passive environmental sensors do not emit signals themselves, but instead receive environmental information by receiving external reflections or radiated signals including cameras, visual sensors, and acoustic sensors such as microphone arrays.
- 2) Active sensors such as radar, millimeter wave radar, and ultrasonic radar, and active environmental sensors actively transmit signals to the external environment for environmental sensing.

Realization of the vehicle state detection function is based mainly on global position systems (GPS) such as the Beidou Navigation Satellite System, and Inertial Navigation System. These devices are designed to obtain information such as vehicle speed and attitude orientation and to provide effective data for automatic vehicle position and navigation.

3.1.1 Camera

Vision sensors used in automatic driving are mainly industrial cameras, which present important advantages over consumer cameras, such as high image stability, transmission capabilities, and interference prevention capabilities. According to the output data signal, industrial cameras can be analog or digital. Depending on the chip type, they are classifiable as charge-coupled device (CCD) cameras and complementary metal oxide semiconductor (CMOS) cameras. Visual sensing technologies are classifiable into three main types as presented in Table 1.

Table 1: Features using visual sensing technology of three types

Technology	Principle Application	Main Technology	Benefit	Shortcomings
Monocular vision technology	<ul style="list-style-type: none"> ▪ Lane positioning, ▪ Road shape identification, detection of obstacles such as surrounding vehicles and pedestrians ▪ Identification of traffic lights and traffic signs 	<ul style="list-style-type: none"> ▪ Lane detection and tracking technology ▪ Obstacle detection and tracking technology ▪ Traffic signal and traffic sign recognition technology, ▪ Vision-based SLAM technology ▪ Visual odometer technology 	<ul style="list-style-type: none"> ▪ Simple structure, ▪ Mature algorithm ▪ Less computation 	<ul style="list-style-type: none"> ▪ Cannot get depth information of limited recognition range and scene target
3D recognition technology	<ul style="list-style-type: none"> ▪ To restore a 3D scene, two (or more) cameras use the same object from different viewpoints by calculating misalignment with the image pixels 	<ul style="list-style-type: none"> ▪ Camera calibration, ▪ Image matching ▪ Obstacle detection 	<ul style="list-style-type: none"> ▪ Traditional calibration method, active visual calibration method, and self-calibration method 	<ul style="list-style-type: none"> ▪ Difficult to find matching points in multiple camera images
Omnidirectional visual technology	<ul style="list-style-type: none"> ▪ Camera rotation method ▪ Fisheye lens method ▪ Spherical mirror method ▪ Conical mirror method 	<ul style="list-style-type: none"> ▪ Single camera 360° rotation imaging, ▪ Fisheye camera imaging, multi-camera stitching imaging ▪ Panoramic reflection imaging 	<ul style="list-style-type: none"> ▪ Wide imaging field of view 	<ul style="list-style-type: none"> ▪ Large image distortion and low resolution

3.1.2 Radar

The radar sensor (Table 2) generally includes a transmitter, transmission antenna, receiver, reception antenna, display, and processing unit. It also includes auxiliary devices such as a power supply devices, data recording devices, and interference prevention devices.

Table 2: Features of Radar

	Work range	Benefits	Shortcomings
Laser radar	Infrared and visible light bands	<ul style="list-style-type: none"> High resolution, good concealment, strong interference, excellent directivity Long measurement distance Short measurement time 	<ul style="list-style-type: none"> Technical limits and High costs With severe attenuation in harsh environments such as clouds, rain and snow.
Millimeter wave radar	Millimeter wave band with a frequency of 30–300 GHz	<ul style="list-style-type: none"> Compact, lightweight, high resolution Powerful anti-interference capability Easy installation Accurately measure the target relative distance and relative speed. 	<ul style="list-style-type: none"> Millimeter waves are an important radar band.
Ultrasonic radar	Mechanical frequency band, frequency exceeding 20 kHz	<ul style="list-style-type: none"> Strong penetrability Low attenuation. It is useful to identify objects that are insensitive to light and color and which have low transparency and diffuse reflectance. Suitable for environments that are not sensitive to external electromagnetic fields. Its electromagnetic interference principle is simple. The production is convenient. The cost is low. Marketing is easy. 	<ul style="list-style-type: none"> Vulnerable to bad weather. The distance measurement speed cannot be compared with photoelectric distance measurements or millimeter wave radar distance measurements. The direction cannot be measured. The application field is limited.

3.1.3 Positioning and navigation technology

Automatic driving is based on automatic navigation. It obtains the relative positional relation between the vehicle and the external environment. It is also necessary to ascertain the absolute position of the vehicle through recognition of the vehicle state.

Position data of an automatic driving vehicle cannot exist independently of the recognition condition benchmark (generally designated as a coordinate system). The vehicle positioning performance results corresponding to different benchmarks are vastly different. Standards often used for automatic driving include geodetic coordinate system (WGS-84 / CGCS 2000), camera coordinate system, image coordinate system, radar coordinate system, and driver recognition coordinate systems. After the benchmark is selected, information such as the vehicle orientation, ambient environment, and map are mapped and marked. One or more maps based on these coordinate systems are generated. In these drawings, the driving situation map based on the driver's cognitive coordinate system can reflect the selection attention, and can move in synchronize with the vehicle.

Most current automatic driving uses GPS / BDS + INS in combination because traffic environments are complex and variable. Single navigation systems are often limited by their own flaws: they cannot guarantee accurate positioning and navigation.

3.1.4 V2X and 5G

Vehicle to Everything (V2X) network communication connects vehicles, roads, and users, mainly using radio frequency identification (RFID), cameras, and cloud servers to improve driving safety and driving efficiency. Consequently, traffic information such as road conditions, road information, and pedestrian information are interchangeable.

The V2X network communication technical capabilities used for automatic driving are short network access time, low transmission delay, high transmission reliability, low interference, high information security, and spectrum

reusability. In addition, large amounts of data must be analyzed and processed. To do so, sensors of different types must be used rationally with V2X technology to elucidate rules from data we have acquired for effective representation.

Realization of V2X technology is generally based on hardware platforms such as RFID, camera equipment, and vehicle sensors. The V2X network communications industry is divided into two standards and industry camps: Dedicated Short Range Communication and LTE-V2X technology (Table 3).

Table 3: Features of DRSC and LTE technologies

Technology	Key indicators	Benefits	Shortcomings
DSRC	Vehicle speed	200 km/h	<ul style="list-style-type: none"> ▪ Mature technology ▪ Coverage is narrow ▪ Data transfer rate is low, ▪ Packet loss rate is high, ▪ High-speed analysis of large amounts of data is difficult ▪ Large amounts of infrastructure is required (RSU) ▪ High course
	Reaction time	100 ms	
	Data transfer rate	12 Mbps (up to 27 Mbps)	
	Delay	20 ms	
	Transfer range	Hundred meters (cheap obstacles)	
	Broadband	75 MHz	
LTE-V*(5G)	Vehicle speed	500 km/h	<ul style="list-style-type: none"> ▪ Low infrastructure maintenance course, wide coverage, ▪ Fast data transfer rate ▪ Low packet loss rate, from working 4G network infrastructure to 5G
	Broadband	100 Mhz	
	Data transfer rate	500 Mbps – 1 Gpbs	
	Delay	10 ms or less (Yosa surface) 50 ms or less (Control surface)	
	Transfer range	Large	

3.2 Planning technology

Planning technology, a direct representation of automated driving intelligence, plays a decisive role in driving safety and performance. Planning technologies includes hierarchical, responsive, and hybrid types (Table 4). Figure 2 portrays the relations among A, staged system structure, B, reactive system structure, and C, hybrid system structure.

Automatic driving planning technology is at the heart of automatic driving. Improper driving decisions affect the safety, energy saving, and comfort of the car itself, reducing external traffic flow efficiency. National and international scholars have achieved some results with vehicle intelligent driving planning methods based on environmental information and vehicle conditions. The systems can cope with complex and dynamic actual traffic scenarios.

Development and integration of an automatic planning system are divisible into four transaction loops each. They can perform information fusion, task specification, track specification, and anomaly handling.

Table 4: Features of the respective types of planning technology

	Structure	Superiority	Inferiority
Hierarchical type	Tandem system structure	Easy to achieve planned reasoning ability and high standards	Sensor demand has high delay, lack of real-time, unreliable
Reactive type	Parallel structure	Easy and flexible transition of the entire system from low to high levels	Difficult to predict overall system behavior. Less advanced information is available.
Hybrid type	Combining hierarchical architecture and reactive architecture	Combined effectively	Technology is immature

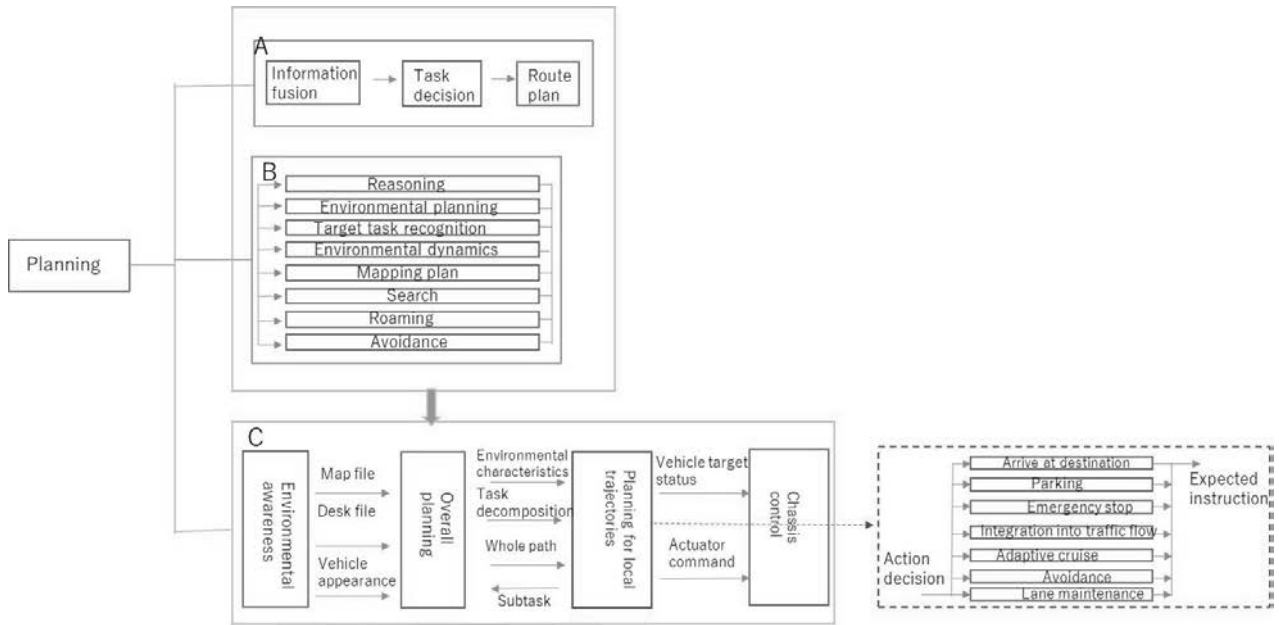


Figure 2: Planning technology structure.

Planning is the basis for automatic driving navigation and control. From the perspective of trajectory determination, it is divisible into two levels: global planning and local planning. The task of global planning is to plan a path that can be passed without collision from the starting point to the target point according to the global map database information. Because the route generated by the overall route plan cannot be a rough route from the starting point to the target point, automatic driving does not incorporate consideration of details of direction, width, curvature, road crossings, or obstacles. It is affected by the local environment while driving. Effects of its own state uncertainty will encounter various unmeasured conditions. Therefore, the automatic driving process requires ideal local path planning without collision based on local environmental information and its own state information.

Depending on the driving environment characteristics, key points and difficulties in local path planning of automatic driving differ.

- 1) On the highway, the vehicle driving environment changes slowly, but demands high accuracy. Automatic driving vehicle control is easy. A main problem is the speed algorithm, which can obtain environmental information and position accuracy of route searching.
- 2) On urban roads, the road environment is more complicated, but the traffic environment is more complex and more obstacles exist nearby. Therefore, to identify the functions and obstacles of smart car roads, requirements will be higher. Path planning is necessary mainly for modeling the environment surrounding the vehicle and for obstacle avoidance, especially for dynamic obstacle direction and speed prediction.
- 3) On non-separated roads with an off-road environment, no clear road boundary exists in the environment where smart cars are located. The roads are wavy and might have large pits and mounds. An important requirement is identification of areas that are accessible by the vehicle.

3.3 Control technology

Key technologies for automatic driving are environment recognition technology and vehicle control technology. Environment recognition technology is the foundation of driverless operation. Control technology is the core of driverless operation including trajectory planning and control execution. These two technologies complement each other to form key technologies for automatic vehicles. The system configuration is shown in Figure 3. The automatic driving process is divisible into three parts.

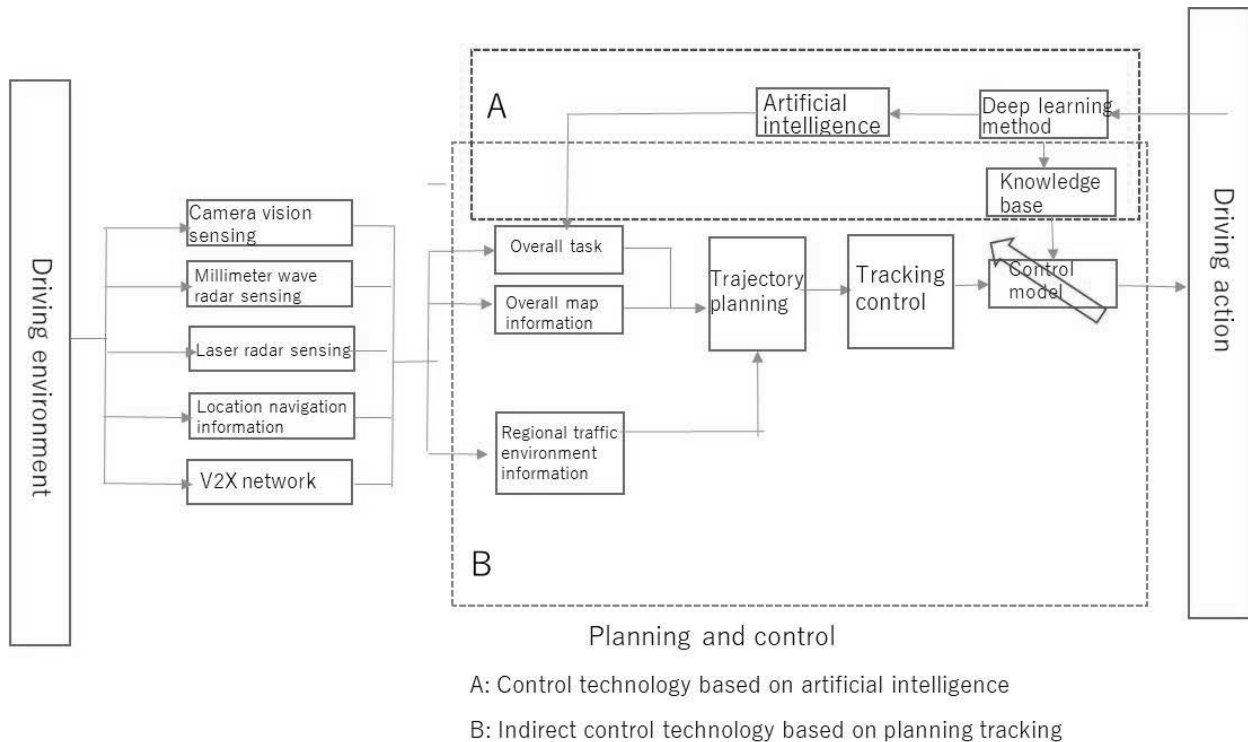


Figure 3: Structure of control technology.

- 1) External environment is recognized by radar, camera and vehicle network connection system
- 2) Based on intelligence sensing fusion information, we learned external scenes through intelligent algorithms. Information, vehicle trajectory planning, vehicle anthropomorphic control to traffic flow,
- 3) Tracks the planning trajectory targets, controls the drive movement of the vehicle's throttle, brakes and steering, adjusts the vehicle's running speed, position and direction, etc. to ensure vehicle safety, operability and stability.

Overall, the process tracks the planning trajectory targets, controls the drive movement of the vehicle's throttle, brakes, and steering, and then adjusts the vehicle's running speed, position, and direction to ensure vehicle safety, operability, and stability.

The core technology for automatic driving control is vehicle longitudinal and lateral control technology. Longitudinal control requires vehicle drive and brake control, lateral control, i.e. steering wheel angle adjustment and tire force control. Automatic vertical and horizontal control are implemented to control driving of the vehicle automatically with given targets and constraints.

Artificial intelligence based control technology uses artificial intelligence to establish a direct mapping process from driving environment to driving behavior. Specifically, an advanced driver model to complete the actual driving process is established within the cognitive range. The control process need not establish a mathematical model of the controlled object. It has strong mobility and real-time performance.

The vehicle front–rear control is control of the travel speed, i.e., control in a direction in which the distance between the vehicle speed and the front and rear vehicles or obstacles is controlled automatically. Cruise control and emergency brake control are examples of automatic driving vertical control. Control difficulties of this type can be attributed to the control of motor drives, engines, transmissions, and brake systems. Different motor engine transmission models, vehicle motion models, and brake process models are combined with different controller algorithms to form different vertical control modes.

4. Current Situations and Roadmaps of Automated Driving in Japan, China, Europe, and the United States

4.1 Current status of support driving systems in Japan, China and Europe, and the United States

Automatic driving technology requires various corresponding systems to be configured on a smart car to achieve its complex functions.

When regarding the overall level, driving support level 2 is currently at the center, but among them, one can find that it is the current stage in which automatic driving systems of level 3 or higher related to 17) FSDC are beginning to appear (Table 5 & 6).

Table 5: List of automatic driving support systems.

V2X Identification technology	V2P Vehicle to Pedestrian	V2V Vehicle to Vehicle
①LDW (Line departure warning lane departure warning device) * (LDA)	⑨PPS (person protection system, pedestrian protection system)	⑪FCW (front collision warning forward collision warning)
②LKA (Lane Keep Assist Lane Maintenance Assist)	⑩DMS (Driver Monitor System)	⑫TJA (traffic jam assist system)
③AEB (automatic emergency braking) * (ABA)		⑬ACC (Adaptive Glue Control adaptive driving control) * (DRCC)
④BSD (Blind Spot Detection) * (BSM)		⑭RCTA (Backward crossing detection) * (CTA)
⑤SVA (side view assist)		⑮ALC (Automotive Line Change Assist System)
⑥APS (automatic parking system)		⑯TRT (Title recognition technology)
⑦AFS (adaptive front lighting system, adaptive front lighting) * (AHB)		⑰SLA (Intelligent Speed Limit Assist)
⑧NVS (Night Vision System, Night Lighting Support System) * (PCS)		⑱FSDC automatic operation system

Table 6: Driver manufacturer's equipment support system.

		Identification technology					Pedestrian & driver safety		Driving safety										
		LDK	LKA	BSD	AEB	SVA	APS	NVS	AFS	PPS	DMS	FCW	TJA	ACC	RCTA	ALC	TRT	SLA	FSDC
China	FAW Group (Red Flag)	△	○	△	△					△	△	△	△	○	○	○	○	○	
	SAIC Group (Shanghai)	○		△			○	△				○	○	○	○	○	○	○	
	Dongfeng Motor	○	○	△	○		○	△				△	○	○	○	○	○	○	
	Changan Automobile		△	△	○							○	○	○	○	○	○	○	
	Guangzhou Automobile			△		△	△												
	Great Wall Motor Haval	○	○			○	○			○									
	Chery Automobile	△				△						△							
	Geely Automobile	△						○				○	○	○	○	○	○	○	
	BYD					○				○									
	Xiaopeng Automotive	○		○	○							○	○	○	○	○	○	○	
NIO	△		△	△		△		△			△	△	△		△				
Japan	Toyota	○	○	○			○					○	○	○	○	○	○		
	Honda	○	○	○			○		○			○	○	○	○	○	○		
	Nissan	○	○	○	○				○			○	○	○	○	○	○		
	Fuji Heavy Industries	○	○	○	○				○			○	○	○	○	○	○		
	Mazda	○	○	○	○				○			○	○	○	○	○	○		
American, European	Shanghai VW	○					○			○	○	○	○	○	○	○	○		
	FAW VW			○								○	○	○	○	○	○		
	Audi										○	○	○	○	○	○	○		
	Mercedes-Benz				○						○	○	○	○	○	○	○	○	
	Dongfeng Pojo		○								○	○	○	○	○	○	○	○	
	Dongfeng Citroen	○				○						○	○	○	○	○	○		
	General Motors	○	○									○	○	○	○	○	○		
	Ford		○	○	○	○			○			○	○	○	○	○	○		
	Tesla	△	△	△			△				△	△	△					△	

○: Option △: Basic

The respective companies have realized different driving support systems, but system implementation is continuing under various conditions. Technologies are not perfect. Moreover, functions such as ABE have limitations in inter-vehicle distance control depending on circumstances. Many functions of APAS might not be disabled depending on the road conditions, vehicle conditions, weather conditions, even if the ACC function is used in limited areas on expressways and motorways. Although driving support system vehicle technology is incomplete, Chinese, Japanese, and American companies are working actively on improving them. Among them, some development models such as those for Tesla and NIO vehicles are considering automatic support system as basic car functions. However, regarding the status of the overall automatic support system development, the development center of Japanese and Chinese companies will depend on the respective company technologies and respective country policies. Presumably, safety will be the primary consideration in Japan.

4.2 Automatic driving roadmap organization of China, Japan, and the United States.

4.2.1 China

The Chinese government will gradually support the standardization and independence of the automatic driving technology industry. However, the government's policy is put forth in the literature particularly highlights integration of communication technology and manufacturing industry in a new era. According to a plan proposed in April 2017 <Automotive Industry Medium- to Long-Term Development Plan>, in 2020, more than 50% of cars are equipped with driving assistance (DA) partial automated driving (PA), or conditional automated driving (CA) systems. The installed cars (about 10%) might be accelerated by the explosive development of automatic driving technology.

Chinese cities are experiencing severe traffic congestion because of increased car ownership, irregular driving habits, and reduced vehicle usage. Commuting is inefficient and congestion-inducing, with great amounts of time spent in traffic and parking. Automated driving with intelligent networking can free up driving time, optimize the use of road resources, and smooth road traffic. New car sales in China account for a large share of new car sales worldwide. Therefore, technology can be promoted easily. Changes might be more acceptable for internet vehicles in areas where the mobile internet is developing rapidly in China

China is more likely than other mature market countries to use mobility services. The use of mobility services has changed consumers' traditional views of car ownership. Chinese consumers are expected to accept self-driving cars readily. However, public awareness of automatic driving remains low. Few automobile technology enthusiasts are strongly interested in automatic driving. Technologies must be launched widely. Safe driving and "The Dolly Problem" with a conservative attitude are the main reasons for refusal of automatic driving.

Table 7: Automatic driving roadmap organization of China.

	2000	2003	2006	2011	2012	2013	2014	2015	2016	2017	2018	2019	2020	2025
FAW Group	● B12020 self-driving car			● Hongqi HQS unmanned vehicle	● 286 km high-speed full-range unmanned experiment						● Qing Jui 2.0 project	● Automatic parking ● Platooning ● Hongqi HT, Jiefang planned to be commercialized	● Mass production of Hongqi "E · Border" ● City operation	● L4 penetration rate is over 50%
Great Wall Motor				● Automated driving team ● Haval HS, H9 ● Driving assistance ● ADAS stage									● Mass production of autonomous vehicles	● L2 autonomous driving market
Baidu				● Baidu self-driving car project	● City automatic driving loop automatic driving ● Autonomous highway driving (demonstration experiment) ● Maximum speed 150km/h						● Automated driving on limited area expressways ● Autonomous driving on city roads		● Automated driving on the entire highway ● Autonomous driving on city roads	
SATIC				● Intelligent driving car ● IGS	● Cloud automotive application			● Promotion of services			● OTA Online System Update	● Super Cruise	● Mass production of Baidu, JAC intelligent vehicles	● Fully automatic operation ● AR augmented reality technology ● L4 fully automatic operation ● Industrial application
Changan Automobile				● Intelligent strategy "6 S 4" ● 5 basic technology system platform ● Five core application technologies ● Single intelligence car				● 2,000 kilometers unmanned long distance test			● L2 automatic mass production (first company in China)	● Changan Huawei Joint Innovation Center (SG-V2X)	● Mass production of L3 autonomous vehicles	
Beijing Automotive Group								● 5G-based autonomous driving vehicle ● NOVA_Pilot1.0 * (L1)			● NOVA_Pilot2.0 * (L2)		● NOVA_Pilot3.0 * (L3) ● SG-V2X * (2020)	● NOVA_Pilot4.0 * (L4)

4.2.2 Japan

In Japan, the future needs of a mobile society are classified roughly into large urban areas, suburbs, local cities, and depopulated areas. In large urban areas, public transportation is expected to be developed further. Suburbs and smaller cities present possibilities for practical use, such as driverless ride sharing and driverless taxis. Door-to-door transportation methods are used mainly for personal cars, with travel to school, work, hospitals, and shopping for everyday life. In less populated areas, practical application of low-speed automatic driving buses and driverless taxis can be considered in cooperation with local governments.

In Japan, networks, intelligence, and road safety concepts are integrated. The plan is divided into three stages: driving assistance, V2X, and the realization of three stages of more advanced road safety.

The period of 2020 to around 2025 represents the first stage of introduction of automatic driving vehicles. Presumably, automatic driving vehicles and general vehicles will use public roads simultaneously. The share of automatic driving vehicles is expected to be small.

Table 8: Automatic driving roadmap organization of Japan.

	2000	2003	2006	2011	2012	2013	2014	2015	2016	2017	2018	2019	2020	2025
Fuji Heavy Industries		EyeSight ght3.0		SI-Cruise									L2 automatic driving eyesight*	L4 automatic driving system
Toyota					Ha: mo (share car)					MSPF (share service)	Preventive safety package "Toyota Safety Sense" "Lexus Safety System+" "TRI-Advanced Development (TRI-AD)" Truck platooning on a highway		L4 automatic driving on highways L3 automatic driving system for exclusive road 2020: "Highway Teammate" put into practical use. Commercialization of "Urban Teammate" DSRC system (America 2021)	L4 automatic driving on general roads
Nissan									ProPilot*		Autonomous highway driving C-V2X demonstration experiment	5G NR	ProPilot 3.0* (L3) Automatic driving in general road-limited areas (L3) Highway self-driving car (L4)	L4 automatic operation (2022)
Mazda											ACTIVESENSE* (AFS, HBC, MRCC, RVM, LDWS, FOW) Mazda co-pilot concept* autonomous driving demonstration experiment		Mazda Co-Pilot Concept*	Implementation of Mazda Co-Pilot Concept*
Honda											Honda SENSING (L2)		Highway self-driving car (L4)	L4 automatic driving

4.2.3 United States and Europe

In the United States, the government management system is decentralized. The legal environment is moving forward. The US traffic management system is managed by many state and local governments. Over the past two years, 23 states in the United States have introduced Driving Laws, The 5 states have adopted automatic driving laws. The US Road Traffic Safety Administration Safety Rules are an approximation of the management system. The United States has adopted administrative law that establishes Federal Automobile Safety Standards.

Those standards facilitate mandatory installation of vehicle DSRC (Dedicated Short Range Communications). The Highway Safety Authority has established a transportation change research center to establish self-driving car guidelines and policy frameworks and to facilitate demonstration testing. The HSA has a comprehensive layout from strategy, legislation, and testing levels. Current traffic laws in the United States prohibit self-driving cars that are not equipped with steering wheels and brakes.

Gaining passenger confidence is important for expanding the acceptance of general automatic vehicles. The Intel Automatic Driving Improvement Report states that when people's trust is reflected in the experience of trust and human interaction with computers, people will make a big difference in machine safety and trust.

Table 9: Automatic driving roadmap organization of Europe and the United States.

	2000	2003	2006	2011	2012	2013	2014	2015	2016	2017	2018	2019	2020	2025
Alphabet Inc.					Fleet* 480,000 kilometers			Autonomous driving mileage 1 million kilometers		Fully automated driving test	Weimo's experimental mileage is 8 million kilometers	Running computer simulation about 8 billion kilometers	Lidar sensor sales	
Tesla							Lane change on the Autopilot Expressway	Enhanced Auto Parallel	Automatic parking	Public road demonstration	C-V2X experiment		Equipped with level 4 automatic driving hardware	
Ford														Mass production of L4 automatic driving (ride sharing and taxi) (2021)
General Motors											Cadillac CT6	BOLT Ev* (Ride Share Business)	Public road demonstration of V2V technology	Cruise self-driving commercial applications
ZMP Inc.												Automated driving taxi operation (demonstration experiment)	Automatic taxi	Realization of MaaS

5 Conclusions

As described herein, countries are preparing actively for automatic driving in terms of policy and economy transformation, new energy vehicle creation, and favorable conditions establishment for automatic driving. The likely roadmaps of that development seem clear.

In the 2020s, automatic driving on highways will be possible. The adoption of safe driving support systems and the spread of 5G and V2X can reduce traffic accidents considerably.

In the 2030s, all of the following can be expected: automatic driving on general roads, widespread use of cars equipped with automatic driving systems, exclusive road traffic flow control for automatic driving vehicles, elimination of traffic congestion, improved punctuality of movement, reduction of resources related to movement, and fewer traffic accidents. Great progress can be expected, especially with smart cities. With the realization of a mobile society centered on vehicles equipped with automatic driving systems in the 2040s and the development of automatic driving technology, the structure of society is expected to change dramatically.

References

- 1) Seio Nakajima, Takehide Takahashi, Hideo Kobayashi: Current state and issues of automatic driving 2018, Shakaihyoronsha Co. Ltd.(2018) (In Japanese).
- 2) Automotive Jobs American Automobile Manufacturers: Latest automatic driving / ADAS development / installation trend, <https://automotive.ten-navi.com/article/30474/> (2018.11.21) (In Japanese).
- 3) Chinese Artificial Intelligence Society: China Artificial Intelligence Series White Paper Smart Driving 2017 (In Chinese).
- 4) Toyota Motor homepage <https://toyota.jp/index.html>
- 5) Guangzhou Honda, homepage <https://www.ghac.cn/>
- 6) Dongfeng homepage <https://www.dfmc.com.cn/>
- 7) Nissan, homepage <https://www.nissan.co.jp/>
- 8) Mazda homepage, <https://www.mazda.co.jp/>
- 9) Ford, homepage <http://www.ford-service.co.jp/>
- 10) Tesla homepage https://www.tesla.com/ja_jp/models

Evaluation of Road Space Reallocation Arrangement and Rest Space Installation for Pedestrians and Cyclists Using the Level of Service Concept on Midosuji Boulevard

Haruka KAWACHI*, Nagahiro YOSHIDA**, Pola BERENT***

(Received October 31, 2019)

Synopsis

The road space reallocation project on Osaka's main street, Midosuji, started in 2017 to realize the concept of human-centered urban spaces in response to the change of social trends and conditions. The pilot project has been undertaken to increase spaces for pedestrians and cyclists. While the "Level of Service" concept was widely employed to evaluate user comfort issues in the transportation field, it is unknown whether it could apply to these space differences and evaluate the reallocation effect correctly. In this study, we show the elements that are not expressed by the Level of Service and are directed towards a more realistic comfort assessment; for example, rest spaces in road designs, and the expected and necessary speed to avoid worsening traffic flow.

Keywords: Pedestrian transportation plan, bicycle transportation plan, Road space reallocation, Level of service, Comfort, Rest space

1. Research Background and Objectives

In recent years, waning interest in owning a car has been observed among young people, along with its use as a mode of urban transport. The reason is, the youth generally demonstrate lower interest in cars. Moreover, people are relatively more concerned of their environmental impact and in addition, they have more interest in healthy activities. This shift has generated a renewed emphasis on walking and cycling activities. On Central Midosuji Boulevard in Osaka, noticeable changes have been observed since it was built decades ago, in the ways people behave in relation to it and also in the state of the surrounding areas. To reorganize Midosuji in accordance with this changing social situation and the needs of the time, a pilot project is undertaken to close one side of the street, widen the sidewalk, and build a bike lane (Figure 1). This place-making project is initiated to consider the comfort of users and to incorporate pedestrian-centric ideas, with the latter guided by the principle of transforming a car-centric streetscape into a human-centric one¹⁾.

Level of Service (LOS) is used as an index to express the comfortability of this kind of space for transportation; the U.S. Highway Capacity Manual²⁾ (HCM) defines six LOS grades, on the scale of A to F (A represents the best and F represents the worst). However, limiting the consideration to factors related to transportation may not adequately represent the comfortability of a mixed-use space such as Midosuji, with broad spaces for commingled pedestrians and cyclists, which has other spatial features that relate to its changing streetscape and appeal as a place for leisure.

For this study, we focused on road space reallocation and the effect of a rest space on the sidewalk. A direct survey was conducted of pedestrians and cyclists traversing on broad pedestrian-oriented road spaces of Midosuji, with an objective to evaluate the effects of this streetscape reallocation on both groups in terms of transportation, space, and passers-by, using the concept of service levels. Thereby, proposing the place-making elements will further improve the comfortability when the pilot-project segment is extended in the future.

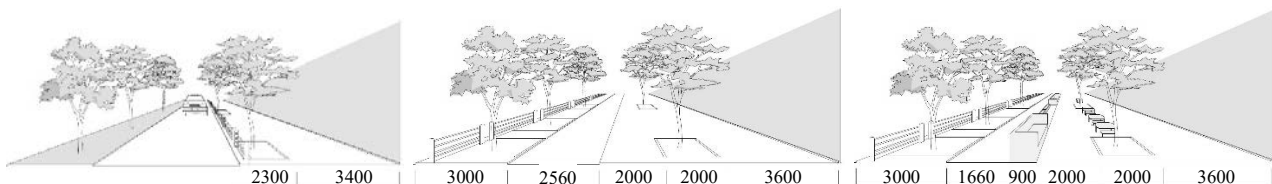


Figure 1: Road space reallocation overview

* Student, Master Course of Department of Civil Engineering

** Associate Professor, Department of Civil Engineering

*** Visiting PhD Student (JSPS Fellow), Centre for Urban Sustainability and Resilience, Department of Civil, Environmental and Geomatic Engineering, University College London

2. Research methodology

2.1. Survey overview

To understand the comfortability of pedestrian spaces of Midosuji, Osaka, Japan, we performed surveys on pedestrians and cyclists on three sections: (a) narrow section, (b) wide section without rest space, and (c) wide section with rest space (Table 1). To calculate LOS and assess the traffic situation, a video-based study was conducted, and a questionnaire was administered to gather subjective assessments. Table 3 shows key elements of the questionnaire used for analysis.

Table 3 shows the breakdown of the width of pedestrian and cyclist spaces in each target sections. Figure 2 shows the personal information of the questionnaire survey for pedestrians and cyclists and traffic volume for pedestrians and cyclists on the survey date.

Table 1: Survey overview

	(a) narrow section	(b) wide section without rest space	(c) wide section with rest space
Questionnaire survey	2017/07/22 (SAT) 9:00–19:00 2017/08/04 (FRI) 13:00–19:00 2017/08/05 (SAT) 13:00–19:00	2017/07/22 (SAT) 9:00–19:00 2017/08/04 (FRI) 13:00–19:00 2017/08/05 (SAT) 13:00–19:00 2017/12/03 (SUN) 11:00–19:00	2017/11/19 (SUN) 11:00–19:00
Video survey	2017/07/22 (SAT) 9:00–19:00	2017/07/22 (SAT) 9:00–19:00 2017/12/03 (SUN) 11:00–19:00 ※ to calculate LOS, we use the data on 12/3.	2017/11/19 (SUN) 11:00–19:00
Subject	Pedestrians: n=84 Cyclists: n= 8	Pedestrians: n=93 Cyclists: n=14	Pedestrians: n=79 Cyclists: n=11
Traffic volume at peak hour	Pedestrians: 3,248 p Cyclists: 69 bicycles [The following include cyclists traffic volume on roadway] Cyclists: 213 bicycles	Pedestrians: 3,316 p Cyclists: 316 bicycles [The following include cyclists traffic volume on roadway] Cyclists: 358 bicycles	Pedestrians: 2,727 p Cyclists: 300 bicycles [The following include cyclists traffic volume on roadway] Cyclists: 321 bicycles

Table 2: Contents of Questionnaire survey

Question	Methodology on answer
Comfortability when traveling	1, 2, 3, 4, 5, 6 (6 levels)
Importance (whole road)	space, safety, speed, length of road, other users, surroundings 1, 2, 3, 4, 5, 6 (6 levels)
Importance (road elements)	path width, verge width, lighting, users speed, volume of pedestrians, volume of cyclists path maintenance, street furniture, surroundings 1, 2, 3, 4, 5, 6 (6 levels)
Rest space	I am more comfortable / I am less comfortable / my comfort is unaffected (3 levels)
Expected speed	same as now / slower than now / faster than now (3 levels)

Table 3: Breakdown of streetscape breadth in target segments

		(a) narrow section	(b) wide section without rest space	(c) wide section with rest space
Path width [m]	Sidewalk	3.4 (not separate)	7.6	5.6
	Bicycle lane		2.6	1.7
	Rest space	-	-	2.9
	Trees	2.3	3.0	3.0
	Walkable path width	3.4	10.2	7.3
	Total width	5.7	13.2	13.2

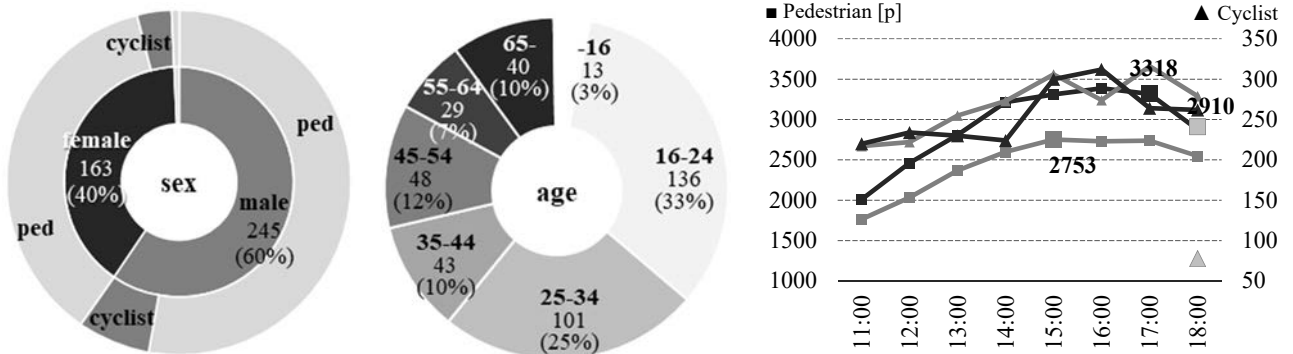


Figure 2: Personal information of questionnaire survey and traffic volume for pedestrians and cyclists

2.2. Analysis methodology

In the questionnaire survey, which serves as subjective indices, respondents scored comfortability on a 6-point scale (1 being very uncomfortable and 6 being very comfortable).

For objective indices, we used the LOS of HCM, which rates density, flow rate, speed, and number of congestion events on each 10-minute peak (Table 4). However, we used the formula based on research by H. Yamanaka et al.³⁾ to calculate pedestrian density. In addition, we used cyclists overtaking pedestrians or pedestrians passing each other as the number of congestion events.

The peak time for (a) according to the “Midosuji Pilot Project Study of Cyclist & Pedestrian Traffic Volumes”—which was conducted by the city of Osaka in November–December 2016 and referenced a post-improvement study near the pilot segment used in this study—is 18:30–18:40. Peak times in (b) and (c) were initially measured as 11:00–19:00 for pedestrian and cyclist traffic volume; subsequently these were measured as 17:00–18:00 for (b) and 15:00–16:00 for (c), and from them, the peak time for (b) is 17:00–17:10 and for (c) is 15:00–15:10.

Table 4: Video analysis method for calculating pedestrian LOS

	(a) narrow section	(b) wide section without rest space	(c) wide section with rest space
Time	18:30–18:40	17:00–17:10	15:00–15:10
Density [p/m ²]	area: 3.4m(width)×4.5m (length) calculated every 30 seconds	area: 5.8m (width)×17.55m (length) calculated every 30 seconds	
Flow rate [p/min/m]	calculated every 1 minute		
Speed [m/s]	area: 4.5m (length) calculated the passing time for 30 seconds every 2 minutes and calculated the average	area: 17.77m (length) calculated the passing time for 30 seconds every 1 minute and calculated the average	
The number of congestion events [events/h]	$F_p = Q_{sb}(1 - \frac{S_p}{S_b})/PHF, F_m = Q_{ob}(1 + \frac{S_p}{S_b})/PHF, F = F_p + 0.5F_m$ <p>F: total the number of congestion events [events/h], F_p, F_m: number of passing / opposing events [events/h], Q_{sb}, Q_{ob}: bicycle flow rate in the same /opposing direction [bicycles/h], S_p, S_b: mean pedestrian /bicycle speed on the path [m/s], and PHF: peal time factor (=0.83) calculated the number of congestion events by using Flow rate and speed</p>		

3. Survey results

3.1. Subjective assessment

3.1.1 Comfort

Figure 3 shows the comfort score for pedestrians and cyclists. Going from segment (a) to (b), the width of the sidewalk affected the comfort score for pedestrians, raising it from 3.46 to 4.10; going from segment (b) to (c), the presence of inviting features slightly increased the score from 4.10 to 4.22. In the HCM, LOS is determined based on the assumption that wider roads increase comfort; while (a) and (b) reflect that trend, (b) and (c) show that comfort can be increased by the presence of inviting features, even when the width is reduced.

For cyclists [(a) to (b)] the width of the sidewalk affected the score, raising it from 2.63 to 3.86; going from segment (b) to (c), the presence of inviting features slightly decreased the score from 3.86 to 3.73. It was greatly affected by the decrease in the path width.

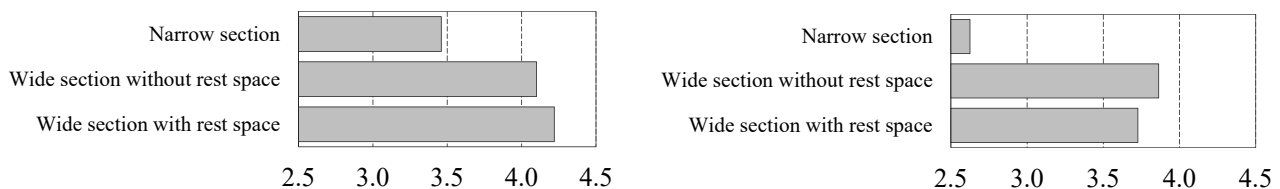


Figure 3: Left; Comfort score for pedestrians (n=369), Right; score for cyclists (n=41)

3.1.2 The factors affecting subjective comfort

Figure 4 shows the importance of factors contributing to comfortability. We can say the following.

Pedestrians:

- The whole road; from the top “safety,” “space,” “surroundings”
- Road elements; “path width,” “volume of pedestrians,” “volume of cyclists,” “surroundings”
- Pedestrians do not feel important about speed elements (e.g. The whole road; “speed,” road elements; “users speed”), however LOS includes the elements.

Cyclists:

- The whole road; from the top “safety,” “space” “other users”
- Road elements; “path width,” “volume of pedestrians,” “volume of cyclists,” “path maintenance”
- Cyclists do not feel important about all elements, except for some, on section (b).

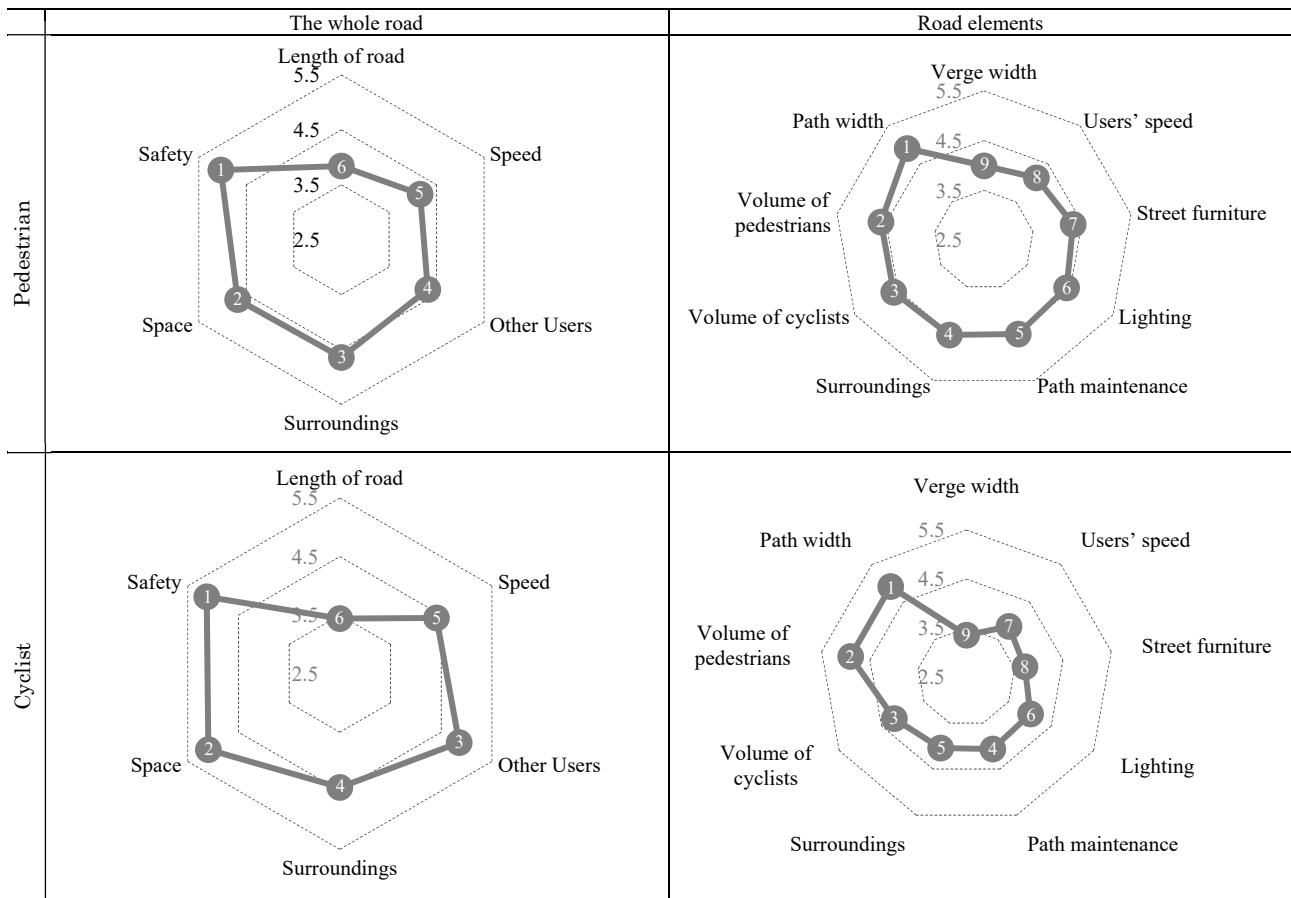


Figure 4: Importance of factors contributing to comfortability; pedestrians; n=370, cyclists; n=39

3.1.3 The rest space

Figure 5 shows the comfort on installing rest spaces. We presented the respondents with the following question: “For each factor below, please rate its importance for your comfort when traveling on a mixed/segregated shared path.” For pedestrians, by installing the rest space on the sidewalk, the answer “I am more comfortable” increases 31.0 points from 24.7 to 55.7%, and the answer “I am less comfortable” decreases 15.2 points, going from 21.5% to 6.3% ($t=-4.61^{**}$, $df=170$). While for cyclists, the answer “I am more comfortable” slightly increases from 16.7% to 27.2% and the answer “I am less comfortable” is almost unchanged from 25.0% to 27.2% ($t=0.27$, $df=21$, ns), and the answer “my comfort is unaffected” is nearly half the answers on both sections.

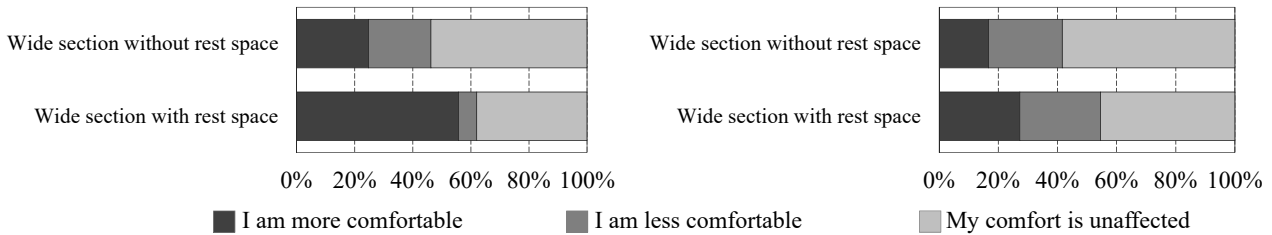


Figure 5: Comfort on installing rest spaces; pedestrians; n=172, cyclists; n=23

3.1.4 The expected speed

Figure 6 shows the expected speed when pedestrians and cyclists are traveling. We presented the respondents with the following question: “What is the speed you want to pass?” For pedestrians, the answer is almost unchanged in the three sections. [(a)(b) $t=-0.38$, $df=270$, ns , (a)(c) $t=0.44$, $df=156$, ns , (b)(c) $t=0.93$, $df=268$, ns] While for cyclists, the answer “Same as now” decreases gradually [(a) 87.5%→(b) 40.9%→(c) 36.4%], and the answer “Faster than now” increases gradually [(a) 12.5%→ (b) 27.3%→(c) 45.5%]. However, no significant difference is found in any sections because of fewer answers [(a)(b) $t=-0.16$, $df=24$, ns , (a)(c) $t=-1.95$, $df=15$, ns , (b)(c) $t=-1.45$, $df=25$, ns].

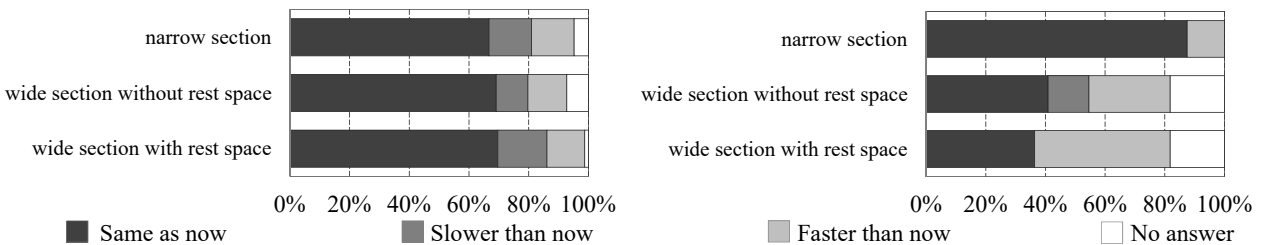


Figure 6: Changing of the expected speed; pedestrians; n=370, cyclists; n=41

3.2. Objective assessment

Figure 7 shows the average LOS scores, based on different criteria, and the LOS rank from HCM. We can say the following.

(a)(b):

- density improved in the LOS rank, however, flow rate and the number of congestion events remained at the rank of A, and the speed was considerably worse compared to other criteria.
- in the LOS score, all of criteria except the number of congestion events improved the traffic flow, in particular, flow rate improved from 14.3p/min/m to 5.8p/min/m.

(b)(c):

- the increase in the number of passing/opposing events resulted in a decrease in the LOS rank, i.e., from B to C, and lower speeds resulted in a further decrease in its rank, i.e., from C to D. The other criteria remained at the rank of A.
- in the LOS score, traffic flow conditions deteriorated in all criteria.

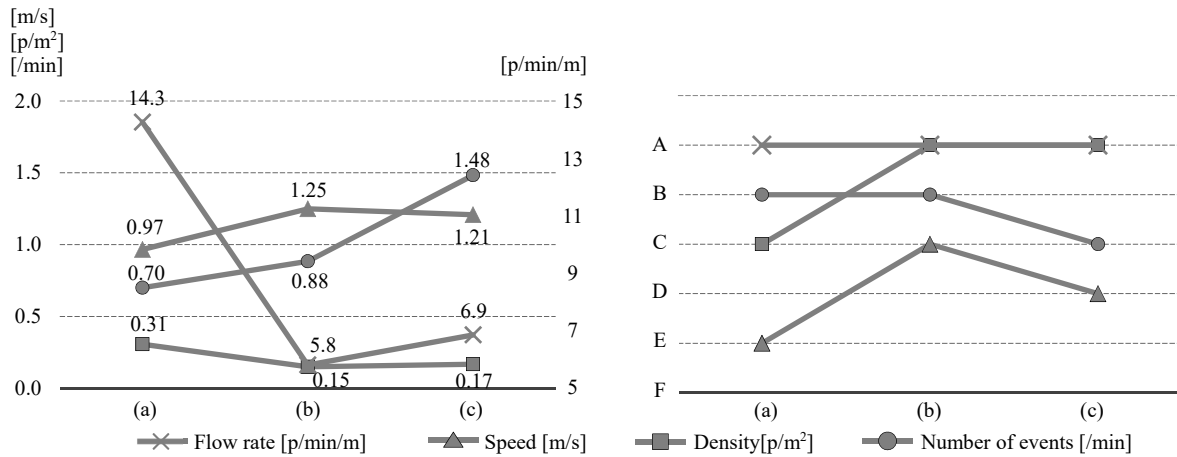


Figure 7 (Left) LOS scores, (Right) LOS rank

4. Discussion

For pedestrians from subjective comfort, they feel more comfort by installing rest spaces even if the path width narrowed. From objective comfort, however, the LOS rank and score did not improve and some criteria worsened.

Regarding the importance of factors contributing to comfortability, pedestrians feel important about the criteria included in the LOS (e.g. space, volume of pedestrians and cyclists), while not about speed; in other words, the feeling did not change by widening the path width and installing a rest space. We focused on the expected speed, but we could not confirm the change in feelings.

For cyclists from subjective comfort, they feel both comfortable and uncomfortable by installing rest spaces. The change in the traffic flow by changing path width influences on the comfort for cyclists, unlike pedestrians. The trend is also significant in the importance of factors contributing to comfortability; it can be said that there is the most comfort in section (b), since the importance is low at (b) where the path width is the widest. Regarding the expected speed, cyclists cannot surpass their expected speed step by step from (a) to (c); it is one of the factors indicating the least comfort, but it is not significant. Then, in section (a), cyclists can pass their expected speed. This was the reason why they passed the roadway at the peak time. However, we questioned cyclists who passed on the sidewalk (if they felt uncomfortable on the sidewalk, they would pass on the roadway).

5. Conclusions

This study shows that, for pedestrians, essentially for broad mixed-use spaces (as in Midosuji Boulevard, Osaka) are essentially for pedestrians and cyclists, and that there is some consistency between subjective and objective evaluations by road width widening, but there is not that by installing rest spaces. Because Due to of this, the LOS criteria from the Highway Capacity Manual cannot completely express user comfortability. For cyclists, however, traffic flow ion their passing space more influences on their comfort more than the road design, and they want to pass faster.

Further study needs to be done to improve the LOS by incorporating the effects of the rest space and the expected speed.

References

- 1) Osaka City Construction Bureau Road Department (2017) "About the pilot project for the road space reallocation of the Midosuji" <http://www.city.osaka.lg.jp/kensetsu/page/0000378248.html>
- 2) Highway capacity manual 2016 : TRANSPORTATION RESEARCH BOARD, National Research Council.
- 3) H. Yamanaka, Y. Handa and Y. Miyagi (2003) "Evaluation method of shared use of bicycles and pedestrians using near-miss index and proposal of its' Level-of-service" Proceedings of JSCE, 730, pp. 27-37
- 4) Y. Tanaka, M. Asano (2011) "Study on the effect of bicycle traffic about the service level on walking space" Civil Engineering Planning Research 44th Annual Meeting
- 5) F. R. Sutikno, Surjono, and E. B. Kurniawan (2013) "Walkability and pedestrian perceptions in Malang City emerging business corridor" Procedia Environmental Sciences, 17, pp. 424-433
- 6) Arunabha Banerjee, Akhilesh Kumar Maurya, Gregor Lämmel (2018) "A Review of Pedestrian Flow Characteristics and Level of Service over Different Pedestrian Facilities" Collective Dynamics Vol.3

Vital Reactions as a Measure of Stress Levels in Bicycle Riders According to Degree of Task

Katsumasa TATSUNO* and Nagahiro YOSHIDA**

(Received October 31, 2019)

Synopsis

In this study, the amount of stress felt by bicycle riders is analyzed to obtain a method for measuring the relationship between the stress factors of the rider and the rider reaction to the environment, particularly while riding in bike lanes. Several vital reaction indices are used in a variety of traffic environments with differing stress factors. This study examines individual differences to include the level of riding experience and complexity of bicycling tasks to better explicitly consider the differences in experience related to stress and the complexity of riding in each environment. We also compare the differences in the vital reaction by the influence of individual based on biking experience and complexity of biking tasks. Results indicated that during a ride in the bike lanes, multitasking induced higher values in all indices of vital reactions, compared with the responses recorded under single-task conditions. It was also found that the vital reactions in subjects who rode their bikes daily tended to be higher under all biking conditions compared with the reactions of those who rode bikes only occasionally.

KEYWORDS: Bicycle, Stress, Vital Reaction, RRI, Biking Task

1. Introduction

Bicycles have become a popular means of transportation owing to their excellent mobility, contribution to reducing the environmental load, and positive impact on rider health. There are various types of bicycle lanes on sidewalks and roadways that separate or share the space with other modes of traffic. Because of the variation in the biking skill of individual riders, the usage rate of bike lanes varies from one type of bicycle lane to another. How the rider evaluates the environment influences whether or not the rider feels comfortable riding their bicycle; thus, it is essential to consider the subjective and objective assessment of the rider when examining what makes a traffic lane desirable from the rider point of view. Previous studies have shown that safety, stress, and the level of comfort for bicycle riders affects their choice of lanes. Research has evaluated stress reactions in the traffic lane by measuring the heart rate variability interval (RRI), galvanic skin response (GSR), and electroencephalogram (EEG) when riding a bicycle, driving a car, or walking²⁾, and there is also research using electromyogram (EMG) for stress measurement in the medical field⁴⁾. This research has provided established data of rider reaction during bicycle operation as a stress reaction using various indices.

However, cycling requires physical activity performed under complex task conditions. Previous studies have shown that personal attributes, such as gender and the presence or absence of knowledge regarding traffic rules, affect the selection of a traveling lane from the various types of bicycle traffic lanes⁶⁾ available. Furthermore, when riding a bicycle, the person who rides the bike simultaneously processes many other tasks; requirements will change significantly depending on the road surface condition and road outline of the selected lane. It is expected that the biking task is closely related to the psychological load of the person when riding a bicycle; thus, there is a need to evaluate rider reaction comprehensively, including the degree of the biking task, the conscious ability of the rider, and riding confidence. However, few research examples capture the interaction between rider reaction, factors in the traffic environment, and rider knowledge.

In this study, to obtain essential knowledge regarding the method of measuring the relationship between stress factors and reactions related to bicycle use, RRI, EMG, and GSR are measured in multiple traffic situations with different biking tasks and stress factors. Then, by conducting a comparative analysis of the rider reaction during bicycle operation and the degree of riding skill required in each traffic situation, it was experimentally examined whether evaluation of the usage environment was possible using a vital reaction index.

* Student, Master Course of Department of Urban Design and Engineering

** Associate Professor, Department of Urban Design and Engineering

2. Definition

2.1 Definition of stress

Stress is generally defined as a “non-specific vital reaction caused by an external stimulus”. At present, the positive aspects of stress are also of interest, as moderate stress has the effect of increasing energy, increasing clarity, and helping the person under stress to understand the situation more accurately⁷⁾. In this study, we defined all vital reactions caused by physical and psychological loads during bicycle operation as stress reactions, considered the influence of the biking environment on riders as external stimuli, and examined the relationship between them.

2.2 Definition of biking task

Bicycle riders handle many tasks when traveling in a bicycle lane. When the traffic lane changes, the types and number of functions required for the bicycle rider differ, and it is expected that they will appear as a vital reaction on the load on the rider.

Therefore, in this study, we defined a biking task as the workload required to travel in each lane when riding a bicycle. The workload is the total amount of external conditions and demands that act to change the physiological and psychological state of a person⁸⁾. In the experiment, the degree of a biking task was expressed as an experimental factor that characterized the complexity of the task. For instance, in a closed space, simple tasks can be performed without the effect of external factors; however, tasks performed on actual roads, where there are various external factors, require greater complexity.

2.3 Overview of vital reaction index

(1) Autonomic nervous system

The autonomic nervous system controls functions essential for life support, such as blood circulation, respiration, and body temperature regulation, and is composed of a sympathetic nervous system and a parasympathetic nervous system. The sympathetic nervous system works to increase the activity level and athletic ability of the body, and functions mainly when it is active, nervous, and stressed. Reactions caused by sympathetic nerves include an increase in heart rate and blood pressure, increase in blood flow to muscles due to contraction of peripheral blood vessels, improvement in oxygen uptake capacity due to a rise in the respiratory rate, and increase in sweat on the palms and soles of the feet.

(2) Heart rate variability interval (RRI)

Heart rate variability represents the variation in the range between the R-waves of the electrocardiogram. When the RRI is reduced more than usual, stress is considered to be occurring.

(3) Electromyogram (EMG)

The electromyogram detects a slight change in potential difference occurring in the muscle, and the amplitude fluctuation of the myoelectric becomes more significant than usual during a stress reaction. The electromyogram waveform is composed of a positive waveform and a negative waveform with the baseline as the boundary; however, to facilitate understanding during analysis, RMS waveform processing is performed to reverse the negative waveform and display it as a positive waveform.

(4) Galvanic skin response (GSR)

The galvanic skin response is an electrical change that occurs temporarily on the skin due to sweating or similar due to a strong stimulus or mental activity. If the value increases, stress is considered to be occurring. In general, an electrode is often placed on the fingertip with the highest concentration of sweat glands to measure this response.

2.4 Overview of measuring equipment

As a measuring instrument, a biology sensor manufactured by S&ME (Fig. 1) was used to measure the RRI, EMG, and GSR of the subject while riding a bicycle. The heart rate sensor electrode was attached to the chest, and the sweat sensor electrode was attached to the index finger and ring fingertips. After a simple experiment to compare reaction due to exercise and stress reduction, the masseter muscle of the masticatory muscle was selected among five muscle candidates, and the electrode attachment of the myoelectric sensor was placed. The measurement interval of each sensor was measured at 0.5 s intervals for RRI and 0.001 s intervals for

EMG and GSR, and recorded in the data logger.

3. Experimental

3.1 Outline of biking experiment

A biking experiment was conducted to compare the electrode mounting positions and examine how the vital reaction index reacts to biking tasks. The subjects were five male students with different bicycle riding experiences (2 daily riders, 3 non-daily riders), and the experimental course was divided into two routes—simple path and complex path (real road). The experimental course (Fig. 2) used for the simple biking task was set up in a university without the influence of other traffic. The experimental course (Fig. 3) used for more complex biking was a 1.5km long course composed of a bicycle track and a shared-use path on an actual road, set in Sakai City, Osaka Prefecture. The width of each lane is 1.1m on the bicycle track and 1.35m on the shared use path with visual separation⁹⁾. The biking experiment on the campus was conducted on January 16, 2018, and the experiment on the actual road was held on January 25, 2018. At the time of measurement, to set the vital reaction in the exercise state to a reasonable value, the resting state for 5 minutes and the bicycle running state for 3 minutes were measured for a specific time, then, the measurement was performed on the course.

3.2 Analysis method

This study demonstrates that by using individual differences in biking experience and complexity of biking tasks you can see how they relate to stress and the complexity of the task required for different environments. This study compared the differences in vital reactions by the influence of individual differences, such as biking experience and sophistication of biking tasks. A comparison was performed using the mean value and variance value of each vital reaction. Here, the variance represents the fluctuation range of the vital reaction.

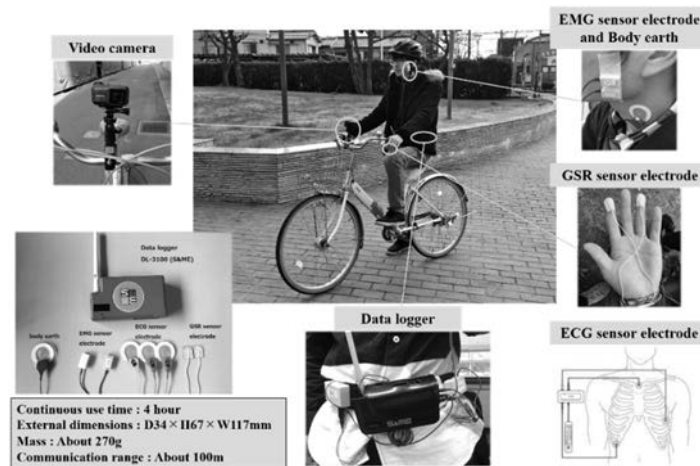


Figure 1. Measuring equipment

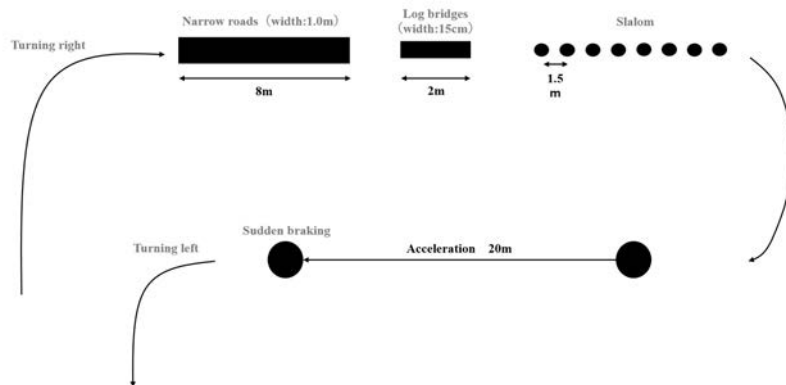


Figure 2. Experimental courses

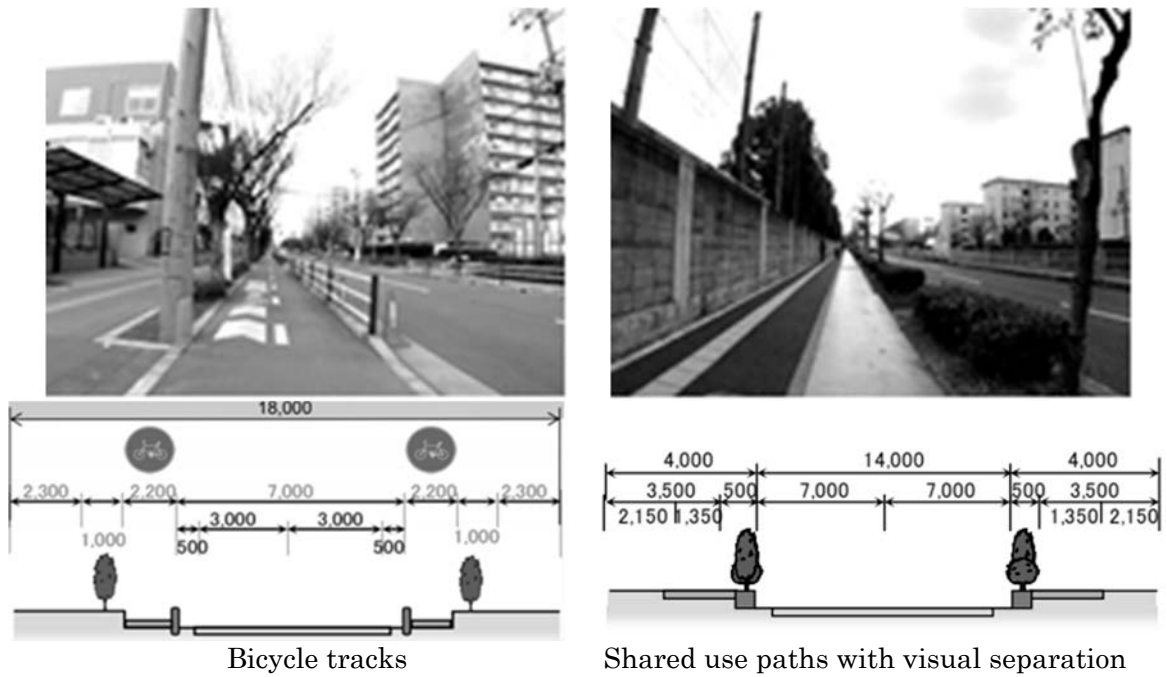


Figure 3. Experimental courses in Sakai City

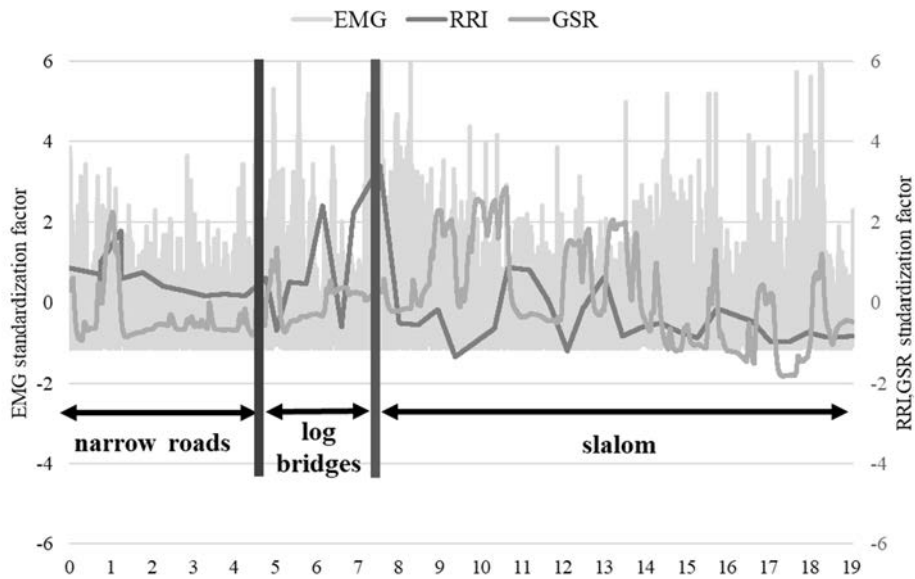


Figure 4. Reaction characteristics of vital reactions

4. Results

4.1 Vital reaction characteristics running on a simple course

A comparison of the reaction characteristics of vital reactions of each obstacle in the biking course (Fig. 4) revealed that RRI and GSR exhibited a gradual response for almost all subjects and continued for a certain period of time under conditions where biking loads, such as narrow roads and log bridges, continued. GSR and EMG also tended to react instantaneously to steering operations such as wobbling, slalom, turning right, turning left, and avoiding obstacles. There was no reaction to movements such as hand signals and left/right confirmation.

Regarding individual differences, a comparison of the changes in vital reactions due to the frequency of daily use of bicycles caused by activities such as going to school revealed an RRI with a greater tendency to decrease

or increase than for students who did not use bicycles at school. In GSR, there was a tendency that the numerical fluctuation at the time of reaction was significant. In EMG, there was no difference in reaction depending on the frequency of bicycle use. Even for students with the same rate of use, RRI and GSR showed significant differences in the time to return to normal values after the values fluctuated.

4.2 Changes in vital reactions depending on degree of biking tasks

The five subjects were classified according to the difference in their biking experience, and vital reactions due to simple biking tasks in campus experiments and vital reactions due to complicated biking tasks in road experiments were compared by the average values of each group (Fig. 5).

Consequently, as tasks became more complex, RRI values tended to decrease, and EMG and GSR values tended to increase gradually. Therefore, it was found that the vital reactions increase as biking tasks become more complicated.

Regarding changes in vital reactions due to differences in biking experience, RRI decreased as tasks became more complicated for both regular and infrequent bikers. However, there was no significant difference in reaction between subjects who rode bicycles daily and those who did not. Moreover, in EMG and GSR, compared to subjects who ride bikes infrequently, the subjects who rode them regularly tended to have a more significant reaction under any biking task. A possible reason for the difference in biking experience is that EMG and GSR have a faster reaction rate to stressors than RRI. Perhaps in addition to the overt mental load, such as a collision or contact typically felt by a bicycle rider, regular riders are also subjected to greater potential psychological pressure from risk prediction. Therefore, it is reasoned that experienced riders were more responsive to stress.

4.3 Evaluation of each traffic lanes

The comparison of the traffic lane for each single road section and intersection (Fig. 6), in the individual road section, shows that the stress value was higher in the bicycle track for EMG and GSR. In addition, at the intersection, the stress value was higher in the shared use path for RRI and EMG. It was assumed that the bicycle track would be more comfortable to travel than the shared use path, however, it appeared that road conditions, such as the width of the traffic lane and curve, and traffic conditions, such as the distance between the opposing bicycles, impacted the original assumption. As for the width of the traffic lane, the bicycle track with a diameter of 1.3 m feels more squeezed than the shared use path with a width of 3.5 m (lane coloring section 1.35 m) where the travel position cannot be specified. Therefore, a more significant response was demonstrated during passing in the bicycle track for EMG and GSR. In addition, because the RRI and EMG responded more significantly to the curves existing in the bicycle track, it became clear that the lane outline was also a factor affecting the vital reaction.

From these results, it is expected that RRI is suitable as an index for evaluating the entire section, and EMG and GSR are suitable as an index for assessing the degree of each stressor. In particular, EMG and GSR have different reaction rates, such that aptitude may differ depending on the duration of the bike ride. Therefore, EMG is suitable for stressors with low biking loads such as avoiding pedestrians, bicycles and obstacles. Furthermore, GSR may be ideal for stressors with continuous biking loads, such as the width of the traffic lane, fences, and curves.

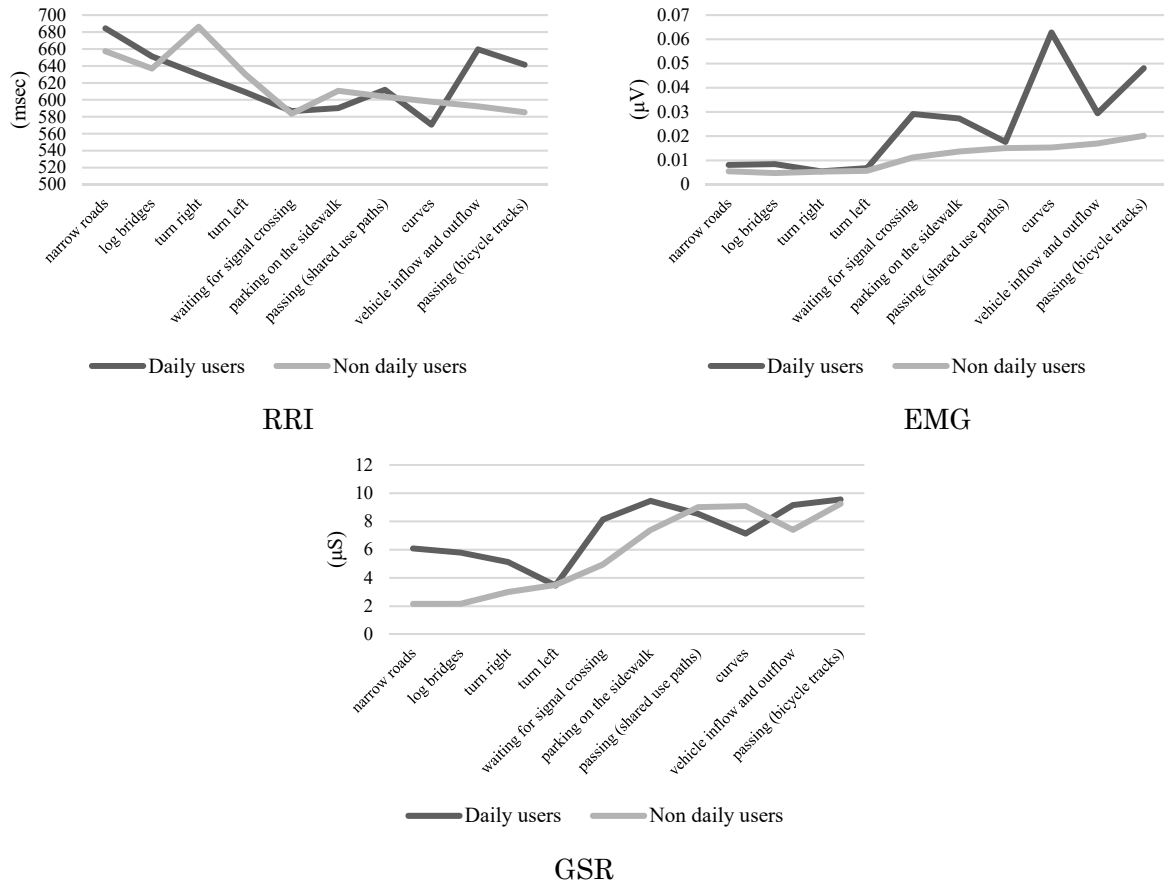


Fig 5. Vital reactions depending on degree of driving tasks

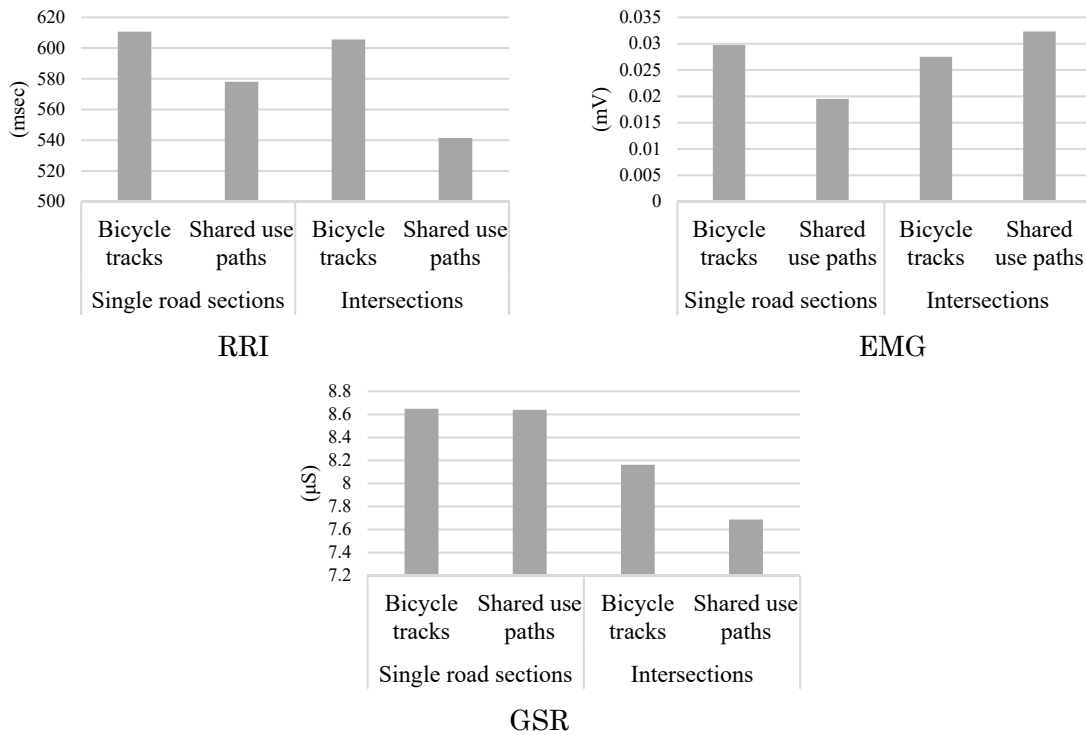


Fig 6. Evaluation of each traffic lanes

5. Conclusion

From the results of this experiment, RRI and GSR showed reactions that gradually started and continued when biking loads were maintained. In addition, EMG tended to respond to steering operation instantaneously.

A comparison of the changes in vital reactions depending on the degree of difficulty biking tasks, it was found that the essential reaction increased as biking duties become more complicated for all vital reaction indices. Regarding changes in vital reactions in EMG and GSR due to individual differences such as biking experience, compared to subjects who did not ride bicycles daily, experienced bike riders tended to have a more significant reaction under any biking task.

Thus, it is clear that the vital reactions of bicycle riders are greatly influenced by the degree of difficulty biking tasks required for traveling in each lane, the biking experience of riders, and their physical ability.

Furthermore, as a result of evaluation of traffic lanes, it became clear that even lanes separated from cars and pedestrians, such as bicycle-only lanes, can become a stress factor by route design, such as the width of traffic lanes and curves. These factors need to be considered in the design of future traffic lanes.

Prior to future development, it is necessary to classify in detail all biking tasks required for traveling in each traffic lane by measuring vehicle behavior and analyzing the relationship between the rider vital reactions and biking tasks.

6. References

- 1) N. Yoshida: Bicycle traffic facilities in various countries. IATSS Review, Vol.41, No2, 2016.
- 2) K. Suzuki, K. Imai, M. Fujita: QOS evaluation method of arterial roads from bicycle users' objective and subjective points of view, Infrastructure planning review, 31, Vol.70, No.5, 2014.
- 3) D. Shibutani, T. Kin : Study on evaluation of driving environment mixed for pedestrians, bicycles and cars using stress measurement, Infrastructure planning review, Vol.48, No.234, 2013.
- 4) T. Takeda: Somatic effects of mitten restraint –Psychophysiological research on patient stress caused by mitten restraint -, Synergetic welfare science 9, Vol2, 19-32, 2014.
- 5) H. Yamakawa, Le Quoc Dung, A. Yamashita, H. Asama: Estimation of stress during car race using physiological measurements, JCMSI, pp853-858, 2014.
- 6) T. Okada, N. Yoshida: Analysis of road traffic conditions and individual knowledge and experience on cyclist path choice behavior, Infrastructure planning review, Vol.70, No.5, 2015.
- 7) Shawn Achor: The Happiness Advantage: The Seven Principles of Positive Psychology that Fuel Success and Performance at Work, Virgin Books, 2011.
- 8) S. Haga, N. Mizukami: Japanese version of NASA Task Load Index, Japan Human Factors and Ergonomics Society, Vol32, No2, 1996.
- 9) Sakai City: Improvement of bicycle traffic environment, <http://www.city.sakai.lg.jp/kurashi/doro/jitensha/seibi.html>, 2017.
- 10) A. Caviedes, M. Figliozzi : Modeling the impact of traffic conditions and bicycle facilities on cyclists on-road stress levels, Transportation Research Part F, Traffic Psychology and Behaviour, volume58 (2018), pp. 488-499.
- 11) K. Kelarestaghi, A. Ermagun, K. Heaslip : Cycling usage and frequency determinants in college campuses, Cities, volume90, (2018), pp. 216-228.

Abstracts of Papers

Published in Other Journals

Mechanical Engineering

Development of Heating Test Equipment for Improved Utilization of Superheated Steam: Monitoring Color Change in Food at High Temperature

Y. TANADA, H. IYOTA, H. SAKAI and K. FUKUCHI

Proc. of the 4th Asia Color Association Conference, Chiang Mai, Thailand, Dec. 5-8, pp.258-262 (2018).

Superheated steam, i.e., high-temperature steam above the boiling point at atmospheric pressure, has been widely used as a heating medium in food baking/drying equipment. The humidity inside the baking/drying equipment have temporal and spatial distribution because there is an inflow of indoor air during food insertion. However, a slight humidity change can influence the heat transfer to the food, which can seriously affect its quality. To solve these problems and improve the utilization of superheated steam, a test apparatus that can set and control the heating conditions was developed in this study. By using this apparatus, we could observe the change in food color under various humidity conditions. To measure the spectral reflection spectrum on the surface of a food sample, spectroscopic measurement devices were installed. A sweet potato slices was inserted at the bottom of the test chamber and heated for 12 minutes with hot air and superheated steam, both at a flow rate of 1 m/s, and a temperature of 200°C. The difference in color change due to the heating media could be observed; the redness of the sample heated with superheated steam was slightly more intense than that of the sample heated with hot air.

Gloss Distribution Measurement of Foods and their Visual Palatability Evaluation

M. ISOMI, H. IYOTA and H. SAKAI

Proc. of the 4th Asia Color Association Conference, Chiang Mai, Thailand, Dec. 5-8, pp.165-171 (2018).

We conducted sensory tests to determine the preference of food appearance by paying special attention to their glossiness. We prepared chicken meatloaf, cookies and fried rice samples; they were all replica foods made of plastic resin, and by painting gloss/matte varnishes, high-, medium-, and low-gloss samples were manufactured. A total of 32 subjects (16 males and 16 females, age 21-24 years old) evaluated the glossiness of foods under the daylight-color or light-bulb-color illumination. The results are as follows: (1) The gloss evaluation of the food is not affected by the color temperature of the light source. (2) Food glossiness tends to be emphasized in comparison with that of industrial products. (3) Glossy foods look like warm, fresh and tasty.

Evaluation of Surface Color of Steam-Cooked Manju through Non-Contact Colorimetric Measurement Using Dome Illumination: Effect of Processing Conditions

H. YAMAMOTO, H. SAKAI, S. KITAMURA, M. TAKAYAMA and H. IYOTA

Proc. of the 4th Asia Color Association Conference, Chiang Mai, Thailand, Dec. 5-8, pp.172-177 (2018).

This paper outlines the results of experimental measurement of the colors of two types of steamed buns (Mugwort Manju and brown Sugar Manju) that were steamed using a continuous steamer, typically used in a food factory. A precise color information was achieved and the effect of the amount of air mixed in the steamer on the color and gloss of the baked food was investigated. It was established that the value of lightness, L^* , increased with steaming, and, as the aeration amount decreased or the humidity in the steamer increased, this value also increased. In addition, it was found that the value of glossiness, $G_s(20^\circ)$, decreased with heating and tended to decrease further with increasing humidity in the steamer. The results indicated that the glossiness of the steamed Mugwort Manju was higher than that of the brown Sugar Manju.

Non-Contact Colorimetric Measurement Using Dome Illumination for Complex Shape Objects

H. SAKAI, M. ISOMI and H. IYOTA

Proc. of the 4th Asia Color Association Conference, Chiang Mai, Thailand, Dec. 5-8, pp.183-186 (2018).

A method is discussed to measure the color distributions of complex shape objects such as rocks, woods, foods in the SCE (Specular Component Excluded) and SCI (Specular Component Included) modes. Commercially available colorimeters are usually contact-type and work perfectly right out of the box for flat and uniform surfaces. However, they are not used for rough and/or non-uniform surfaces of complex shape objects. For such surfaces, non-contact measurements are required and users have to set up the illumination and the colorimeter separately. These operations are not easy; for example, improper illuminations may cause shades on the sample surfaces. To solve this problem, we have developed an integrating sphere (called "dome illumination") with a

movable light-trapping plate for illumination. It is a spherical dome whose inner surface was painted white, and large enough for samples to be placed on the stage in the middle of the dome; an illuminating light source was placed below the sample stage so that samples could be illuminated only by the indirect diffuse light. This dome illumination makes it possible to get an unshaded image of rough surfaces when observed from the top of the dome. Moreover, the movable light trap works as a switch of specular components to obtain the colorimetric images in both SCI and SCE modes. In addition, the gloss distribution can be derived by comparing the SCI and SCE images because their difference is caused by the specular gloss of a sample surface. This paper outlines the colorimetric system with dome illumination and movable light traps we developed. Also, the procedure is described to derive the gloss distribution of rough surfaces by comparing the SCI and SCE images.

Theory and Practice of Color Measurement

H. SAKAI and H. IYOTA

Abstract Book of 2nd Int. Conf. on Appl. Sci., Eng. and Interdisciplinary Studies (2nd ASEIS 2019), Pathumthani, Thailand, July 4-5, No. S2IN2 (2019).

The color we perceive on an object's surface depends not only on the object itself, but also on the light source and observer. Therefore, to compare measured colors, the standard procedures recommended by the Commission Internationale de l'Eclairage (CIE) should be followed. However, these do not work well for rough and non-uniform surfaces of complex shaped objects, such as rocks, wood, and food. This is because the CIE standards assume a flat and uniform object surface. To solve this problem, we propose an integrating sphere with a movable light-trapping plate for illumination to measure color distributions of rough and non-uniform surfaces. It is a spherical dome whose inner surface is painted white, and large enough for objects to be placed on a stage in the middle of the dome. An illuminating light source is placed below the stage so that objects can only be illuminated by indirect diffused light. This dome illumination makes it possible to obtain unshaded images of rough surfaces.

In-situ Color Measurement in Steam Oven for Food Quality Analysis

H. IYOTA and H. SAKAI

Abstract Book of 2nd Int. Conf. on Appl. Sci., Eng. and Interdisciplinary Studies (2nd ASEIS 2019), Pathumthani, Thailand, July 4-5, No. S2O1 (2019).

We introduce a colorimetric method for visual evaluation of foods, an in-situ color measurement during food processing using a spectrometer and a glass fiber probe. A crumb of sliced white bread was used as the sample foodstuff to demonstrate the performance of the method. The baking process and the quality of the baked product were investigated. Producing delicious-looking food is one of the qualities required incoming cooking equipment. The color measurement method introduced is very useful for evaluating cooking equipment from the visual aspects of foods.

Control of Droplet Movement on a Plate with Micro-Wrinkle by Difference of Wettability

Kenji KATOH, Eriko SATO, Shin'ya YOSHIOKA and Tatsuro WAKIMOTO

Experiments in Fluids, Vol. 60, No. 9, 140, 11pages (2019).

In this study, we consider the control of a liquid droplet movement rolling down on an inclined plate with gravitational force using a micro-wrinkle on a wall. The micro-wrinkle was manufactured by the buckling of a thin polymer film (poly(*N*-vinylcarbazole), PVK) on a base polymer (poly(vinyl chloride), PVC). The PVC was stretched once and then PVK (~100-nm thickness) was spin-coated on the surface of the base polymer at ambient temperature. When the strain was released in a thermostatic chamber heated above the glass transition temperature of PVC, a two-dimensional micro-wrinkle having a wavelength of several micrometers was formed on the surface. The advancing and receding contact angles were measured in directions parallel and perpendicular to the wrinkle. It was observed that there were several degrees of contact angle anisotropy. When the droplet was set on the wrinkle surface inclined at 45° to the gravitational force, the direction of droplet movement could be changed by ~20° from the gravitational direction. The deflection angle was estimated from a theoretical model with the principle of minimum work of the contact line.

Length of Bubble Dispersion Region in a Cylindrical Bath Subjected to Side Gas Injection through an L-shaped Lance

Tatsuro WAKIMOTO, Yuki FUKUI, Kenji KATOH and Manabu IGUCHI

Advanced Experimental Mechanics, Vol. 4, pp. 67-73 (2019).

Dissolved oxygen in liquids plays an important role in a variety of fields such as materials engineering. For example, the dissolution rate of oxygen into a molten metal bath is responsible for the efficiency of decarburization in the steelmaking industry. Oxygen is commonly introduced into the bath using many kinds of injection devices. The dynamic behavior of oxygen bubbles mainly governs the oxygen dissolution rate. Water model experiments were carried out in a previous study to understand the oxygen bubble behavior and dissolution rate for basic three (bottom, side, and top) gas injection systems. The side gas injection was found to be most effective for oxygen dissolution. This is probably because the oxygen dissolution rate is closely associated with the length of bubble dispersion region in the bath. In this study air was injected horizontally into a cylindrical water bath through an immersed L-shaped lance. The dispersion pattern of bubbles and related bath surface oscillations were observed with a high-speed video camera and a still camera. An empirical equation was proposed for the length of bubble dispersion region, L_{BS} , based on the data on L_{BS} measured in this study.

Bubble Dispersion Behavior in a Cylindrical Bath Stirred by Horizontal Gas Injection from an L-shaped Lance

Yuki FUKUI, Tatsuro WAKIMOTO, Kenji KATOH and Manabu IGUCHI

Journal of the Japanese Society for Experimental Mechanics, Vol. 18, No. 4, pp. 250-257 (2018) (in Japanese).

The dissolution rate of oxygen into a molten metal bath is responsible for the efficiency of decarburization in the steelmaking industry. Oxygen is commonly introduced into the bath using many kinds of injection devices. The dynamic behavior of oxygen bubbles thus generated in the bath mainly governs the oxygen dissolution rate. Model experiments were carried out in this study to understand the oxygen bubble behavior. Water and air were chosen for the models of molten metal and oxygen, respectively. Air was injected horizontally into a cylindrical water bath through an immersed L-shaped lance. The dispersion patterns of bubbles and related bath surface oscillations were observed with a high-speed video camera and a still camera. The patterns were classified into seven types under the experimental conditions considered in this study.

A Study on Surface Property of Molten Solder in Oxidative Environment

Tatsuro WAKIMOTO, Kokichi ABE, Kenji KATOH, Yoshiaki UEDA (Setsunan Univ.) and Manabu IGUCHI

Proc. of the 13th International Symposium on Advanced Science and Technology in Experimental Mechanics, F01141, 3 pages (2018) (on USB memory).

Surface tension of liquid metal varies in oxide condition for a short time since it is sensitive to surface oxidation. The temporally varying surface tension, i.e. dynamic surface tension, has great impact on many industrial processes relating to liquid metal. In this study, we measured the dynamic surface tension of solder in different oxidation environment by capillary jet method, as well as well-known static surface tension by pendant drop method. While the measured static surface tension decreased with increasing oxygen concentration at oxygen concentrations less than 0.025% because of oxygen adsorption to the surface, it increased at high concentrations greater than 0.025%. The static surface tension also increased with drop diameter at the high oxygen concentrations. The extraordinary behavior in high-oxygen environment suggests the formation of oxide layer. The measured dynamic surface tension indicated fast decrease from initial value to equilibrium surface tension for 2 - 4ms under the oxygen concentration of around 0.02%.

Ultrasonic Testing of GFRP Laminate Degraded by Hot Water from One surface

Akihiro WADA, Tomohiro YAMASAKI and Kazuyoshi WASEDA

Journal of the Society of Materials Science, Japan, Vol. 68, No. 5 (2019), pp. 436-442.

Ultrasonic wave is applied to damage evaluation of GFRP laminate degraded by hot water from one surface. GFRP vessels have been used for storage of both acid solution and alkaline solution because of their excellent corrosion resistance. In these days, integrity evaluation of GFRP vessels has attracted much attention as the number of aged vessels increases. Although degradation proceeds gradually from the inner surface of vessels, sensors can only be attached on the outer surface. Then the through-thickness method for damage evaluation is required. In this research, GFRP plates are degraded by hot water from one surface, and through-thickness ultrasonic inspection is conducted to reveal the dependence of ultrasonic characteristics on damage state of the plates. Beside wave attenuation and velocity, characteristics of reflected waveforms from the degraded surface are analyzed. It is found that the envelope of echo from the degraded surface reflects damage propagation in the thickness direction, and it can be used as damage index of GFRP vessels.

Development of Magnetic Bridge Inspection Robot Aimed at Carrying Heavy Loads

Yodai MATSUMURA, Takehiro SHIBA, Satoshi ITO, Yuya KAWASE and Yogo TAKADA

International Journal of Robotic Engineering, Vol.3, Issue 2, 10 pages (2018).

This paper presents a bridge inspection robot capable of traveling on inner right-angled paths. Locomotion of the newly developed robot is achieved via two motor-driven wheels that are composed of steel yokes, acrylic plates, and neodymium magnets. When the wheel contacts a steel plate, it forms a magnetic circuit and generates a strong force. Owing to this force, the robot can move with heavy objects attached. However, when the wheels strongly adsorb on two surfaces at right-angled junctures, the robot becomes unable to move. To peel the wheels away from one surface, a mechanism is needed to eliminate the strong magnetic force. To achieve this, the robot has been equipped with a pushing mechanism that allows for travel on any inner right-angled path. In this study, the performance of the robot was tested on a steel box that imitated a box girder. The robot was able to carry heavy objects, and it also showed an ability to travel along paths that included a right-angled juncture by utilizing the pushing mechanism.

Development of a Compact Wall-Climbing Robot Capable of Transitioning among Floor, Vertical Wall and Ceiling

Yodai MATSUMURA, Koyo KAWAMOTO and Yogo TAKADA

Journal of the Robotics Society of Japan, Vol.37, No.6, pp.1-10 (2019) (in Japanese).

Many social infrastructures in Japan have been intensively developed since the period of high economic growth, and the aging of them is progressing. Therefore, periodic inspections and repairs are necessary. Inspections require huge costs and take a long time because inspectors visually inspect bridges directly using scaffolds or special cranes. Practical bridge inspection robots are strongly required to reduce the costs and time associated with inspection of bridges. In recent years, various robots have been developed for bridge inspections. However, many of these robots lack the ability to locomote within inspection areas. Therefore, there are many paths which they cannot move under the three-dimensional complex environments of actual bridges. Practical bridge inspection robots are required to be able to transition between a horizontal plane and a vertical plane. Additionally, they are also required to be capable of traveling through bolted splicing parts. However, robots capable of running through these paths have not been reported. We developed a compact wall-climbing robot BIREM-IV which is equipped with four rimless wheels as driving wheels. Strong permanent magnets are attached to its rimless wheels. Therefore, the robot can move around while adsorbing on a steel structure. Furthermore, the running performance of the robot was examined by experiments. It was confirmed that this robot can easily run through bolted splicing parts. Moreover, this robot can surely transit among floor, vertical wall, and ceiling without falling from the structures.

Investigation of Rotors Imitating Bird Wings to Reduce Electricity Consumption of HORNET

Yogo TAKADA, Tatsuki KANADA, Takahiro TANAKA and Yodai MATSUMURA

Journal of Aero Aqua Bio-mechanisms, Vol.8, No.1, pp.48-53 (2019).

To address the deterioration of bridges and buildings, we have developed a robot, HORNET, to inspect building walls. This robot travels on the wall surface using propellers with wheels on the wall. As the running duration is short on smooth surfaces, the cross-sectional shape of the rotor was designed to reduce the power consumption using two-dimensional numerical analysis using a genetic algorithm. Furthermore, we manufactured several kinds of rotors imitating birds and performed experiments to determine the ideal shape to reduce electricity consumption. Experiments were also conducted to evaluate the performance when the rotor was attached to HORNET. First, we developed HORNET's dynamic model and evaluated the performance by running a simulation on a route imitating the actual inspection route. Additionally, by installing a new rotor in HORNET, we evaluated the running performance on the up and down paths.

Small Robotic Fish with Two Magnetic Actuators for Autonomous Tracking of a Goldfish

Takuya ARITANI, Naoki KAWASAKI and Yogo TAKADA

Journal of Aero Aqua Bio-mechanisms, Vol.8, No.1, pp.69-74 (2019).

In this study, we describe a palm-sized robotic fish that can automatically track a goldfish. A robotic fish is suitable for ecological surveys because it is difficult to be noticed by aquatic animals. However, so far, there is no palm-sized robotic fish that can automatically track an aquatic animal. Automatic tracking by the robot is carried out by recognizing the goldfish with a camera and changing the swimming direction towards the goldfish. To follow the agile movement of the goldfish, the robot has a high turning ability with multiple joints. Finally, we have confirmed the robot can track a goldfish.

Testing the Repellent Effects of Construction Materials on the Attachment of the Invasive Golden Mussel, *Limnoperna fortunei*, in a Japanese Urban Tidal River

K. MATSUI (Kindai University), T. FUMOTO (Kindai University), H. KAWAKAMI

Limnology, 20, pp.131–136 (2019).

The golden mussel, *Limnoperna fortunei*, is native to South China but has spread to Japanese freshwater environments as a nuisance invasive species. The golden mussel colonizes hard manmade substrates and its attachment can cause economic losses at water intake facilities. To evaluate the repellent effects of the high alkalinity (pH 12–13) of freshly prepared cement mortar on golden mussels, test pieces made of cement were immersed in a Japanese urban tidal river. Compared with coated mortar, and wood and limestone test pieces, the cement mortar did not show significant repellent effects on golden mussel attachment. Therefore, concrete constructions on riverbanks may be a preferred substrate for golden mussel colonization. A 4-year immersion experiment showed that copper substrate had a strong repellent effect on biofouling, while cement mortar, aluminum, and stainless steel did not have any adverse effects on golden mussel attachment. This experiment also revealed the settlement of invasive golden mussel in an urban tidal area where the salinity fluctuated up to 20.0‰.

Confocal Micro XRF Monitoring of Microbially Influenced Corrosion Process of Steel Samples

J. CHIN, R. HOSOMI, H. KAWAKAMI, K. TSUJI

Adv. X-Ray. Chem. Anal., Japan, 50, pp.169-175 (2019)(in Japanese).

X-ray fluorescence analysis (XRF) is a non-destructive method. There is a lot of applications like analysis of industrial material. A confocal micro XRF instrument enables elemental analysis of point-limited region. The confocal micro XRF instrument was applied to in situ analysis of microbiologically influenced corrosion process. Finally, it was realized to visualized Fe distribution corroded from steel sample in the solution. (This is identical to the abstract that will appear in the section of Applied Chemistry and Bioengineering).

TEM Observation of Cells Treated with Metal Ions

Y. KIKUCHI, M. TAKAOKA, Y. NISHIOKA, H. KAWAKAMI

J. Jap. Inst. Copper, 58, pp. 285-289 (2019) (in Japanese).

Copper, Silver, Nickel and Zinc are well known as antibacterial metal. Introducing antibacterial metals into environment surface in hospitals will decrease the number of viable bacteria on the surface of medical instruments and foods making appliances. On the other hand, the antibacterial (killing) mechanism of antibacterial metals has not yet been fully described. A couple of explanations have been proposed. (1) Reactive oxygen species are generated from the metal surface. (2) Hydrogen peroxide is caused by Fenton-type reactions. (3) Metal ion combines with bacterial cell components. But how to change of bacterial cell structure by killing action come about is not known yet. In this investigation, imaging of cell structures damaged by metal ion is attempted. Bacterial cells were treated with an antibacterial metal ion solution. Treating times were varied from 2 hour to 12 hour. The treated cells were collected by centrifugation, chemically fixed, and embedded in resin. Ultra-thin sections were cut from them and observed by transmission electron microscope. Precipitates in damaged cell were analyzed by EDX. In this investigation, as first trials, Ag was selected. Ag has the most strong killing effect compared with Cu, Ni, and Zn. Ag ion content of the solution was 5 ppm. *Staphylococcus aureus* was tested. The antibacterial property was evaluated in accordance with JIS Z 2801. The structure of *Staphylococcus aureus* sustained increasing damage with the laps of time. After at least 4 hour, small particles of precipitate in the damaged cells were found. From the precipitates, Ag and S were detected by EDX analysis. It appears that Ag ion diffused in to cell and combine with cell components. Consequently, an activities of *Staphylococcus aureus* are dramatically decreased. Also, cell wall thickness decreased with exposure time. From the obtained results, the possible killing mechanisms are discussed. Finally, this study concludes that TEM observation is a useful a tool for this type of investigation.

Effect of Addition of Rust Inhibitor on Antibacterial Activities of Oxygen Free Copper Immersed Repeatedly in NaOCl Aqueous Solution

Y. TODA, H. KAWAKAMI, Y. SUETAKE (Naigai Chemical Products), K. MARUGAME (Naigai Chemical Products)

J. Jap. Inst. Copper, 58, pp. 273-278 (2019) (in Japanese).

Copper is known as antibacterial metallic material. Introducing such copper into frequently hand-touched places has been considered to reduce risks of outbreaks of illnesses caused by pathogens on environmental surfaces. When copper is used in environmental surfaces, surfaces of copper are exposed to the surrounding environment and become contaminated by various substances in the surroundings. As surfaces contamination can reduce the

antibacterial activity of copper, cleaning henceforth must be carried out periodically on the contaminated surface. However, due to the cleaning agents such as the ethanol aqueous solution (EtOH) and the sodium hypochlorite aqueous solution (NaOCl aq.) used for wipe-cleaning, copper surfaces may be corroded and the antibacterial activities may be lost. In this study, we carried out surface chemical analysis using x-ray photoelectron spectroscopy (XPS) and evaluate the antibacterial activities of copper submerged in cleaning agents. Also, in this study, the antibacterial activities of copper compounds formed on the copper surfaces submerged in cleaning agents were evaluated. Copper surfaces submerged in distilled water, EtOH and NaOCl aq. were corroded and the antibacterial activities decreased. Cu, Cu₂O, CuO, Cu(OH)₂ and CuCl₂ were present on the copper surfaces submerged in cleaning agents. The strength of the antibacterial activities was in the order Cu₂O, CuCl₂ > CuO > Cu(OH)₂ > CuCO₃. When benzotriazole as a rust inhibitor was added to NaOCl aq., the antibacterial activities of copper decreased. Other inhibitors, i.e. sodium hexametaphosphate, sodium molybdate dihydrate, trisodium phosphate, to lytriazole and sodium tungstate dihydrate as a rust inhibitor, was used, NaOCl aq., the antibacterial activities of copper improved in comparison with NaOCl aq. without the inhibitors. In particular, the antibacterial activities of copper submerged in trisodium phosphate inoculated NaOCl aq. was almost equivalent to that of clean copper.

Interlaminar Toughening for CFRP Laminates by Introducing Mesh Interlayers with Different Opening Areas

Hayato NAKATANI and Masato NAKANE

Proc. Future Generation Symposium on Composite Materials 2019, Shirahama, Japan, August 26-27, paper ID: GS01 (2019).

A polymer mesh inserted between CFRP plies as an interlayer produces more complex path of crack as interfacial debonding between polymer matrix of CFRP and the mesh and this fracture behaviour results in improved interlaminar toughness. The present study evaluates the interlaminar toughness of UD-CFRP laminates with different opening area under constant wire diameter (45µm) of the introduced mesh layers. 4ENF tests have revealed that there is an apparent peak value of interlaminar toughness G_{IIR} with opening area of 46%. A micro focus X-ray CT system has successfully reconstructed an overview images of the crack that show much more complex switches of the crack plane inside the laminates with mesh opening area of 46%. It is indicated that the interlaminar fracture toughness of the CFRP laminates with mesh interlayers should be dominated by complex crack growth both in microscopic level as the interfacial debonding and in macroscopic level due to the switches of the crack plane.

Effects of Layer Thickness and Annealing on Vickers Hardness and Wear Resistance in Ni-P / Zn-Ni Multilayered Films

H. KANEMOTO, T. KAWAMURA and Y. KANEKO

J. Surface. Finish. Soc. Japan, Vol.70, pp.115-121 (2019).

Ni-P / Zn-Ni multilayered structures were fabricated by an alternate electroplating using two electrolyte baths. The multilayered structures were grown on a steel substrate. To investigate the effect of component layer thickness and annealing on hardness and wear resistance, we prepared two series of the multilayered structures. In one series, the Ni-P and Zn-Ni layers had equal thicknesses of 200 nm, 500 nm, and 1000 nm, while the other series had the constant Ni-P layer thickness of 500 nm. Then, the electroplated films were annealed at 573K for 2 hours. For all the multilayered structures, the annealing led to increases in hardness and wear resistance due to hardening in the Ni-P layers. Among the multilayers having the same component thickness, the 500-nm layer thickness showed the highest hardness and wear resistance. In the annealed multilayers having the constant Ni-P thickness of 500 nm, the hardness and wear resistance increased with decreasing Zn-Ni layer thickness. Our key finding is that the annealed multilayers consisting of 500-nm Ni-P and 100-nm Zn-Ni layers exhibited a higher wear resistance than an annealed Ni-P film, by a factor of three.

Constitutive Equations for Rubber under Abrupt Change in Strain Rate Direction

Y. TOMITA and M. UCHIDA

Key Eng. Mater., Vol. 794, pp. 9-18 (2019).

We proposed constitutive equations for the strain rate and temperature-dependent behavior of rubber by employing the nonaffine molecular chain network theory and reptation theory. The finite element homogenization method along with the proposed constitutive equations have the capability of predicting the deformation behaviors of particle-filled rubber under changes in volume fractions, distribution patterns, and size heterogeneity of the particles without additional parameters. The only existing problem is the modest estimation of the stiffness of

rubber immediately after the abrupt change in strain rate direction (ACSD) as can be seen in the cyclic deformation behavior. We restricted our attention to the generalization of our nonaffine molecular chain network theory to overcome the problems associated with ACSD. We consider the effect of the delay of deformation in surrounding chains on the elasticity modulus by introducing an amplification parameter dependent on the current chain stretch and direction of strain rate immediately after ACSD. The potential of the proposed constitutive equations is examined against the predictability of the experimentally obtained deformation exhibiting ACSD.

Macroscopic and Microscopic Non-uniform Deformations of Polycrystalline Pure Copper during Uniaxial Tensile Test with High Stress Gradient

A. TANIGUCHI, T. MAEYAMA, M. UCHIDA and Y. KANEKO

Key Eng. Mater., Vol. 794, pp. 246-252 (2019).

Metallic materials usually have microscopically heterogeneous structures, such as polycrystalline structures, affecting macroscopic mechanical characteristics. Both macroscopic and microscopic non-uniform deformations of polycrystalline pure copper under a moderate stress gradient were investigated. In this study, macroscopic and microscopic non-uniform deformations under higher stress gradients are investigated. Uniaxial tensile tests using three-curve specimens with different curvatures and grain sizes were performed. In order to evaluate the heterogeneous strain field in the specimen surface, the development of the displacement field was measured using the digital image correlation method (DIC). The stress field was evaluated by coupling the DIC and finite-element methods. In smaller-grain specimens, a strong strain concentration was generated in the minimum cross-section area. Although a strong strain concentration was also confirmed in a larger-grain specimen, the strain field depended not only on the specimen shape but also on the microscopic heterogeneity. This microstructure-driven non-uniform deformation was also observed in the specimen with a larger curvature radius. These results indicated that the macroscopic non-uniform deformation should be estimated by the material parameter related to the microscopic heterogeneity.

Evaluation of Effect of Sample Size and Layer Direction on Mechanical Property of Specimen Manufactured by FDM-Type 3D Printer

H. AKIYAMA, M. UCHIDA and Y. KANEKO

Key Eng. Mater., Vol. 794, pp. 324-332 (2019).

In the present study, we investigate the effect of the sample size and layer direction on mechanical properties of the specimen fabricated by the FDM-type 3D printer under 4-point bending test. Acrylonitrile-butadiene-styrene (ABS) was employed as a source material. Bending tests were performed under several experimental conditions of layer direction, dimension of the specimens and supporting distance. The relationship between bending load and displacement depended strongly on the layer direction. Young's modulus increased with increasing supporting distance, particularly, when the filaments were parallel to the loading direction. The strain distribution during the bending test was evaluated by DIC. When the supporting distance was short, strain distribution obtained from DIC became different from the theoretical distribution. This result indicated that the prominent shear deformation occurs in the bending of the printed material when the supporting distance is short. Subsequently, FEM analysis was performed to remove the error in the estimation of Young's modulus due to the shear deformation, and the correcting equation was proposed.

Evaluation of the Effects of Cross-linking and Swelling on the Mechanical Behaviors of Hydrogels using the Digital Image Correlation Method

M. UCHIDA, T. SENGOKU, Y. KANEKO, D. OKUMURA, H. TANAKA and S. IDA

Soft Matter, Vol. 15, pp. 3389-3396 (2019).

Experimental evaluation and modeling are important steps in the investigation of the mechanical behaviors of hydrogels in the small- to large-strain range. In this study, the effects of cross-linking and swelling on the true stress-strain response of a specific type of hydrogel (polyacrylamide) were evaluated using a uniaxial tensile test. The development of true strain on the surface of the hydrogel was measured using the digital image correlation method. The specimens with higher cross-link density exhibited a higher initial elastic modulus and earlier orientation hardening. The initial elastic modulus was reduced by the swelling, whereas the orientation hardening occurred in an earlier strain range in the swollen hydrogel. The mechanical responses of the as-prepared and swollen hydrogels with different cross-linker contents were fitted using a non-Gaussian statistical model. The conventional model underestimated the decrease in the elasticity owing to the swelling effect and overestimated the increase in the stress in the large-strain range. The mechanical model was suitably modified to yield an accurate reproduction of the mechanical responses. The proposed model, which was characterized by five material

parameters, was found to reproduce the characteristics of the mechanical responses of the as-prepared and swollen hydrogels with different cross-linker contents.

Evaluation and Modeling of Mechanical Behaviors of Thermosetting Polymer under Monotonic and Cyclic Tensile Tests

M. UCHIDA, R. WAKUDA and Y. KANEKO

Polymer, Vol. 174, pp. 130-142 (2019).

A nonlinear elastic-inelastic model for a thermosetting polymer is proposed based on the molecular chain network theory. In the proposed model, the bond of the polymer chain is divided into physical and chemical bonds, and the physical bond is allowed to separate and recombine during the deformation. The decrease in the rigidity and increase in the inelastic strain are related to the development of the physical bond density to represent the characteristic deformation behavior of the polymer. A rate-form large deformation constitutive equation is then formulated based on the updated Lagrangian method. Additionally, deformation behaviors of the epoxy under monotonic and cyclic tensile tests were evaluated by experimental and computational studies. The experimental results of the monotonic tensile test displayed a gradual transition from elastic to inelastic deformation, strain softening behavior after the macroscopic yielding stress, and an increase in the initial slope and the macroscopic yielding stresses with an increasing strain rate. The computational model can represent such characteristics by controlling the development of the physical bond density. In a cyclic test, a decrease in the rigidity and an increase in the residual strain with increasing cycles were observed even in a small strain range. Such inelastic deformation depended on the strain rate and the given upper stress in the cyclic test. Further, the proposed model successfully reproduced such nonlinear behavior in the cyclic test.

Nonlocal Multiscale Modeling of Deformation Behavior of Polycrystalline Copper by Second-order Homogenization Method

M. UCHIDA and Y. KANEKO

The European Physical Journal B, Vol. 92: 189, 11pp. (2019).

Engineering materials usually exhibit heterogeneity such as that observed in the polycrystalline structure of metals, and this heterogeneity affects the nonuniform deformation of a material. In this study, the micro- to macroscopic nonuniform deformation of polycrystalline copper specimen with a curved gage section is evaluated by a finite element method (FEM) simulation based on the second-order homogenization method (2nd-HM). The effects of the microstructure size and macroscopic stress gradient on the nonuniform deformation of the material are then investigated by comparing the simulation and experimental results. A two-dimensional plane strain polycrystalline microstructure was periodically applied to all the integration points in the macrostructure; the anisotropic deformation of the crystal grains is represented by the conventional crystalline plasticity constitutive equation. The computational results indicate that the interaction between nonuniform deformation on the micro and macroscopic scales induces a slight size effect in the material. However, the FEM simulation based on the 2nd-HM could not predict the decrease in the macroscopic strain concentration in the specimens with large crystalline grains, which was observed in the experimental studies, because of random strain localization resulting from the microscopic heterogeneity.

Effects of Cross-link Density on Plastic Flow of Glassy Epoxy Networks

Shin'ya YOSHIOKA, Akira KAWAI and Yasuhito ITAMI

J. Soc. Mat Sci, Jpn, Vol.68, pp.13-19 (2019) (in Japanese).

Steady plastic flow of glassy epoxy networks having various crosslink density was analyzed with Eyring equation to discuss the effect of crosslinked molecular structures on nonlinear viscoelastic behavior of glassy polymers in terms of strain-induced structural change. Steady flow stresses of the glasses were calculated with modified stress optical rule (MSOR) from stress and birefringence data observed during uniaxial stretching. Activation enthalpy ΔH , activation entropy ΔS and activation volume v_a of the steady flow for each material were obtained as functions of stretching conditions by means of a special fitting method of Eyring equation proposed by Nanzai. As having been reported for thermoplastic glassy polymers, ΔH , ΔS and v_a for each material were in unique functional relations each other. The ΔH - ΔS relation for each material agreed fairly well with that derived from WLF equation for the linear viscoelastic relaxation of the material in the molten state. This result confirms that strain-induced change of glassy structures into liquid-like ones is the essential mechanism of the nonlinear viscoelastic behavior of glassy polymers independently of crosslink density. ΔH - ΔS relations for epoxy networks showed only a weak dependence on the crosslink density, whereas v_a markedly increased with increasing crosslink density. The steady flow stresses at an identical straining condition was almost the same for epoxy networks with

different crosslink density except for materials with extremely high crosslink density, which showed a lower flow stress. An increase of crosslink density probably makes v_a enlarge due to constraints introduced by crosslinked structure, resulting in the reduction of flow stresses especially at extremely high crosslink density.

Applied Physics and Electronics

Photoluminescence Polarization Characteristics of Self-Trapped Excitons in an Undoped β -Ga₂O₃ Single Crystal

Suguru YAMAOKA, Yusuke MIKUNI, and Masaaki NAKAYAMA

Journal of Physics: Conference Series Vol.1220, 012030 (4 pages) (2019)

We have investigated the photoluminescence (PL) polarization characteristics of the self-trapped exciton (STE) in an undoped β -Ga₂O₃ single crystal at 77 K under three-photon excitation. From analysis of the polarization characteristics, we found that the STE PL is polarized almost parallel to the *a*-axis. The STE-PL polarization corresponds to the orientation of the self-trapped hole which was investigated in previous works using an electron-paramagnetic-resonance experiment and a first-principles calculation.

DOI: 10.1088/1742-6596/1220/1/012030

Spatially-Resolved Photoluminescence Study of Temperature Dependence of Exciton Inelastic Scattering Processes in a ZnO Thin Film

Masaaki NAKAYAMA and Yojiro NAKAYAMA

Journal of the Physical Society of Japan Vol.88, 083706 (4 pages) (2019)

We have investigated the temperature dependence of exciton inelastic scattering processes, exciton–exciton scattering and exciton–electron scattering, in a ZnO thin film using spatially-resolved photoluminescence (PL) spectroscopy. It was found that the PL band due to the exciton inelastic scattering process is selectively observed at a spot around a film edge away from an excitation spot. The selective observation enabled us to measure precisely the PL-peak energy. The quantitative analysis of the temperature dependence of the PL-peak energy reveals that the exciton–exciton scattering, which occurs in a temperature region from 10 to ~160 K, changes to the exciton–electron scattering in a higher temperature region up to room temperature.

DOI: 10.7566/JPSJ.88.083706

Synergetic Enhancement of Light-Matter Interaction by Nonlocality and Band Degeneracy in ZnO Thin Films

Takashi KINOSHITA, Takuya MATSUDA, Takuya TAKAHASHI, Masayoshi ICHIMIYA, Masaaki ASHIDA, Yoshiaki FURUKAWA, Masaaki NAKAYAMA, and Hajime ISHIHARA

Physical Review Letters Vol.122, 157401 (4 pages) (2019)

This study aims to reveal the full potential of ZnO as an ultrafast photofunctional material. Based on nonlocal response theory to incorporate the spatially inhomogeneous quality of the samples coupled with experimental observations of linear and nonlinear optical responses, we establish the ultrafast radiative decay of excitons in ZnO thin films that reaches the speed of excitonic dephasing at room temperature in typical semiconductors at a couple tens of femtoseconds. The consistency between the observed delay-time dependence of the transient-grating signals and the theoretical prediction reveals that the ultrafast radiative decay is due to the synergetic effects of the giant light-exciton interaction volume and the radiative coupling between multicomponent excitons.

DOI: 10.1103/PhysRevLett.122.157401

Temperature Dependence of Photoluminescence Dynamics of Exciton-Exciton Inelastic Scattering in a GaAs/AlAs Multiple-Quantum-Well Structure

Yuichiro MIYAZAKI and Masaaki NAKAYAMA

Journal of Physics: Conference Series Vol.1220, 012026 (4 pages) (2019)

We have investigated the photoluminescence (PL) dynamics of exciton-exciton inelastic scattering at temperatures from 10 to 60 K. It was found that the energy dependence of the PL decay rate is scaled by that of the group velocity of the photon-like lower polariton (LP) at each temperature, taking account of the broadening factor of the polariton state. This fact demonstrates that the PL decay rate is dominated by the photon-like LP which is the final state of the exciton-exciton inelastic scattering process. The broadening factor is proportional to temperature, which indicates the influence of acoustic phonon scattering on the LP state.

DOI: 10.1088/1742-6596/1220/1/012026

Synthesis of Mn-Doped ZnSe-ZnS Alloy Quantum Dots by a Hydrothermal Method

Hisaaki NISHIMURA, Yuxin LIN, Masayuki HIZUME, Taichi TANIGUCHI, Naoteru SHIGEKAWA, Tomomi

TAKAGI, Susumu SOBUE, Shoichi KAWAI, Eiichi OKUO, and DaeGwi KIM
Chem. Lett. Vol. 48, pp. 1081–1083 (2019).

This study aims to report the hydrothermal synthesis of water-soluble Mn-doped ZnSe-ZnS alloy quantum dots (QDs), wherein manganese (Mn^{2+}) serves as an emission center. The alloy composition was controlled by the mixing ratio of ZnSe:Mn and ZnS:Mn precursor solutions. The photoluminescence (PL) band originating from the d-d transition in Mn^{2+} was clearly observed. With an increase in the amount of ZnS in the alloy QDs, the absorption onset energy shifted toward higher energy, demonstrating the successful preparation of alloy QDs, and Mn PL intensity increased as well.

doi:10.1246/cl.190365

Hydrothermal Synthesis of ZnSe:Mn Quantum Dots and Their Optical Properties

Hisaaki NISHIMURA, Yuxin LIN, Masayuki HIZUME, Taichi TANIGUCHI, Naoteru SHIGEKAWA, Tomomi TAKAGI, Susumu SOBUE, Shoichi KAWAI, Eiichi OKUO, and DaeGwi KIM

AIP Advances Vol. 9, pp. 025223-1-025223-7 (2019).

Water-soluble Mn^{2+} -doped ZnSe quantum dots (QDs) were synthesized using a hydrothermal method. The characteristics of the precursor solutions greatly affected the photoluminescence (PL) properties of the ZnSe:Mn QDs. In QDs synthesized with alkaline precursor solutions, a PL band originating from the intra-3d shell transition of Mn^{2+} is clearly observed, indicating that Mn^{2+} ions are thoroughly doped inside the ZnSe QDs. The PL quantum yield of the ZnSe:Mn QDs synthesized under the optimum conditions reached 20%. By introducing a ZnS shell at the surface of the ZnS:Mn QDs, the PL properties were improved and the PL quantum yield was further increased to 30%.

doi:10.1063/1.5085814

Synthesis of Water-Soluble CuInS₂ Quantum Dots by a Hydrothermal Method and Their Optical Properties

Kazutaka IIDA, Youta UEHIGASHI, Hideki ICHIDA, Hang-Beom BU, and DaeGwi KIM

Bull. Chem. Soc. Jpn. Vol. 92, pp. 930–936 (2019).

Water-soluble CuInS₂ (CIS) quantum dots (QDs) were hydrothermally prepared in the presence of *N*-acetyl-*L*-cysteine (NAC) as a stabilizer, and the optimal hydrothermal synthetic conditions for NAC-capped CIS QDs were investigated. The photoluminescence (PL) quantum yield (QY) of the CIS QDs synthesized under optimal conditions was 4%, which was comparable with the highest QY reported for water-soluble CIS core QDs. The introduction of a ZnS shell produced CIS/ZnS core/shell QDs and further increased the PL QY to 30%. Furthermore, bilayer structures consisting of Au nanoparticles and CIS/ZnS QDs were fabricated using a layer-by-layer method to enhance the PL of the CIS/ZnS QDs on the basis of the localized surface plasmon resonance of Au nanoparticles.

doi:10.1246/bcsj.20180399

Temperature Dependence of Photoluminescence Properties of Water-Soluble CdS Quantum Dots

Kunio SHIMURA, TaeGi LEE, and DaeGwi KIM

J. Physics: Conf. Ser. Vol. 1220, 012029-1-012029-4 (2019).

We investigated the size dependence of band-edge photoluminescence (PL) dynamics for CdS quantum dots (QDs). The temperature dependence of the PL-decay profiles of CdS QDs with an average diameter of 3.7–6.0 nm was measured. The PL-decay profiles became longer as the temperature increased. Further, it was found that the temperature dependence of the PL-decay profiles depends greatly on the QD size. These experimental results can be understood by considering that the magnitude of the splitting energy between the bright- and dark-exciton states depends on the QD size and becomes larger as the QD size becomes smaller.

doi:10.1088/1742-6596/1220/1/012029

Absorption and Photoluminescence Properties of CdSe Quantum Dots Prepared by Hydrothermal Method

TaeGi LEE, Kaito NOGUCHI, Hisaaki NISHIMURA, and DaeGwi KIM

J. Physics: Conf. Ser. Vol. 1220, pp. 012028-1-012028-4 (2019).

Herein, we investigated the preparation and optical properties of water-soluble CdSe quantum dots (QDs). CdSe QDs with a narrow size distribution were hydrothermally prepared by reacting Cd^{2+} with NaHSe in the presence of *N*-acetyl-*L*-cysteine as ligand. Furthermore, photoluminescence quantum yield increased to ~47% when a ZnS shell was applied to prepare the CdSe/ZnS core/shell QDs.

doi:10.1088/1742-6596/1220/1/012028

Preparation of ZnSe-ZnS Alloy Quantum Dots by a Hydrothermal Method and Their Optical Properties

Hisaaki NISHIMURA, Yuxin LIN, Yuki KUNIMASA, and DaeGwi KIM

J. Physics: Conf. Ser. Vol. 1220, pp. 012027-1-012027-4 (2019).

We prepared colloidal ZnSe_xS_{1-x} alloy quantum dots (QDs) and investigated their optical properties. ZnSe_xS_{1-x} QDs were successfully prepared by a hydrothermal method, which was confirmed by the results of X-ray structural analysis. When the alloy composition was decreased from $x = 1$ to 0, the absorption energy continuously shifted to the high energy side. Band-edge photoluminescence (PL) was the main PL band in ZnSe QDs, whereas only defect-related PL band was observed in ZnS QDs. The band-edge PL was clearly observed as the main PL band for $x = 0.52$ to 1, which shifted to the high energy side by decreasing x .

doi:10.1088/1742-6596/1220/1/012027

Temperature Dependence of Photoluminescence Properties of Water-Soluble ZnSe Quantum Dots

Yong-Shin LEE, Taichi TANIGUCHI, and DaeGwi KIM

J. Physics: Conf. Ser. Vol. 1220, pp. 012024-1-012024-4 (2019).

We have investigated the optical properties of ZnSe quantum dots (QDs) prepared by a hydrothermal method. The photoluminescence (PL)-decay profiles become slower with an increase in temperature up to 160 K, contrary to an ordinary behaviour due to thermal quenching. The temperature dependence of the PL-decay profile is explained by a three-state model consisting of a ground state and two excited states of the lower-lying bound-exciton and higher-lying dark-exciton states. The analysis of the temperature dependence of the decay time indicates that the dark-exciton state contributes to the PL-decay process in the ZnSe QDs.

doi:10.1088/1742-6596/1220/1/012024

Correlated Roles of Temperature and Dimensionality for Multiple Exciton Generation and Electronic Structures in Quantum Dot Superlattices

I-Ya CHANG, DaeGwi KIM, and Hyeon-Deuk KIM

J. Phys. Chem. C Vol. 123(2019) pp. 2549–2556.

Quantum dot superlattices (QDSLs), which are one-, two-, and three-dimensional periodic superlattices composed of QDs, induce dimensionality dependent quantum resonance among component QDs and thus represent a new type of condensed matter exhibiting novel energy, exciton, and carrier dynamics. We focused on the two important parameters, dimensionality and temperature, and identified their correlated roles to determine the electronic and photoexcited properties intrinsic to each QDSL at each dimensionality and temperature. We computationally demonstrated that the multiple exciton generation is significantly accelerated at higher temperature especially in the higher-dimensional QDSLs, indicating their great advantage especially at ambient temperature compared to an isolated zero-dimensional QD. Both dimensionality and temperature can be crucial and correlated parameters for independent tailoring of the properties of the QDSLs without changing the size, shape, and compositions of component QDs. The physical insights and advantage of the QDSLs we found here will lead to designing efficient and space-saving optoelectronic and photovoltaic devices that work at ambient temperature.

doi:10.1021/acs.jpcc.8b10565

Absence of Delayed Fluorescence and Triplet–Triplet Annihilation in Organic Light Emitting Diodes with Spatially Orthogonal Bianthracenes

Yong-Jin PU, Rei SATAKE, Yuki KOYAMA, Takahiro OTOMO, Rika HAYASHI, Naoki HARUTA, Hiroshi KATAGIRI, Daisuke OTSUKI DaeGwi KIM, and Tohru SATO

J. Mater. Chem. C Vol. 7 (2019) pp.2541–2547.

Two compounds, 2-methyl-9,10-bis(naphthalen-2-yl)anthracene (MADN), which has a single anthracene unit, and 10,100-diphenyl-9,9'-bianthracene (PPBA), which has two spatially orthogonal anthracene units, were compared and investigated in terms of photoelectric characteristics and the reverse intersystem crossing (RISC) process in organic light emitting diodes (OLEDs). Transient electroluminescence (EL) measurements indicated large contributions of triplet–triplet annihilation (TTA) for MADN but almost no contribution of TTA for PPBA. The magnetic field dependence of EL for the two anthracene compounds was also different. The EL of MADN was sensitive to the magnetic field at high current density, but PPBA showed less dependence, which indicated the absence of the TTA process for PPBA. TD-DFT calculations revealed that PPBA has doubly degenerate lowest triplet states (T_1 and T_2) with a much lower energy than S_1 , which is unfavorable for thermally activated delayed fluorescence (TADF). The near-zero ΔE_{ST} between highly excited states $S_{m \geq 1}$ and $T_{n > 2}$ is favorable to RISC at a highly excited state. Oxygen quenching of photoluminescence only for PPBA and decreasing EL intensity with deexcitation

ing temperature only for PPBA support the existence of the RISC path from $T_{n>2}$ to $S_{m\geq 1}$. A high external quantum efficiency of 11% in blue OLEDs with PPBA was obtained, indicating that this orthogonal anthracene type of molecular design for RISC at a highly excited state would expand the material development of compounds emitting blue fluorescence for OLEDs.

doi:10.1039/c8tc05817b

Dynamics of Quasiparticles Generation, Transport and Relaxation in Armchair-edge Graphene Nanoribbons

Yushi SAKAI and Akira TERAJ

Journal of the Physical Society of Japan, Vol. 88, 054718 (10 pages) (2019)

We study the dynamics of quasiparticles such as quasiparticles generation, charge transport and relaxation in armchair-edge graphene nanoribbons of the ribbon width of six carbon atoms by numerical simulation. A polaron is created by hole injection into HOMO of the ribbons while a self-trapped exciton is created by photoexcitation of an electron from the HOMO to the LUMO. The dynamical simulations after hole injection or photoexcitation have revealed that phonon fluctuations are necessary for the quasiparticles to be generated. The creation time becomes shorter as the amplitude of the phonon fluctuations increases. The polaron transport in the presence of a bond-type defect is also investigated. It is found that the transmittance and the reflectance of the polaron depend on the position of the defect as well as the strength of the applied electric field. Under particular conditions, the polaron may be split into fractions even though it is an elementary excitation. As for the exciton relaxation, it is found that the exciton leaves oscillations of the bond distortion after photon emission. The oscillations are localized in space and quasi-periodic in time and therefore correspond to a breather or an intrinsic localized mode known to exist in nonlinear differential equations and also in conducting polymers.

DOI: 10.7566/JPSJ.88.054718

Compositional nanoanalysis at grain boundaries in Si by atom probe tomography combined with FIB operated at low temperatures

Yutaka OHNO (Univ. of Tohoku), Yasuo SHIMIZU (Univ. of Tohoku), Naoki EBISAWA (Univ. of Tohoku), Koji INOUE (Univ. of Tohoku), Yasuyoshi NAGAI (Univ. of Tohoku), Hideto YOSHIDA (Univ. of Osaka), Naoto KAMIUCHI (Univ. of Osaka), Ryotaro ASO (Univ. of Osaka), Seiji TAKEDA (Univ. of Osaka), Jianbo LIANG, and Naoteru SHIGEKAWA

Extended Abstracts of European Conference and Exhibition on Advanced Material and Processed (EURO-MAT2019), 2019/9/3.

Impact of focused ion beam in the structural analysis of semiconductor interfaces fabricated by surface activated bonding

Yutaka OHNO (Univ. of Tohoku), Hideto YOSHIDA (Univ. of Osaka), Naoto KAMIUCHI (Univ. of Osaka), Ryotaro ASO (Univ. of Osaka), Seiji TAKEDA (Univ. of Osaka), Yasuo SHIMIZU (Univ. of Tohoku), Naoki EBISAWA (Univ. of Tohoku), Yasuyoshi NAGAI (Univ. of Tohoku), Jianbo LIANG, and Naoteru SHIGEKAWA

Extended Abstracts of 30th International Conference on Defects in Semiconductors (ICDS30), 2019/7/23.

Direct bonding of diamond and dissimilar materials for power device applications

Jianbo LIANG, Yasuo SHIMIZU (Univ. of Tohoku), Yutaka OHNO (Univ. of Tohoku), Kenji SHIRASAKI (Univ. of Tohoku), Naoki EBISAWA (Univ. of Tohoku), Yasuyoshi NAGAI (Univ. of Tohoku), Makoto KASU (Univ. of SAGA), and Naoteru SHIGEKAWA

Extended Abstracts of 2019 International Symposium on Single Crystal Diamond and Electronics (SCDE 2019), 2019/6/10.

Impact of Ar atom irradiation on the crystallinity of GaAs/Si interfaces fabricated by surface activated bonding at room temperature

Yutaka OHNO (Univ. of Tohoku), Reina MIYAGAWA (Nagoya Institute of Technology), Hideto YOSHIDA (Univ. of Osaka), Seiji TAKEDA (Univ. of Osaka), Jianbo LIANG, and Naoteru SHIGEKAWA

Extended Abstracts of 2019 IEEE International Workshop on Low Temperature Bonding for 3D Integration (LTB-3D), pp.2 (2019).

Arsenic (As) vacancies are introduced beneath the GaAs surfaces irradiated by Ar atoms for surface activation, while As interstitials are co-introduced at deeper regions. After 673 K annealing, As vacancies disappear by the recombination with As interstitials, via the migration of As interstitials.

Effect of annealing temperature on diamond/Si interfacial structure

Jianbo LIANG, Yan ZHUO (Bristol of Univ.), Satoshi MASUYA (Univ. of SAGA), Manikant SINGH (Bristol of Univ.), James POMEROY (Bristol of Univ.), Seongwoo KIM (Adamant Namiki Precision Jewel. Co., Ltd.), Martin KUBALL (Bristol of Univ.), Makoto KASU (Univ. of SAGA), and Naoteru SHIGEKAWA

Extended Abstracts of 2019 IEEE International Workshop on Low Temperature Bonding for 3D Integration (LTB-3D), pp.3 (2019).

Transmission electron microscope (TEM) observation showed that a 25 nm thick intermediate layer was formed at the diamond/Si bonding interface without annealing, the intermediate layer thickness decreased with the annealing temperature. No cracking even in nanometer scale occurred even after high-temperature annealing at 800 °C.

Artifacts in the structural analysis of SAB-fabricated interfaces by using focused ion beam

Yutaka OHNO (Univ. of Tohoku), Hideto YOSHIDA (Univ. of Osaka), Naoto KAMIUCHI (Univ. of Osaka), Ryotaro ASO (Univ. of Osaka), Seiji TAKEDA (Univ. of Osaka), Yasuo SHIMIZU (Univ. of Tohoku), Naoki EBISAWA (Univ. of Tohoku), Yasuyoshi NAGAI (Univ. of Tohoku), Jianbo LIANG, and Naoteru SHIGEKAWA

Extended Abstracts of 2019 IEEE International Workshop on Low Temperature Bonding for 3D Integration (LTB-3D), pp.55 (2019).

Atomistic structure of interfaces fabricated by surface activated bonding (SAB) at room temperature can be modified under the irradiation of a focused ion beam for structural analysis, presumably due to the migration of atoms assisted by point defects that are introduced during the SAB process.

Atom probe tomography of GaAs homointerfaces fabricated by surface-activated bonding

Yasuo SHIMIZU (Univ. of Tohoku), Naoki EBISAWA (Univ. of Tohoku), Yutaka OHNO (Univ. of Tohoku), Jianbo LIANG, Naoteru SHIGEKAWA, Koji INOUE (Univ. of Tohoku), and Yasuyoshi NAGAI (Univ. of Tohoku)

Extended Abstracts of 2019 IEEE International Workshop on Low Temperature Bonding for 3D Integration (LTB-3D), pp.56 (2019).

Elemental distribution around GaAs homointerfaces fabricated by surface-activated bonding (SAB) is examined by atom probe tomography (APT). Our APT detected small amount of contaminants accidentally introduced on the SAB interfaces. We confirmed that As-deficient intermediate layer at the as-bonded interfaces was recovered by post-bonding annealing.

Fabrication of Diamond/Cu Direct Bonding for Power Device Application

Shinji KANDA, Satoshi MASUYA (Univ. of SAGA), Makoto KASU (Univ. of SAGA), Naoteru SHIGEKAWA, and Jianbo LIANG

Extended Abstracts of 2019 IEEE International Workshop on Low Temperature Bonding for 3D Integration (LTB-3D), pp.57 (2019).

Direct bonding of diamond and Cu is successfully fabricated by surface activated bonding method. An almost full contact area of diamond and Cu is obtained. The effect of annealing temperature on the structure properties of the bonding interface is investigated under in-situ annealing in a transmission electron microscope (TEM).

Electrical properties of p+-GaAs//patterned metal layer/n+-Si junctions

Takashi HISHIDA, Jianbo LIANG, and Naoteru SHIGEKAWA

Extended Abstracts of 2019 IEEE International Workshop on Low Temperature Bonding for 3D Integration (LTB-3D), pp.58 (2019).

We successfully fabricate a p+-GaAs//patterned metal/n+-Si junction by the surface-activated bonding of a p+-GaAs substrate and a patterned metal layer formed on an n+-Si substrate in alignment to an SiO₂ passivation layer.

Bonding strength evaluation of Al foil/AlN junctions by surface activated bonding

Shotaro HORIKAWA, Sho MORITA, Jianbo LIANG, Yoshihisa KANEKO, Yoshitaka NISHIO (Toyo Aluminium K. K.), Moeko MATSUBARA (Toyo Aluminium K. K.), Hiroshi ASAHI (Toyo Aluminium K. K.), and Naoteru SHIGEKAWA

Extended Abstracts of 2019 IEEE International Workshop on Low Temperature Bonding for 3D Integration (LTB-3D), pp.59 (2019).

An Al foil/AlN junction is fabricated by bonding a 30- μ m Al foil and a 650- μ m AlN plate at room temperature and

473 K. Their bonding strength, which is measured by the 180° peel test, is estimated to be ~30 and ~60 N/m for junctions fabricated by the room-temperature and 473-K bonding, respectively.

A polyimide film/aluminum foil junction by modified surface activated bonding

H. AKAZAWA, Jianbo LIANG, Yoshitaka NISHIO (Toyo Aluminium K. K.), Moeko MATSUBARA (Toyo Aluminium K. K.), Hiroshi ASAHU (Toyo Aluminium K. K.), and Naoteru SHIGEKAWA

Extended Abstracts of 2019 IEEE International Workshop on Low Temperature Bonding for 3D Integration (LTB-3D), pp.60 (2019).

We bond a polyimide (PI) film and an Al foil by modified surface activated bonding, in which the surface of Al foil is only irradiated by the fast atom beam of Ar. It is found that the sputtered Al atoms are deposited on the surface of PI film and play a major role in fabricating the PI film/Al foil junction.

Analysis of SiC/Si Bonding Interface with Thermal Annealing Treatment by XPS

Zexin WAN, Liang JIANBO, and Naoteru SHIGEKAWA

Extended Abstracts of 2019 IEEE International Workshop on Low Temperature Bonding for 3D Integration (LTB-3D), pp.89 (2019).

Properties of SiC/Si bonding interface made by surface activated bonding are studied by X-ray photoelectron spectroscopy of the SiC surface that are unveiled by removing Si substrates of SiC/Si junctions. By fitting the XPS spectra, we found that the annealing of junctions brings about the shift in binding energy of Si-C bonding, which is in correlation with the reverse-bias current of SiC/Si heterojunction. The change in the binding energy is assumed to be attributed to the shift of Fermi level at the SiC surface due to the annealing.

Directly bonded n+-InGaP/n+-Si junctions with a low interface resistance

Moritake SAKIHARA, Liang JIANBO, and Naoteru SHIGEKAWA

Extended Abstracts of 2019 IEEE International Workshop on Low Temperature Bonding for 3D Integration (LTB-3D), pp.90 (2019).

We successfully fabricate a n+-InGaP/n+-Si junctions by the surface-activated bonding of n+-InGaP epi layers grown on n+-GaAs substrates to n+-Si substrates. The achieved interface resistance, 0.059 Ω·cm², is lower than the interface resistance of directly-bonded n+-GaAs/n+-Si junctions.

Interfacial characterization of GaN/diamond heterostructures prepared by room temperature bonding for high power device applications

Jianbo LIANG, Yasuo SHIMIZU (Univ. of Tohoku), Yutaka OHNO (Univ. of Tohoku), Kenji SHIRASAKI (Univ. of Tohoku), Yasuyoshi NAGAI (Univ. of Tohoku), Seongwoo KIM (Adamant Namiki Precision Jewel. Co., Ltd.), Martin KUBALL (Bristol of Univ.), Makoto KASU (Univ. of SAGA), and Naoteru SHIGEKAWA

Extended Abstracts of 13th Topical Workshop on Heterostructure Microelectronics (TWHM 2019), pp.115-116 (2019).

Fabrication of GaAs/Diamond direct bonding for high power device applications

Y. NAKAMURA, Yasuo SHIMIZU (Univ. of Tohoku), Yutaka OHNO (Univ. of Tohoku), Kenji SHIRASAKI (Univ. of Tohoku), Yasuyoshi NAGAI (Univ. of Tohoku), Makoto KASU (Univ. of SAGA), Naoteru SHIGEKAWA, and Jianbo LIANG

Extended Abstracts of 13th Topical Workshop on Heterostructure Microelectronics (TWHM 2019), pp.117-118 (2019).

Direct Bonding of GaN and Diamond Without an Intermediate Layer at Room Temperature

Jianbo LIANG, Yasuo SHIMIZU (Univ. of Tohoku), Yutaka OHNO (Univ. of Tohoku), Kenji SHIRASAKI (Univ. of Tohoku), Yasuyoshi NAGAI (Univ. of Tohoku), Seongwoo KIM (Adamant Namiki Precision Jewel. Co., Ltd.), Martin KUBALL (Bristol of Univ.), Makoto KASU (Univ. of SAGA), and Naoteru SHIGEKAWA

Extended Abstracts of 13th International Conference on Nitride Semiconductors (ICNS'13), Bellevue, BP01.12 (2019).

Electrical Properties of GaAs/GaN Junctions by Bonding GaN Layers Grown on Free Standing Substrates

Shoji YAMAJO, Jianbo LIANG, and Naoteru SHIGEKAWA

Extended Abstracts of 13th International Conference on Nitride Semiconductors (ICNS'13), Bellevue, BP02.10 (2019).

GaAs/Si Double-Junction Cells Fabricated by Sacrificial Layer Etching of Directly-Bonded III-V/Si Junctions

Ryo Kozono, Sanji Yoon, Jianbo Liang, Naoteru Shigekawa

The 46th IEEE Photovoltaic Specialist Conference (PVSC 46), 300 - Poster D9, June 16-21, 2019, CHICAGO, IL, USA.

A GaAs/Si double-junction cell is fabricated by directly bonding a GaAs single-junction cell structure grown on a GaAs (001) substrate to a n-on-p Si subcell and separating the GaAs substrate using a sacrificial layer etching. Before the sacrificial layer etching, the III-V/Si junction is annealed at 300 °C for 1 h so as to recrystallize the interface and achieve an enough bonding strength based on the results of hard X-ray photoemission spectroscopy. We obtain a bonding yield of ~80% after the sacrificial layer etching. We confirm that the fabricated double-junction cell normally operates by measuring its current-voltage and spectral-response characteristics.

Effects of Layered Cadmium-Based Nanoparticles on Si Solar Cells.

Yuki IDUTSU, Shun TANAKA, Liang JIANBO, Tomoki NARAZAKI, Hisaaki NISHIMURA, DaeGwi KIM, Naoteru SHIGEKAWA

The 46th IEEE Photovoltaic Specialist Conference (PVSC 46), 535 - Poster B1, June 16-21, 2019, CHICAGO, IL, USA.

We deposit Cd-based nanoparticles on Si solar cells using the layer-by-layer method and measure their current-voltage and spectral response characteristics. The solar cells covered by the nanoparticles show higher conversion efficiencies due to the interference of the layered nanoparticles. We also observe features indicating the energy absorbance of the nanoparticles in the reflectance of cells.

Direct bonding of diamond and Cu at room temperature for power device application

Jianbo LIANG, Shinji KANDA, Satoshi MASUYA (Univ. of SAGA), Makoto KASU (Univ. of SAGA), and Naoteru SHIGEKAWA

Extended Abstracts of 12th New Diamond and Nano Carbons Conference, S3-14-T (2019), Hualien, Taiwan.

Impurity distribution at Si/GaAs heterointerfaces fabricated by surface-activated bonding analyzed by atom probe tomography

Yasuo SHIMIZU (Univ. of Tohoku), Naoki EBISAWA (Univ. of Tohoku), Yutaka OHNO (Univ. of Tohoku), Jianbo LIANG, Naoteru SHIGEKAWA, Koji INOUE (Univ. of Tohoku), and Yasuyoshi NAGAI (Univ. of Tohoku)

Extended Abstracts of 2018 MRS Fall Meeting & Exhibit, 2018-11-28, Boston, USA.

p⁺-Si/AlGaIn/GaN HEMTs with Si/nitride bonding interface for high thermal tolerance

Shunichi KONO, Jianbo LIANG and Naoteru SHIGEKAWA

Extended Abstracts of International Workshop on Nitride Semiconductors 2018 (IWN2018), ThP-ED-10, Kanazawa, Japan.

TEM characterization of GaAs/GaN heterointerface fabricated by surface activated bonding

Shoji YAMAJO, Jianbo LIANG and Naoteru SHIGEKAWA

Extended Abstracts of International Workshop on Nitride Semiconductors 2018 (IWN2018), TuP-CR-18, Kanazawa, Japan.

Atom probe study of impurity distribution at Si/GaAs heterointerfaces fabricated by surface-activated bonding

Yasuo SHIMIZU (Univ. of Tohoku), Naoki EBISAWA (Univ. of Tohoku), Yutaka OHNO (Univ. of Tohoku), Jianbo LIANG, Naoteru SHIGEKAWA, Koji INOUE (Univ. of Tohoku), and Yasuyoshi NAGAI (Univ. of Tohoku)

Extended Abstracts of Summit of Materials Science 2018 (SMS2018), October 29-30, Sendai, Japan.

Low-Loss Characteristics of Metal-Foil-Based Passive Components by Surface-Activated Bonding Technologies

Keita MATSUURA, Jianbo LIANG, Koichi MAEZAWA (Univ. of Toyama), and Naoteru SHIGEKAWA

IEEE Transactions on Electron Devices 66, 3946 [7 pages] (2019).

Low-loss passive components for RF signals compatible with the on-wafer process are essential for realizing integrated circuits with high-frequency and high power operations. We successfully fabricate thick-metal film-based coplanar waveguides (CPWs) and inductors (INDs) by directly bonding a 17- μm -thick Al foil to a sapphire (0001) substrate and wet etching. The surface-activated bonding (SAB) technologies at room temperature are used. RF characteristics of the foil-based passive components are compared with those of components made of 1- μm thick evaporated Al layers. We obtain a better insertion loss and a higher Q-factor for foil-based CPWs and INDs, respectively. The measured characteristics are compared with those obtained by an analysis based on the equivalent circuit scheme. Impacts of side etching of foils and surface oxidation on their characteristics are observed. Characteristics of virtual components made of 1- μm -thick Al foils, i.e., 1- μm -thick Al films with the same resistivity as that of foils, are analytically investigated.

Macroscale synthesis of CuO nanowires on FTO plane substrate

Yota MABUCHI (Nagoya Institute of Technology), Rashid Norhana MOHAMED (Nagoya Institute of Technology), Xuyang LI (Nagoya Institute of Technology), Jianbo LIANG, Naoki KISHI (Nagoya Institute of Technology), and Tetsuo SOGA (Nagoya Institute of Technology)

Modern Physics Letters B 33, 1950138 [4 pages] (2019).

This study aims to fabricate copper oxide (CuO) nanowires by annealing a copper film formed on a charged film of fluorine-doped tin oxide (FTO). However, from the viewpoint of stress and growth of nanowires, it is difficult to mass-produce CuO nanowires on the entire region of the macro area on the plane substrate. In the proposed study, this was made possible by modifying the substrate's structure.

Annealing effect of surface-activated bonded diamond/Si interface

Jianbo LIANG, Yan ZHUO (Bristol Univ.), Satoshi MASUYA (Univ. of SAGA), Manikant SINGH (Bristol Univ.), James POMEROY (Bristol Univ.), Seongwoo KIM (Adamant Namiki Precision Jewel. Co., Ltd.), Martin KUBALL (Bristol Univ.), Makoto KASU (Univ. of SAGA), and Naoteru SHIGEKAWA

Diamond & Related Materials 93, 187-192 (2019).

From transmission electron microscope (TEM) observation, a 25 nm thick amorphous layer was confirmed at the diamond/Si bonding interface without annealing, the amorphous layer thickness decreased with the annealing temperature. No cracking even in nanometer scale occurred even after high-temperature annealing at 800 °C. From in-situ micro-Raman monitoring, the compressed stress was observed in the Si of the bonding interface without annealing with respect to the bonding Si substrate. A tensile stress relaxation was observed in the diamond of the bonding interface with respect to the polished diamond. These results were attributed to the large load applied to the diamond and Si substrates during bonding process. After annealing at 400 °C, the residual stress in the Si of the bonding interface decreased, while the residual stress in the diamond of the bonding interface increased, which should be due to the residual stress caused by the applied load was released by annealing process. The residual stress in the Si and diamond of the bonding interface increased and decreased, respectively, as the annealing temperature increased from 400 to 1000 °C. The main reason was due to the structure change of the amorphous layer and the tensile stress relaxation in the diamond of the bonding interface.

Stability of diamond/Si bonding interface during device fabrication process

Jianbo LIANG, Satoshi MASUYA (Univ. of SAGA), Seongwoo KIM (Adamant Namiki Precision Jewel. Co., Ltd.), Toshiyuki Oishi (Univ. of SAGA), Makoto KASU (Univ. of SAGA), and Naoteru SHIGEKAWA

Applied Physics Express 12, 016501-1 – 016501-5 (2019).

Diamond/Si bonding interface with an entire contact area and high thermal stability is achieved by surface activated bonding method. The fabrication of diamond field-effect transistors (FETs) on the diamond bonded to Si is demonstrated. The FET exhibits clear saturation and pinch-off characteristics. A 5-nm-thick $\text{Si}_x\text{C}_{x-1}$ layer was formed at the interface with annealing at 1000 °C. The layer was formed by the inter-diffusion of carbon and Si atoms near the bonding interface, which plays a role of residual stress relaxation between diamond and Si. These results suggest that diamond/Si heterostructures are applicable for combining diamond devices with Si LSI.

Hard X-ray photoelectron spectroscopy investigation of annealing effects on buried oxide in GaAs/Si junctions by surface-activated bonding

Shoji YAMAJO, Sanji YOON, Jianbo LIANG, Hassanet SODABANLU (Univ. of Tokyo), Kentaro WATABABE (Univ. of Tokyo), Masakazu SUGIYAMA (Univ. of Tokyo), Akira YASUIC (JASRI/Spring-8), Eiji IKENAGA (JASRI/Spring-8), Naoteru SHIGEKAWA

Applied Surface Science 473, 627-632 (2019).

Hard X-ray photoelectron spectroscopy measurements are performed on ≈ 10 -nm-thick GaAs film/Si substrate junctions fabricated by the surface activated bonding and selective wet etching. The chemical shifts of Ga-O and As-O signals in Ga $2p_{3/2}$ and As $2p_{3/2}$ core spectra indicate that oxides are formed in a part of GaAs films neighboring GaAs/Si interfaces due to the surface activation process. Analyses of Ga-O and As-O signals show that the thickness of such buried oxides is decreased due to a post-bonding annealing at temperatures up to 400°C. This means that the electrical properties of bonding interfaces, which are in the meta-stable states, are improved by the annealing. The thickness of oxides is different from that of amorphous-like transition layers at the GaAs/Si interfaces observed by transmission electron microscopy.

How Membrane Lipids Influence Plasma Delivery of Reactive Oxygen Species into Cells and Subsequent DNA Damage: An Experimental and Computational Study

Jonas Van der PAAL (University of Antwerp), Sung-Ha HONG (University of South Australia), Maksudbek YUSUPOV (University of Antwerp), Nishtha GAUR (University of South Australia), Jun-Seok OH, Robert D. SHORT (University of Lancaster), Endre J. SZILI (University of South Australia) and Annemie BOGAERTS (University of Antwerp)

Phys. Chem. Chem. Phys. Vol. 21, 19327 (15 pages) (2019)

The mechanisms of plasma in medicine are broadly attributed to plasma-derived reactive oxygen and nitrogen species (RONS). In order to exert any intracellular effects, these plasma-derived RONS must first traverse a major barrier in the cell membrane. The cell membrane lipid composition, and thereby the magnitude of this barrier, is highly variable between cells depending on type and state (e.g. it is widely accepted that healthy and cancerous cells have different membrane lipid compositions). In this study, we investigate how plasma-derived RONS interactions with lipid membrane components can potentially be exploited in the future for treatment of diseases. We couple phospholipid vesicle experiments, used as simple cell models, with molecular dynamics (MD) simulations of the lipid membrane to provide new insights into how the interplay between phospholipids and cholesterol may influence the response of healthy and diseased cell membranes to plasma-derived RONS. We focus on the (i) lipid tail saturation degree, (ii) lipid head group type, and (iii) membrane cholesterol fraction. Using encapsulated molecular probes, we study the influence of the above membrane components on the ingress of RONS into the vesicles, and subsequent DNA damage. Our results indicate that all of the above membrane components can enhance or suppress RONS uptake, depending on their relative concentration within the membrane. Further, we show that higher RONS uptake into the vesicles does not always correlate with increased DNA damage, which is attributed to ROS reactivity and lifetime. The MD simulations indicate the multifactorial chemical and physical processes at play, including (i) lipid oxidation, (ii) lipid packing, and (iii) lipid rafts formation. The methods and findings presented here provide a platform of knowledge that could be leveraged in the development of therapies relying on the action of plasma, in which the cell membrane and oxidative stress response in cells is targeted.

DOI: 10.1039/C9CP03520F

Development of an Ambient Air Flow Rotating Arc Jet for Low-Temperature Treatment

Vladislav GAMALEEV (Meijo University), Naoyuki IWATA (Meijo University), Jun-Seok OH, Mineo HIRAMATSU (Meijo University) and Masafumi ITO (Meijo University)

IEEE Access Vol. 7, 93100 (8 pages) (2019)

For low-temperature atmospheric pressure plasma treatment applications, we developed a novel rotating arc jet operated using various gases, including ambient air. We demonstrate the operation of plasma via the injection of various gas mixtures and tune operation parameters to achieve a low-temperature gas output from the arc jet. The rotating arc jet has an efficiency two orders of magnitude higher in the generation of reactive oxygen and nitrogen species than commercially available conventional nonequilibrium atmospheric pressure plasma jets operated with He or Ar gases. The high concentration of reactive species and use of ambient air as a process gas is promising for biomedical and agriculture applications. This work is a step toward the commercial use of plasma jets operated with ambient air.

DOI: 10.1109/ACCESS.2019.2928419

Rethinking Surface Reactions in Nanoscale Dry Processes toward Atomic Precision and beyond: A Physics and Chemistry Perspective

Kenji ISIKAWA (Nagoya Univ.), Tatsuo ISHIJIMA (Kanazawa Univ.), Tatsuru SHIRAFUJI, Silvia ARMINI (IMEC), Emilie DESPIAU-PUJO (Univ. Grenoble Alpes, CNRS), Richard A. GOTTSCHO (Lam Res. Corp.), Keren J. KANARIK (Lam Res. Corp.), Gert J. LEUSINK (TEL Technol. Cent., America, LCC), Nathan

MARCHACK (IBM T. J. Watson Res. Cent.), Takahide MARUYAMA (ULVAC Inc.), Yasuhiro MORIKAWA (ULVAC Inc.), Gottlieb S. OEHRLEIN (Univ. Mary Land), Sangwuk PARK (Samsung Electron. Co., Ltd.), Hisataka HAYASHI (Toshiba Memory Corp.), Keizo KINOSHITA (AIO Core Co., Ltd.)

Jpn. J. Appl. Phys., Vol. 58, SE0801 (14 pages) (2019)

In this review, we discuss the progress of emerging dry processes with atomic precision. Researchers in the field of plasma processing and surface science have addressed the increasingly challenging demands of material selectivity by utilization of synergistic enhancement of etching or deposition. The discussion encompasses major challenges in the plasma science and technology community. The focus of the review is advances in atomic layer etching and area-selective deposition with activation or deactivation, especially in terms of materials scaling and variety. Control of high-aspect-ratio feature fabrication in semiconductor manufacturing and etched shapes of interior features at the nanoscale are needed. Issues related to profile distortion have received much attention. State-of-the-art techniques used in semiconductor manufacturing are reviewed and future challenges are outlined. DOI: 10.7567/1347-4065/ab163e

Formation of Freestanding Thin Films on Liquid Surfaces: Printing on Liquid Surfaces

Tatsuru SHIRAFUJI

J. Print. Sci. Technol., Vol. 56, 181-187 (2019) (in Japanese)

Freestanding thin films have been used for various purposes such as for separation and wound dressing as well as applications in sensors, catalysts, supercapacitors, and artificial organs. Most of the freestanding thin films used in these applications are fabricated via the peeling-off of films that have been formed on solid substrates. In this review, we discuss possible methods and advantages of the direct formation of thin films on liquid surfaces without peeling-off processes; these methods are denominated as “printing on liquid surfaces.”

Reaction Kinetics of Active Species from an Atmospheric Pressure Plasma Jet Irradiated on the Flowing Water Surface —Effect of Gas-drag by the Sliding Water Surface—

Tatsuru SHIRAFUJI and Jun-Seok OH

J Photopolym Sci Technol. Vol. 32, 535 (6 pages) (2019)

We performed numerical simulations for investigating atmospheric pressure humid air chemistry triggered by metastable argon atoms fed from an atmospheric pressure plasma jet (APPJ) irradiated on a flowing water surface. We discuss the gas-drag effect caused by the flow of water surface. The gas-drag effect may alter spatial profiles of gas-phase species around the APPJ. It may alter also spatial profiles of the flux of active species impinging on the water surface. The numerical simulations have revealed that the flux profile of OH radicals is surely altered by the gas-drag effect and its flux on the surface is reduced to 1/6 of that on the static surface.

DOI: 10.2494/photopolymer.32.535

Investigation on the Long-Term Bactericidal Effect and Chemical Composition of Radical-Activated Water

Naoyuki IWATA (Meijo University), Vladislav GAMALEEV (Meijo University), Jun-Seok OH, Takayuki OHTA (Meijo University), Masaru HORI (Nagoya University) and Masafumi ITO (Meijo University)

Plasma Process Polym. Vol. 17, e1900023 (6 pages) (2019)

We treat deionized water using an atmospheric-pressure radical source to investigate the role of neutral radicals in the bactericidal efficacy of radical-activated water (RAW). The bactericidal efficacy of RAW is investigated using a colony forming unit assay with *Escherichia coli*. Both the bactericidal efficacy and reactive oxygen and nitrogen species (RONS) concentration in stored RAW are investigated over a period of a month. *E. coli* was completely sterilized even in RAW stored for 7 days, indicating the strong bactericidal effect. However, deterioration of the bactericidal efficacy of RAW stored for 14 days is confirmed, which does not have a clear correlation with the time evolution of the RONS concentration. This result becomes a strong evidence that RAW has long term bactericidal efficacy.

DOI: 10.1002/ppap.201900055

Simultaneous Achievement of Antimicrobial Property and Plant Growth Promotion Using Plasma- Activated Benzoic Compound Solution

Naoyuki IWATA (Meijo University), Vladislav GAMALEEV (Meijo University), Hiroshi HASHIZIME (Nagoya University), Jun-Seok OH, Takayuki OHTA (Meijo University), Kenji ISHIKAWA (Nagoya University), Masaru HORI (Nagoya University) and Masafumi ITO (Meijo University)

Plasma Process Polym. Vol. 17, e1900023 (6 pages) (2019)

This study assesses a potential use of the recently developed nonthermal atmospheric pressure plasma technology

in hydroponic plant cultivation. Two types of plasma - activated liquid solutions were compared, namely, L-Phenylalanine (L-Phe), which had a benzene ring structure, and L-Alanine (L-Ala), which did not have a benzene ring structure. Antimicrobial property and plant growth enhancement were simultaneously obtained when plasma-activated L-Phe was used. We found that the benzene ring structure in solution contributed to antimicrobial property. Further, colony forming unit assay indicated that 99% of *Escherichia coli* (*E. coli*) were eliminated after 24-h incubation and radish sprout growth increased by about 40% after 2 days of cultivation.

DOI: 10.1002/ppap.201900023

Tailoring the Chemistry of Plasma-Activated Water Using a DC-Pulse-Driven Non-Thermal Atmospheric-Pressure Helium Plasma Jet

Jun-Seok OH, Endre J. SZILI (University of South Australia), Akimitsu HATTA (Kochi University of Technology), Masafumi ITO (Meijo University) and Tatsuru SHIRAFUJI

Plasma, Vol. 2, 127 (10 pages) (2019)

We investigate the use of a DC-pulse-driven non-thermal atmospheric-pressure He plasma jet in the regulation of hydrogen peroxide (H_2O_2), nitrite (NO_2^-), nitrate (NO_3^-), and oxygen (O_2) in deionized (DI) water. The production of these molecules is measured by in situ UV absorption spectroscopy of the plasma-activated water (PAW). Variations in the pulse polarity and pulse width have a significant influence on the resultant PAW chemistry. However, the trends in the concentrations of H_2O_2 , NO_2^- , NO_3^- , and O_2 are variable, pointing to the possibility that changes in the pulse polarity and pulse width might influence other plasma variables that also impact on the PAW chemistry. Overall, the results presented in this study highlight the possibility of using DC-pulse-driven plasma jets to tailor the chemistry of PAW, which opens new opportunities for the future development of optimal PAW formulations across diverse applications ranging from agriculture to medicine.

DOI: 10.3390/plasma2020010

Plasma Polymerization Using Helium Atmospheric-Pressure Plasma Jet with Heptylamine monomer

Kyle G. DOHERTY (University of Liverpool), Jun-Seok Oh, Paul UNSWORTH (University of Liverpool), Carl M. SHERIDAN (University of Liverpool), Peter WEIGHTMAN (University of Liverpool), James W. BRADLEY (University of Liverpool), Rachel L. WILIAMS (University of Liverpool)

Plasma Process Polym. Vol. 16, e1800185 (10 pages) (2019)

Atmospheric-pressure plasma jets can be used to modify surfaces in a spatially-defined manner. Operating these jets in air is an efficient surface modification tool, however the resulting surface chemistries are limited by the plasma gases. In this study we demonstrate that plasma polymerization with heptylamine on polystyrene (PS) surfaces, using an atmospheric pressure plasma jet (APPJ), can enable mammalian cell attachment and growth. Importantly, the addition of the heptylamine monomer, in a helium carrier-gas, altered the spatially-defined treatment area in comparison to treatment with a helium plasma alone.

DOI: 10.1002/ppap.201800185

Modulating the Concentrations of Reactive Oxygen and Nitrogen Species and Oxygen in Water with Helium and Argon Gas and Plasma Jets

Kotaro OGAWA (Kochi University of Technology), Jun-Seok OH, Nishtha GAUR (University of South Australia), Sung-Ha HONG (University of South Australia), Hirofumi KURITA (Toyohashi University of Technology), Akira MIZUNO (Toyohashi University of Technology), Akimitsu HATTA (Kochi University of Technology), Robert D. SHORT (University of South Australia, University of Lancaster), Masafumi ITO (Meijo University) and Endre J. SZILI (University of South Australia)

Jpn. J. Appl. Phys., Vol. 58, SAAB01 (9 pages) (2019)

We employed UV-vis spectroscopy to monitor real-time changes in the oxygen tension and concentration of reactive oxygen and nitrogen species (RONS) in deionized (DI) water during treatments with helium (He) and argon (Ar) gas plasma jets. He and Ar gas jets are both shown to deoxygenate DI water with He being more efficient than Ar, whilst the plasma jets deliver and regulate the concentrations of hydrogen peroxide (H_2O_2), nitrite (NO_2^-) and nitrate (NO_3^-) in DI water. The H_2O_2 and NO_3^- production efficiency varied between He and Ar plasma jets, but was similar for NO_2^- . Whilst DI water fully equilibrated with ambient air prior to treatment (de-oxygenated by both plasma jets) when DI water was first de-oxygenated by an inert gas jet treatment, both plasma jets were found to be capable of oxygenating DI water. These insights were then used to show how different combinations of plasma jet and inert gas jet treatments can be used to modulate O_2 tension and RONS chemistry. Finally, potential further improvements to improve control in the use of plasma jets in regulating O_2 and RONS are discussed.

DOI: 10.7567/1347-4065/aaea6b

Effects of Sheath Gas Flow on He Atmospheric Pressure Plasma Jet

Kotaro OGAWA (Kochi University of Technology), Hideki YAJIMA (ORC Manufacturing), Jun-Seok OH, Hiroshi FURUTA (Kochi University of Technology) and Akimitsu HATTA (Kochi University of Technology)

Appl. Phys. Express, Vol. 12, 036001 (5 pages) (2019)

It was demonstrated that employing a sheath gas flow was effective in the formation of long laminar flow of He jet without turbulence by matching the gas velocities at the boundary between the He core jet and the N₂ sheath gas flow. With the extension of He laminar flow, the plume length of plasma was significantly extended to more than 20 mm at a 0.5-slm flow rate of He. The irradiation area for the direct plasma treatment of the target was clearly limited within 2 mm even at a 10-mm distance from the target.

DOI: 10.7567/1882-0786/aafde9

The Dependence of Nonlinear Electrical Properties of Yeast Suspensions on Temperature and Electrode Shape

Keita TAMURA, Masafumi MURAJI, Kenji TANAKA, and Tatsuru SHIRAFUJI

IEEJ Transactions on Fundamental and Materials, Vol.139, No.8, pp339-344 (2019)

We observed the temperature dependence of nonlinearity in the response waveform from a yeast suspension when an alternating current (AC) voltage was applied. This observation is based on repeatable data of nonlinearity measured over time. The nonlinearity in the response of the living yeast suspension was unique, and a relationship between this nonlinearity and the growth state of yeast was identified. We suggest that this nonlinearity reflects the electrical properties inherent in living organisms. Measuring the nonlinearity of the yeast suspension response and accounting for temperature permits us to rapidly distinguish between living and dead yeast. Moreover, we found that the nonlinearity depended on the shape of the electrodes. For each electrode shape, we investigated the effects of field intensity and its distortion on the nonlinearity of the response using a computer simulation. We suggest that the nonlinearity is strongly related to the field intensity and its distortion near the electrodes.

DOI: 10.1541/ieejfms.139.339

A Novel Eye Tracking System to Expand Viewing Area in All Directions for Glasses-Free 3D Display Displayable in Both Portrait and Landscape Modes

Hiroyuki NAKAMURA, Goro HAMAGISHI, Kayo YOSHIMOTO, Hideya TAKAHASHI, Takuya MATSUMOTO, and Kaoru KUSAFUKA

Proc. The International Display Workshops, Nagoya, Dec. 11, Vol.25, pp.792-795 (2018).

We have previously proposed the see-through retinal projection type super multi-view head-mounted display (HMD). The smooth motion parallax provided by the super multi-view technique enables a precise superposition of virtual 3D images on real scene. Moreover, if a viewer focuses one's eyes on the displayed 3D image, the stimulus for the accommodation of human eye is reproduced naturally. To realize the super multi-view condition, multiple parallax images must be projected onto the retina. However, in the previous proposed HMD, since the respective parallax images were spatially divided and were projected onto the retina, the image resolution was low and the optical system was complicated. In order to overcome these problems, we propose the improved see-through retinal projection type super multi-view HMD by using the time division projection optical system. The proposed HMD consists of a multiple exposure holographic lens with multi-convergence points, a high frame rate display device, and a high-speed optical shutter. Multiple parallax images are displayed by time division and are converged on respective points by the holographic lens. The optical shutter which synchronized to the display device passes only one convergence light corresponding to the right parallax image. Therefore, proposed HMD realizes the pseudo super multi-view condition and displays the virtual image at the distance within ability for focusing on the human eye. To verify the effectiveness of the proposed HMD, we confirmed the depth range of the 3D image by the prototype of the proposed HMD was more than 250 mm in front of the pupil.

Vessel position estimation system based on pixel-wise refocusing using light field imaging

Kayo YOSHIMOTO, Hideya TAKAHASHI, and Kenji YAMADA (Osaka University)

Proc. SPIE Advanced Biomedical and Clinical Diagnostic and Surgical Guidance Systems XVII, San Francisco, Feb. 26, Vol.10868, 108681M, CD-ROM (2019).

Venipuncture is a medical practice which is ordinarily performed in hospital. However, it is a difficult procedure as the occurrence of many failure of the puncture and sometimes medical accidents such as nerve damage and blood vessel damage are reported. This is caused by the difficulty of visually identification of the blood vessel. Although the depth information of the blood vessel is also important, the existing system in clinical practice can visualize vessels only by two dimensional images. In our previous study, to estimate the three dimensional position of the blood vessel, we have proposed the system based on refocusing using light field imaging. This method can obtain cross-sectional information of blood vessel emphasized using near infrared light at each depth. However, under the influence of the strong scattering characteristics of living tissue, vascular fluoroscopic images obtained using infrared light are blurred. This is because the light scattered from other paths overlaps with the light traveling straight through the influence of blood vessel absorption. In order to suppress this blur, a system for removing scattered light is constructed. In order to eliminate the influence of scattering, a method of angular filtering using a lens array is adopted. Since this method uses lens arrays, it has high affinity with refocusing technology. First, we organize the expression related our proposed system. Then, evaluate the basic principles of the proposed system by using blood vessel simulated object.

Analysis of displayable depth range for retinal projection type super multi-view 3D head-mounted display using the time division projection optical system

Hiroaki MAEDA, Junya KOHNO, Kayo YOSHIMOTO, and Hideya TAKAHASHI

Proc. SPIE Advanced in Display Technologies IX, San Francisco, Mar. 1, Vol.10942, 109420X, CD-ROM (2019).

We have previously proposed the retinal projection type super multi-view head-mounted display (HMD) using the time division projection optical system. By using the super multi-view HMD, it is possible to provide the viewer with the three-dimensional (3D) image that induces the accommodation of a human eye naturally. In order to realize the super multi-view method, it is necessary to simultaneously project multiple parallax images on the retina. However, when the parallax between each parallax image is large and the

corresponding pixels of each parallax image on the retina do not overlap each other, the retinal image is observed as multiple projection images, therefore the accommodation cannot be induced. In this paper, to estimate the displayable range of 3D image of the proposed super multi-view HMD, we revealed the relationship between the number of parallax images and the displayable range of 3D image by using Gullstrand's schematic eye model and the analysis of the light intensity distributions of retinal images. In order to verify the displayable range of 3D image, we constructed the prototype HMD which projected five parallax images on the retina. We confirmed that the displayable range of 3D image of the prototype HMD is from 900 mm to 2000 mm in front of human eye. By clarifying the relationship between the number of parallax images and the displayable range of 3D image, it is possible to freely design the display range of 3D image of the retinal projection type super multi-view HMD.

3D display with active parallax barrier using the monochromatic LC panel of specifications same as the image display panel

Tomoya TSUJINO, Hiroyuki NAKAMURA, Takuya FUJISHIMA, Goro HAMAGISHI, Kayo YOSHIMOTO, Hideya TAKAHASHI, Takuya MATSUMOTO, and Kaoru KUSAFUKA

Proc. SPIE Advanced in Display Technologies IX, San Francisco, Mar. 1, Vol.10942, 1094211, CD-ROM (2019).

In the stereoscopic 3D display using the parallax barrier, the active barrier method can expand the viewing area if the barrier pattern optimizes corresponding to the position of the observer by eye tracking. However, requiring not only the LC display panel but also the specially shaped LC panel for the active barrier, this system should be very expensive. We propose using the active barrier which is a monochromatic panel of the same pixel shape as the image display panel. In the proposed method, it is easy to manufacture panels for the active barrier, and the 3D display provide the wide viewing area and high quality 3D images for observers. When the active barrier is a monochromatic panel having the same pixel shape as the image display panel, basically the barrier pitch cannot realize the ideal value. Thus, the observer cannot observe the stereoscopic image in the full screen. In order to realize stereoscopic observation, we apply the cycle pitch composing the stereoscopic image. The cycle pitch composing the stereoscopic image is the method to bring the pitch constituting the L/R image closer to the ideal value by periodically increasing the number of dots constituting the L/R image. To confirm the effectiveness of the proposed method, the crosstalk of the prototypes using film barriers were measured. Crosstalk was less than or equal to 10% at the viewing distance of 421 mm to 1238 mm. That crosstalk can be reduced regardless of observation distance was confirmed.

A novel control method of the combination of simple active barrier pitch control and image processing to extremely expand the viewing zone in forward and backward directions of stereoscopic 3D displays

Takuya FUJISHIMA, Hiroyuki NAKAMURA, Tomoya TSUJINO, Goro HAMAGISHI, Kayo YOSHIMOTO, Hideya TAKAHASHI, Takuya MATSUMOTO, and Kaoru KUSAFUKA

Proc. SPIE Advanced in Display Technologies IX, San Francisco, Mar. 1, Vol.10942, 109420M, CD-ROM (2019).

We have previously proposed eye tracking system to expand viewing area in all directions for glasses-free 3D display. In this system, since the parallax barrier was fixed, the viewing zone was expanded by image processing corresponding to the viewing position. Thus, there was a limit to expanding the viewing zone only by image processing. On the other hand, we can expand the viewing zone by applying an active barrier that changes to the optimum barrier pattern corresponding to the viewing position by eye tracking. However, to change the active barrier pattern, complex calculation and a specially designed active barrier LC panel are required. To overcome this problem, we propose a novel control method to expand the viewing zone of stereoscopic 3D displays with active parallax barrier in depth direction. The proposed method is the combination of the simple generation method of a barrier pattern and the synthesis method of Left/Right synthetic image corresponding to the viewing position. In this method, let the optimum barrier pitch be B_p at the viewing distance d , we set the barrier pitch to $x \cdot B_p$ and synthesize the Left/Right image so that crosstalk is low at the same time at the viewing distance d/x . To verify the effectiveness of the proposed method, we measured the crosstalk of the prototype 3D display. The crosstalk ratios at the optimum viewing distance 1092 mm (d), 774 mm ($d \cdot 3/4$) and 546 mm ($d \cdot 1/2$) were 4.28%, 3.82% and 5.02%, respectively. Therefore, low crosstalk 3D images could be observed.

A Clue to High Rate Capability of Lithium-Ion Batteries Obtained by an Electrochemical Approach Using “Diluted” Electrode

Kingo ARIYOSHI, Satoshi MIZUTANI, Tomoya MAKINO, and Yusuke YAMADA

J. Electrochem. Soc., Vol. 165, pp. A3965-A3970 (2018)

Rate capability of “diluted” electrodes composed of micron-sized particles of an active material, $\text{Li}[\text{Li}_{0.1}\text{Al}_{0.1}\text{Mn}_{1.8}]\text{O}_4$ (LAMO), and a spectator material, Al_2O_3 , were investigated to determine the rate-limiting step during discharge accompanied with lithium insertion. Capacity retention based on the LAMO-weight specific current density (C-rate) was significantly improved by reducing LAMO contents in the diluted electrodes, whereas no significant difference was found in capacity retention based on area specific current density. These results indicate that the rate-limiting step during discharge is not Li-ion diffusion in the active materials, but the transportation of Li cations and counter anions in the electrodes. Comparison of amounts of Li^+ ions inserted to LAMO during charge with that supplied from an electrolyte indicated that rate capability can be improved by increasing the amount of Li ions in the pore of the electrode. The comparison also suggests that transportation of the counter anion causing concentration overvoltage limits the rate capability.

Measurement of Side-Reaction Currents on Electrodes of Lithium-Ion Cells Using a Battery Cycler with a High-Precision Current Source

Kingo ARIYOSHI, Yuki FUKUNISHI, and Yusuke YAMADA

Electrochemistry, Vol. 87, pp. 188-192 (2019)

Capacity fading mainly caused by state-of-charge deviations between the positive and negative electrodes of lithium-ion batteries (LIBs) can be accurately predicted if the rates of side reactions occurring on these electrodes are known. Herein, we show that the rates of side reactions on LIB electrodes can be determined using an in-house built high-current-precision battery cycler comprising galvanostat, charge/discharge control, and current switching units. An $\text{Li}[\text{Li}_{1/3}\text{Ti}_{5/3}]\text{O}_4/\text{Li}[\text{Li}_{1/3}\text{Ti}_{5/3}]\text{O}_4$ (LTO/LTO) symmetric cell is used to verify that the battery cycler provides currents accurate enough to determine side-reaction rates, and the rates of side reactions on LTO (negative) and LiNiMO (positive) electrodes in an LTO/ LiNiMO cell are compared with intrinsic values obtained for the symmetric cell.

$\text{Li}_2\text{Ni}_{0.2}\text{Co}_{1.8}\text{O}_4$ Having a Spinel Framework as A Zero-Strain Positive Electrode Material for Lithium-Ion Batteries

Kingo ARIYOSHI, Yuki ORIKASA, Kensuke KAJIKAWA, and Yusuke YAMADA

J. Mater. Chem. A, Vol. 7, pp. 13641-13649 (2019)

Zero-strain insertion materials are ideal electrode materials for lithium-ion batteries because they do not undergo dimensional change during lithium insertion and extraction. Herein, a zero-strain insertion material, Ni-substituted $\text{Li}_2\text{Co}_2\text{O}_4$ ($\text{Li}_2\text{Ni}_{0.2}\text{Co}_{1.8}\text{O}_4$) having a spinel framework, was synthesized and characterized to study the zero-strain mechanism. The change in the lattice dimensions of $\text{Li}_2\text{Ni}_{0.2}\text{Co}_{1.8}\text{O}_4$ during lithium extraction was very small (only 0.1%), confirming that $\text{Li}_2\text{Ni}_{0.2}\text{Co}_{1.8}\text{O}_4$ is a zero-strain insertion material. It had a flat voltage profile at 3.5 V with a reversible capacity of 100 mA h g^{-1} , which was quite different from the voltage profile of LiCoO_2 having a layered structure. Detailed structural analysis by X-ray absorption spectroscopy revealed that there was no dimensional change because the changes in two crystallographic factors, contraction of the Co–O bond and distortion of the oxygen sublattice, cancelled out. The zero-strain lithium-ion battery combined with $\text{Li}_2\text{Ni}_{0.2}\text{Co}_{1.8}\text{O}_4$ and $\text{Li}[\text{Li}_{1/3}\text{Ti}_{5/3}]\text{O}_4$ showed good cyclability.

Rate Capability of Carbon-Free Lithium Titanium Oxide Electrodes Related to Formation of Electronic Conduction Paths Observed by Color Change

Kingo ARIYOSHI, Takaya INO, and Yusuke YAMADA

J. Power Sources, Vol. 430, pp. 150-156 (2019)

Lithium titanium oxide prepared by the hydrogen reduction synthesis of $\text{Li}[\text{Li}_{1/3}\text{Ti}_{5/3}]\text{O}_4$ (LTO) exhibits electronic conductivity. The product demonstrated a superior rate capability than pristine LTO upon the examination of a pellet electrode in the absence of conductive additives. The rate capability of the pristine LTO pellet electrode is poor during the oxidation reaction due to low electronic conductivity of the electrode originated from insufficiently developed electronic conduction paths. In contrast, the rate

capability during the reduction reaction is improved due to the formation of electronic conduction paths resulting from transformation to the electronic conductor LTO during the reduction process. Visual inspection indicated that the formation and loss of electronic conduction paths in the electrode are key to determining the rate capability of the LTO pellet electrode in the absence of a conductive additive. Our results confirmed that this LTO exhibiting an electronic conductivity maintains an electronic conduction path in the pellet electrode in the absence of a conductive additive during the redox reaction, thereby resulting in an improved rate capability in both the oxidation and reduction reactions

Electrochemical Impedance Analysis of $\text{Li}[\text{Li}_{0.1}\text{Al}_{0.1}\text{Mn}_{1.8}]\text{O}_4$ Used as Lithium-Insertion Electrodes by the Diluted Electrode Method

Kingo ARIYOSHI, Satoshi MIZUTANI, and Yusuke YAMADA

J. Power Sources, Vol. 435, p. 226810 (2019)

Electrochemical impedance analysis was performed for $\text{Li}[\text{Li}_{0.1}\text{Al}_{0.1}\text{Mn}_{1.8}]\text{O}_4$ (LAMO) used as a lithium-insertion electrode by the diluted electrode method to identify the origin of resistance. Utilization of diluted electrodes, in which some portion of active material, LAMO, was systematically replaced with the same amounts of spectator Al_2O_3 material to maintain the original structure of the LAMO electrode, is a promising method to discriminate between the resistance attributed to the lithium-insertion reaction in LAMO (charge-transfer resistance) and that accompanied by conduction of electron and/or ion in the porous electrodes. Electrochemical impedance spectra of the diluted electrodes consisted of two semicircles. The radius of a semicircle in the lower frequency region depends on the LAMO content in a diluted electrode, indicating that the semicircle is associated with charge transfer resistance. On the other hand, the radius of the other semicircle in the higher frequency region is independent of the LAMO contents, suggesting that the semicircle is mainly related to the resistance accompanied by the porous structure of electrodes. Thus, the structure of lithium-insertion electrode should be carefully considered in designing high-energy and high-power lithium-ion batteries that employ thick electrodes.

Degradation Mechanism of LiCoO_2 under Float Charge Conditions and High Temperatures

Motoyuki HIROOKA, Tomohito SEKIYA, Yoshitomo OMOMO, Masayuki YAMADA, Hideaki KATAYAMA, Takefumi OKUMURA, Yusuke YAMADA, and Kingo ARIYOSHI

Electrochim. Acta, Vol. 320, p. 134596 (2019)

Lithium-ion batteries (LIBs) consisting of LiCoO_2 and graphite electrodes exhibit a trade-off relationship between their reversible capacity and cycle/calendar life in terms of the charge cut-off voltage. That is to say, a higher charge cut-off voltage leads to a larger reversible capacity and shorter cycle life. In order to develop LIBs that satisfy both performance criteria (*i.e.*, have a high reversible capacity as well as a long cycling life), the degradation mechanism of the LiCoO_2 electrode under float charge conditions and high temperatures is investigated while focusing on the relationship between the structural deterioration of the electrode and capacity fading. Durability tests performed on graphite/ LiCoO_2 cells under float charge conditions (4.4 V at 60 °C) induced a drop in the open-circuit voltage as well as capacity fading in the LiCoO_2 electrode along with the dissolution of a large number of cobalt ions. Acoustic emission histometry, X-ray diffraction, and transmission electron microscopy analyses of the LiCoO_2 electrode after the float charge tests revealed that the degradation of the LiCoO_2 electrode during the float charge tests occurred as per the following steps: (1) the HF generated by the decomposition of LiPF_6 reacts with the charged LiCoO_2 electrode, (2) the charged LiCoO_2 electrode is disproportionated into CoO_2 and Co^{2+} ions, and finally (3) the CoO_2 having an O1 structure decomposes into cobalt oxides containing cobalt ions in a lower oxidation state, which is associated with the evolution of oxygen gas.

Comparative Measurements of Side-Reaction Currents of $\text{Li}[\text{Li}_{1/3}\text{Ti}_{5/3}]\text{O}_4$ and $\text{Li}[\text{Li}_{0.1}\text{Al}_{0.1}\text{Mn}_{1.8}]\text{O}_4$ Electrodes in Lithium-Ion Cells and Symmetric Cells

Kingo ARIYOSHI, Yuki FUKUNISHI, and Yusuke YAMADA

J. Electrochem. Soc., Vol. 166, pp. A3314-A3318 (2019)

Lithium-ion batteries using $\text{Li}[\text{Li}_{1/3}\text{Ti}_{5/3}]\text{O}_4$ and $\text{Li}[\text{Li}_{0.1}\text{Al}_{0.1}\text{Mn}_{1.8}]\text{O}_4$ (LTO/LAMO) are very attractive for long-life and highpower applications. Capacity fading of the batteries mainly results from the deviation in the state of charges (SOCs) of LTO and LAMO electrodes caused by the difference in the side reaction currents of the electrodes. In this study, “real” and “intrinsic” side reaction currents are

measured in LTO/LAMO cells and symmetric cells of LTO/LTO and LAMO/LAMO, respectively. An observed significant difference in the side reaction currents is affected by the coupled electrode. The real side reaction currents for both electrodes are a few times larger than the intrinsic side reaction currents at any temperature, which can be explained by taking into account the influence of oxidation (or reduction) products generated at the positive (or negative) electrode on the negative (or positive) electrode. A mechanism of the side reaction inside the cell is proposed to explain the above phenomenon. The mechanism indicates the importance for understanding the “secondary” effects of side reactions, which are influenced by decomposition products on the other electrode, in addition to “primary” effects of side reactions such as the formation of solid electrolyte interphase.

Unique Half Embedded/Exposed PdFeCu/C Interfacial Nanoalloy as High-Performance Electrocatalyst for Oxygen Reduction Reaction

Biraj Jyoti BORAH, Himadri SAIKIA, Chiranjita GOSWAMI, Kumar Kashyap HAZARIKA, Yusuke YAMADA, and Pankaj BHARALI

ChemCatChem, Vol. 11, pp. 3522-3529 (2019)

Design of high-performance non-Pt electrocatalyst for fuel cell applications is greatly anticipated. Herein, we have developed a unique half-embedded and half-exposed interfacial PdFeCu nanoalloy anchored onto carbon matrix. The stable electronic coupling between the carbon matrix and PdFeCu nanoalloy possess very fast interfacial electron transfer which in turn enhances the electron conductivity. This makes the trimetallic

nanoalloy high performing oxygen reduction reaction (ORR) electrocatalyst in both basic and acidic media. The PdFeCu/C nanoalloy exhibits enhanced electrochemically active surface area than various PdFe/C bimetallics as well as benchmark 20 wt% Pt/C and Pd/C. As a result, it offers larger active sites for ORR and eased the electron transport during the electrocatalysis. It exhibits 1.5- and 2.4-fold higher mass activity in

comparison to the Pt/C and Pd/C. Furthermore, it exhibits long term stability and low onset potential compared to those of the other catalysts. Thus, the present investigation shows potential strategy for the design and synthesis of Pt-free electrocatalyst with remarkable catalytic activity and stability.

Technologies for Utilization of Hydrogen Peroxide as Energy Carrier

Yusuke YAMADA

Chemical Engineering, Vol. 64, pp. 466-470 (2019) (in Japanese)

Hydrogen peroxide is a potential chemical not only as a selective oxidant in various chemical processes but also as an energy carrier. Hydrogen peroxide can be produced by selective two-electron reduction of molecular oxygen abundant in air using natural energy such as solar energy. Also, hydrogen peroxide can be used as a fuel of direct hydrogen peroxide fuel cells for electric power generation.

Elemental Analysis of Three Kinds of Teas by Tabletop XRF Analyzer

Jingyuan ZHU, Haruna TAKAHASHI, Kouichi TSUJI

Memoirs of the Faculty of Engineering Osaka City University, Vol.59, pp.1-5 (2018).

In this research, we investigated three kinds of tea samples by using tabletop XRF analyzer JSX-1000S (JEOL Company, Japan). Each tea sample was tested in original state, powder state and tablet state with different mass values. We could show the minimum mass for quantitative XRF analysis. By analyzing the X-ray spectrum recorded for these samples, we found the possibility of XRF analysis as a method of tea quality control and detecting tea producing area.

X-Ray Fluorescence and Emission: X-ray Fluorescence Theory

Kouichi TSUJI

Encyclopedia of Analytical Science 3rd Edition, edited by P. Worsfold, C. Poole, A. Townshend, M. Miró, Elsevier, Vol. 10, pp. 471-481 (2019).

X-ray fluorescence (XRF) spectrometry is an analytical technique used widely for elemental determinations in both industrial, and research and development laboratories. It belongs to a family of atomic spectrometry techniques but enjoys some distinctive analytical advantages compared with rival techniques, such as atomic absorption spectrometry (AAS) and inductively coupled plasma–atomic emission spectrometry (ICP–AES).

X-Ray Fluorescence and Emission: Wavelength Dispersive X-Ray Fluorescence

Kouichi TSUJI

Encyclopedia of Analytical Science 3rd Edition, edited by P. Worsfold, C. Poole, A. Townshend, M. Miró, Elsevier, Vol. 10, pp. 459-470 (2019).

The analytical capabilities of X-ray fluorescence (XRF) have been recognized since the work of Moseley, who, in 1913 and 1914, published papers describing the systematic variation in fluorescence wavelength with atomic number and used this observation to characterize the elemental composition of brass. However, the performance of early instrumentation was restricted by various technical difficulties, and it was not until 1948 that the prototype of the first commercial wavelength dispersive (WD)-XRF instrument was described by Friedman and Birks. Commercial instrumentation became available during the mid-1950s and was progressively adopted by laboratories involved in elemental analysis of a range of sample types.

X-Ray Fluorescence and Emission: Energy Dispersive X-Ray Fluorescence

Philip J. POTTS, Kouichi TSUJI

Encyclopedia of Analytical Science 3rd Edition, edited by P. Worsfold, C. Poole, A. Townshend, M. Miró, Elsevier, Vol. 10, pp. 420-431(2019).

Although the principles and mechanism of excitation for energy dispersive X-ray fluorescence (ED-XRF) are exactly the same as for wavelength dispersive (WD)-XRF, the analytical characteristics of ED-XRF instrumentation demonstrate some significant differences, largely due to the different response characteristics of an ED detector. Traditionally, ED detectors were popularly associated with the Si(Li) detector (lithium-drifted silicon). However, although Si(Li) remains the standard against which other detector types are compared, technological advances have led to the introduction of alternative detector types, not the least the silicon PIN diode, the silicon drift detector (SDD), as well as germanium, mercury(II) iodide, and other semiconductor devices.

Obituary

Kouichi TSUJI

Adv. X-Ray. Chem. Anal., Japan, Vol.50, pp.1-5 (2019) (in Japanese).

Prof. Kichinosuke Hirokawa, emerits at KINKEN, Tohoku Univ., passed away on August 28, 2018 at the age of 85. He was awarded by the Zuiho Chujusho on 2013. His main research results on atomic spectroscopy, XRF, GDS, XPS, surface analysis were introduced.

“Advances in X-Ray Chemical Analysis, Japan” Edited by “The Discussion Group of X-Ray Analysis, The Japan Society for Analytical Chemistry”

Kouichi TSUJI

Adv. X-Ray. Chem. Anal., Japan, Vol.50, pp.7-10 (2019) (in Japanese).

Elemental Distribution Analysis of Copper-based Preservative-treated Woods by Micro XRF Method

Momotaro NAKANISHI, Hitomi NAKANO, Yuko FUJIWARA, Yosihisa FUJII, Kouichi TSUJI

Adv. X-Ray. Chem. Anal., Japan, Vol.50, pp.105-112 (2019) (in Japanese).

Wood is useful as construction material; however, wood is not strong for decay and insect damages. Generally, injecting copper-based preservative treatment is effective for these damages. However, in some cases, the amount of injection treatment is not enough and homogenous in wood. In previous studies, wood samples had been cut to confirm Cu distribution in the samples. Analytical method for investigating the injection amount of Cu is required in non-destructively and non-contact way. In this study, we attempted to acquire elemental distribution in wood by using micro XRF method. European red pine (*Pinus sylvestris*) wood was measured by micro XRF instrument manufactured in the laboratory. XRF images of Cu, Ca, and K were measured on the surface and cross section of the wood sample. It was found that the injection depth of copper depended on the structure of wood. In addition, the detection efficiency of Cu fluorescent X-rays was evaluated according to Lambert-Beer's law and compared with the experimental result.

Development of X-Ray Analytical Microscope for Painting Using Long Working Distance Mono-Capillary

Hitomi NAKANO, Mai SAKAGUCHI, Takuma AMPO, Shintaro KOMATANI, Sumito OHZAWA, Yoko IWASAKI, Moe KONDO, Kaori TAGUCHI, Naoyoshi MORI, Kouichi TSUJI

Adv. X-Ray. Chem. Anal., Japan, Vol.50, pp.151-160 (2019) (in Japanese).

A nondestructive and noncontact analytical method has been required for measurement of arts and paintings, in order not to hurt the samples. X-ray fluorescence analysis (XRF) is one of suitable techniques for this purpose. To obtain elemental images, a micro-XRF spectrometer was developed using an X-ray micro beam. In order to measure paintings safely, we developed an X-ray mono-capillary focusing device with a long working distance. In this paper, we report obtained for Vincent van Gogh's painting arts at POLA museum collection by using the X-ray analytical microscope.

Confocal Micro XRF Monitoring of Microbially Influenced Corrosion Process of Steel Samples

Jigi CHIN, Ryohei HOSOMI, Hiroshi KAWAKAMI, Kouichi TSUJI

Adv. X-Ray. Chem. Anal., Japan, Vol.50, pp.169-175 (2019) (in Japanese).

X-ray fluorescence analysis (XRF) is a non-destructive method. There is a lot of applications like analysis of industrial material. A confocal micro XRF instrument enables elemental analysis of point-limited region. The confocal micro XRF instrument was applied to in situ analysis of microbiologically influenced corrosion process. Finally, it was realized to visualize Fe distribution corroded from steel sample in the solution.

Proposal of Elemental Determination Method of Human Hairs by Using Tabletop X-Ray Fluorescence Analyzer

Takumi FURUSATO, Fumiyuki INOUE, Kouichi TSUJI

Adv. X-Ray. Chem. Anal., Japan, Vol.50, pp.177-184 (2019) (in Japanese).

Minerals play a great role in the human body. Therefore, it is important to know the excess or deficiency of minerals for health examination. However, the mineral concentrations in the blood are kept constant due to homeostasis, therefore blood tests cannot give us the abnormality. On the other hand, since hair takes in and holds mineral information, it is possible to examine the mineral concentrations in the body by measuring the hair itself. Therefore, we decided to study element determination method in hair more easily and quickly than ICP-AES/MS analysis. In this study, we considered a scattered X-ray internal standard method using a tabletop X-ray fluorescence analyzer. As a result, S, Ca, Zn in the hair could be quantified. However, for elements with small content such as Ca and Zn, the dispersion in quantitative value became larger. Also, since it depends on the sample form, it was found that preparation method of hair sample is important.

67th Annual Denver X-Ray Conference [DXC] Report

Tetsuya YONEDA, Kouichi TSUJI

Adv. X-Ray. Chem. Anal., Japan, Vol.50, pp.67-70 (2019) (in Japanese).

Report on EXRS 2018 (European Conference on X-Ray Spectrometry) and X-Ray Research Trend

Yukie IZUMOTO, Tsugufumi MATSUYAMA, Hiroshi YOSHII, Kouichi TSUJI

Adv. X-Ray. Chem. Anal., Japan, Vol.50, pp.71-78 (2019) (in Japanese).

Progress and Application Examples of X-Ray Fluorescence Elemental Imaging Analysis Technology

Masaki YAMANASHI, Aoi YAMAUCHI, Kouichi TSUJI

Bunseki Vol.2019 (4), pp.146-153 (2019) (in Japanese).

X-ray fluorescence (XRF) is well known as a nondestructive elemental analysis technique under atmospheric pressure. In recent years, advances in X-ray optical elements and two-dimensional detectors have enabled XRF imaging to obtain element distribution information in a large region in samples. This paper mainly describes the elemental technologies related to XRF imaging with X-ray optics and two-dimensional detector, and shows applications by this laboratory systems using them. In addition, XRF image processing using compressed sensing is also introduced.

Multi-Modal Compositional Analysis of Layered Paint Chips of Automobiles by the Combined Application of ATR-FTIR Imaging, Raman Microspectrometry, and SEM/EDX

Md Abdul MALEK, Takashi NAKAZAWA, Hyun-Woo KANG, Kouichi TSUJI, Chul-Un RO

Molecules, Vol.24, pp.1381 (2019).

For the forensic analysis of multi-layered paint chips of hit-and-run cars, detailed compositional analysis, including minor/trace chemical components in the multi-layered paint chips, is crucial for the potential credentials of the run-away car as the number of layers, painting process, and used paints are quite specific to the types of cars, color of cars, and their surface protection depending on the car manufacturer and the year of manufacture, and yet overall characteristics of some paints used by car manufacturers might be quite

similar. In the present study, attenuated total reflectance-Fourier transform infrared (ATR-FTIR) imaging, Raman microspectrometry (RMS), and scanning electron microscopy/energy-dispersive X-ray spectrometric (SEM/EDX) techniques were performed in combination for the detailed characterization of three car paint chip samples, which provided complementary and comprehensive information on the multi-layered paint chips. That is, optical microscopy, SEM, and ATR-FTIR imaging techniques provided information on the number of layers, physical heterogeneity of the layers, and layer thicknesses; EDX on the elemental chemical profiles and compositions; ATR-FTIR imaging on the molecular species of polymer resins, such as alkyd, alkyd-melamine, acrylic, epoxy, and butadiene resins, and some inorganics; and RMS on the molecular species of inorganic pigments (TiO_2 , ZnO , Fe_3O_4), mineral fillers (kaolinite, talc, pyrophyllite), and inorganic fillers (BaSO_4 , $\text{Al}_2(\text{SO}_4)_3$, $\text{Zn}_3(\text{PO}_4)_2$, CaCO_3). This study demonstrates that the new multi-modal approach has powerful potential to elucidate chemical and physical characteristics of multi-layered car paint chips, which could be useful for determining the potential credentials of run-away cars.

Evaluation of Full-Field Energy Dispersive X-Ray Fluorescence Imaging Apparatus and Super Resolution Analysis with Compressed Sensing Technique

Aoi YAMAUCHI, Masanori IWASAKI, Kazunori HAYASHI, Kouichi TSUJI

X-Ray Spectrometry, DOI: 10.1002/xrs.3055 (2019)

A full-field energy dispersive X-ray fluorescence (FF-EDXRF) imaging spectrometer that utilizes single-photon counting analysis with a charge-coupled device was developed in our laboratory.

We evaluated the developed spectrometer with respect to its energy resolution, spatial resolution, quantitative performance, and elemental imaging and compared it with the corresponding characteristics of scanning-type EDXRF spectrometers. In addition, we demonstrate that the limit of detection and sensitivity deteriorate as the analytical area decreases. Finally, compressed sensing, which is a widely used information-processing technique, was applied for clearing XRF images.

In Situ Observation of Corrosion Process of Steel Sheet Under Stress Load by Confocal Micro X-Ray Fluorescence Imaging

Kouichi TSUJI, Ryohei HOSOMI

Tetsu-to-Hagané, Vol.105, pp.975-980 (2019) (in Japanese).

Details of corrosion process of the steel sheet under stress load in the solutions have not been understood well. In this case, it is important to observe the corrosion process in liquid solutions by using nondestructive analytical method. Therefore, we applied a confocal micro-XRF analytical method for this purpose. This method enables a nondestructive elemental imaging near the surface of the materials in the solution. We prepared a sample cell where a Zn plating steel sheet was placed under stress load in NaCl solution. Zn and Fe XRF images were successfully observed in situ for 5 days in two analytical modes: cross sectional XRF imaging and depth-selective XRF imaging.

Development of Cu/Ni Binary Catalyst for Hydrothermal Oxidation of Refractory Compounds

Noritsugu KOMETANI, and Masaaki NARITA

Proceedings of 12th International Symposium on Supercritical Fluids, Paper ID: OI04 (2018)

We have reported that Cu-based materials show a remarkable catalytic effect for the treatment of refractory organic compounds such as chlorophenol and trichloroethylene by catalytic hydrothermal oxidation, because of enhanced generation of hydroxyl radicals through Fenton-like reaction catalyzed by Cu(I) ion under hydrothermal condition. Here, we report that Cu/Ni binary catalyst exhibits a higher activity than Cu for the hydrothermal oxidation of 3,4-dichlorophenol. It is indicated by EXAFS data that the atomic interaction between Cu and zero-valent Ni may accelerate Fenton-like reaction, resulting in enhanced degradation and mineralization of 3,4-dichlorophenol.

Oxygen additive effects on decomposition rate of poly(vinyl phenol)-based polymers using hydrogen radicals produced by a tungsten hot-wire catalyst

Masashi YAMAMOTO, Shiro NAGAOKA, Keisuke OHDAIRA, Hironobu UMEMORO, Hideo HORIBE

Thin Solid Films, Vol. 679, pp. 22–26 (2019)

For fabricating semiconductor devices and for microelectromechanical systems, photoresists are important materials supporting photolithography processes. However, photoresists must be removed for subsequent processes. An earlier study demonstrated that adding a small amount of oxygen gas to the atmosphere in which hydrogen radicals are produced increased the decomposition rate of a positive-tone novolac

photoresist. For this study, we prepared polymers with different side chain structures based on poly(vinyl phenol) (PVP). We examined the effects of added oxygen and the oxygen-added hydrogen radicals on the decomposition rates of PVP-based polymers. Hydroxyl groups of PVP are partly substituted with *tert*-butoxycarbonyl groups in order to use for base polymer of KrF photoresist. Results show that oxygen addition can be useful for KrF photoresist removal.

Dynamics of the phase separation in a thermoresponsive polymer: accelerated phase separation of stereo-controlled poly(*N,N*-diethylacrylamide) in water

Mitsuhiro MATSUMOTO, Takanori TADA, Taka-aki ASOH, Tatsuya SHOJI, Takashi NISHIYAMA, Hideo HORIBE, Yukiteru KATSUMOTO, Yasuyuki TSUBOI

Langmuir Vol. 34(45), pp. 13690–13696 (2018)

We studied the dependence on tacticity of the dynamic phase separation behavior of thermoresponsive poly(*N,N*-diethylacrylamide) (PDEA) in an aqueous solution. Using a laser temperature-jump technique combined with transient photometry, we determined the time constants of the phase separation and found that both atactic and isotactic-rich PDEAs had fast and slow phase separation processes (τ_{fast} and τ_{slow}). The fast process (τ_{fast}) was independent of the tacticity, irrespective of the concentration. On the other hand, the slow process had a strong dependence on the tacticity. We found the slow phase separation process got considerably faster with increasing isotacticity in dilute solutions. This effect due to the tacticity of the PDEA is totally different from that of poly(*N*-isopropylacrylamide) and can be explained on the basis of the difference between the hydrophobicity of atactic PDEA and that of isotactic-rich PDEA.

Oxidative Decomposition of Organic Compounds by Ozone Microbubbles in Water

Yuta KODA, Terumi MIYAZAKI†, Eriko SATO, Hideo HORIBE

J. Photopolym. Sci. and Technol., Vol. 32(4), pp. 615-618 (2019)

Oxidative degradation of poly(ethylene glycol) (PEG) by ozone microbubbles (O3MBs) was investigated in water. Ozone water are generally effective in oxidation reaction with a variety of organic compounds. O3MBs have promise to improve the efficiency because it seems that O3MBs generates hydroxy radicals, resulting in the higher active oxidative degradation. Herein, oxidative decomposition of PEG by O3MBs in water was carried out and the products were characterized by 1H nuclear magnetic resonance (NMR) and matrix assisted laser desorption/ionization fourier transform ion cyclotron resonance mass spectrometry (MALDI-FT-ICR-MS). Through the continuous struggles, decomposition of PEG was promoted by O3MBs. It was found that O3MBs with hydrogen peroxide added had the largest decomposition effect. The reason has been veiled yet, however, the author reasons that O3MBs have promise as the novel degradation system.

Relationship between Oxygen Additive Amount and Photoresist Removal Rate Using H Radicals Generated on an Iridium Hot-Wire Catalyst

Masashi YAMAMOTO, Tomohiro SHIROI, Tomokazu SHIKAMA, Shiro NAGAOKA, Hironobu UMEMOTO, and Hideo HORIBE

J. Photopolym. Sci. and Technol., Vol. 32(4), pp. 609–615 (2019)

We examined an environmentally friendly photoresist removal method using radicals produced by decomposing mixtures of hydrogen and oxygen on a hot iridium catalyst. We earlier reported that the decomposition of photoresists was hastened by adding oxygen gas to a hydrogen flow using a tungsten hot-wire catalyst. The rate increased with the oxygen additive amount up to about 1.0% and then decreased gradually. The decrease is caused by the catalytic poisoning of O atoms on the catalyst surface because of its poor oxidation resistance. In present study, we show that oxygen addition without catalytic poisoning is effective to increase the decomposition rate. The poisoning can be avoided by using an Ir catalyst. The decomposition rate showed an Arrhenius-type dependence on the substrate temperature. The rate increased rapidly with increasing amounts of added oxygen to 1.0% and then the increase became more gradual. OH radicals must play an important role to hasten the decomposition reactions.

A Comparison of Removal Phenomena in Photoresist Materials Using Laser Irradiation

Tomosumi KAMIMURA, Naoki NISHIOKA, Yuji UMEDA, Daichi SHIMA, Yusuke FUNAMOTO, Yoshiyuki HARADA, Masashi YOSHIMURA, Ryosuke NAKAMURA, Hideo HORIBE

J. Photopolym. Sci. and Technol., Vol. 32(4), pp. 603–607 (2019)

Resist removal phenomena using laser irradiation were compared in the novolak resist and the PVP. Thresholds for stripping from the Si wafer and damaged at the Si wafer were evaluated for the laser

irradiating condition in the normal atmosphere and in the water. The PVP was found to be easy to be stripped as compared with the novolak resist. Only in the water, the photoresist material was completely stripped from the Si wafer surface. The size of the changed area by the laser irradiation for the PVP was approximately 2 times larger than that of the novolak resist. Time-resolved images were also acquired in 400 ns and 7500 ns after the laser irradiation. The scattering condition of the PVP in the removal process was completely different from that of the novolak resist.

Formation of a single poly(*N,N*-diethylacrylamide) micro-droplet in water by coupling of photothermal effects and an optical force

Mitsuhiro MATSUMOTO, Taka-aki ASOH, Tatsuya SHOJI, Takashi NISHIYAMA, Hideo HORIBE, Yukiteru KATSUMOTO, Yasuyuki TSUBOI

J. Phys.: Conf. Ser. Vol. 1220, Article No. 012034 (2019)

Poly(*N*-isopropylacrylamide) (PNIPAM) exhibits phase separation with lower critical solution temperature (LCST). In the 1990s, Masuhara and co-workers reported the first demonstration of optical trapping of PNIPAM forming a micrometer-sized polymer droplet. Since then, this technique has attracted much attention to create a molecular assembly in a microspace. In the present study, we targeted poly(*N,N*-diethylacrylamide) (PDEA), which has an analogous chemical structure to PNIPAM. We demonstrated that optical tweezers formed the unique micro-morphologies of a phase separated PDEA droplet. Fluorescence microscopic images and Raman spectra of the PDEA droplet showed that a lot of smaller-sized water-rich micro-domains were inhomogeneously formed in the droplet. Such unique phase separation behavior was never observed in steady-state heating of an aqueous PDEA solution above its LCST. Our results indicate that a novel micro-structure can be formed by coupling of an optical gradient force and a local temperature elevation.

Photoresist removal using hydrogen radicals produced by tantalum hot-wire catalyst

Masashi YAMAMOTO, Tomohiro SHIROI, Tomokazu SHIKAMA, Shiro NAGAOKA, Hideo HORIBE

AIP Conf. Proc., Vol. 2151, Article No. 020010 (2019)

Photoresist removal method using hydrogen radicals produced by decomposing hydrogen on a hot-wire catalyst is one of an environmentally friendly methods. We examined the relationship between photoresist removal rate and its surface temperature and the surface element analysis for a tantalum catalyst. In this study, we considered an adaptability of the catalyst to the removal.

Coumarin Derivative Polymers for Thermo- and Light- Responsive Monofunctional Polymers: Effect of Additives on Thermo-Responsivity

Eriko SATO

AIP Conf. Proc., Vol. 2040, Article No. 0200026 (4 pages) (2018)

Methacrylic and acrylic homopolymers containing a coumarin unit in the side-chain, which undergoes reversible [2+2] cycloaddition by photoirradiation, are the very limited examples of the dual-stimuli responsive monofunctional polymers. The coumarin derivative polymers show lower critical solution temperature-type phase separation in some chlorinated organic solvents such as chloroform. In this study, the control of the cloud points of the coumarin derivative polymers by the addition of low-molecular-weight additives to the solution was investigated. It was revealed that the addition of low-molecular-weight compounds, which would interact with the coumarin derivative polymers, such as coumarin, 3,4-dihydrocoumarin, chromone, and 9-bromoanthracene resulted in significant increase in the cloud points. It was also found that the cloud points of the coumarin derivative polymer can be controlled by the addition amount of the additives up to near the boiling point of the solvent.

Regiospecificity of Alternating Copolymerization of Cyclic Conjugated Dienes and Oxygen

Eriko SATO, Shuji TAKETANI, Chisato OMORI, Hideo HORIBE and Akikazu MATSUMOTO

Chem. Lett., Vol. 48(5), pp. 445-448 (2019)

Alternating radical copolymerization of cyclic conjugated diene monomers, i.e., cyclopentadiene and furan, with oxygen were carried out to generate degradable polyperoxides. The cyclopentadiene and furan based-polyperoxides consisted of different regiospecific structures. The regiospecificity of the alternating copolymerization was rationalized by the bond dissociation energies of the carbon-to-oxygen bond of the peroxy radicals based on density functional theory calculations. The thermal degradation behavior of the resulting cyclic conjugated diene-based polyperoxides was also investigated.

Reductants for Polyperoxides to Accelerate Degradation at Elevated Temperatures

Eriko SATO, Michihiro YURI, Akikazu MATSUMOTO and Hideo HORIBE

Polym. Degrad. Stab., Vol. 162, pp. 47-54 (2019)

The alternating copolymer of a conjugated diene monomer and oxygen, i.e., polyperoxide, is a mainchain degradable polymer and undergoes radical chain degradation by heating. During the degradation process, oxygen-centered radicals are formed and thus side reactions such as hydrogen abstraction from the polymer by the oxygen-centered radicals and subsequent coupling, which prevent the degradation, sometimes take place. In this study, in order to promote the degradation of polyperoxides only at elevated temperatures while maintaining their stability at ambient temperature, appropriate organic reductants, which do not significantly react with the polyperoxides at 30 °C but react at 100 °C, were explored. N,N-Dimethylaniline, which is a conventional reductant for redox initiation systems, initiated the redox degradation of cyclopentadiene-based polyperoxides even at 30 °C due to the very high nucleophilicity. The introduction of an electron donating group at the para position, i.e., 4-dimethylaminoacetophenone, 4-dimethylaminobenzaldehyde, and 4-dimethylaminobenzonitrile, successfully maintained the stability of the polyperoxide at 30 °C and accelerated the degradation at 100 °C due to the reduced nucleophilicity. Similar results were obtained by using 1-acetyl-2-phenylhydrazine and 1-phenyl-3-pyrazolidone (PhP) as a reductant, and PhP resulted in the most significant acceleration effect at 100 °C. The activation energy for the overall degradation of the polyperoxide in the presence of PhP was much lower than that of the polyperoxide in the absence of a reductant. In the case of sorbic ester-based polyperoxides, their stabilities at 30 °C were not maintained in the presence of the reductants and the stability was improved by increasing the 2,5 structure regarding the diene moiety in the main-chain.

Thermal Latent Reductants for Controlled Degradation of Polyperoxides and Their Application to High Performance Dismantlable Adhesives

Eriko SATO, Chisato OMORI, Michihiro YURI, Yuta KODA and Hideo HORIBE

ACS Appl. Polym. Mater., Vol. 1(8), pp. 2140-2148 (2019)

1-Phenyl-3-pyrazolidone (PhP) having an active hydrogen was blocked by phenyl isocyanate derivatives to reduce its nucleophilicity, and the potential of the blocked PhP as a thermal latent reductant generating the organic reducing agent, PhP, was revealed for the first time. The degree of dissociation of the blocked PhP during heating in solution can be controlled by the steric hindrance of the isocyanate-blocking agents. The thermal latency of the blocked PhP for the sorbic ester-based polyperoxides, which undergo a serious reductive decomposition by PhP even at 30 °C, was investigated to accelerate the decomposition of the polyperoxides only at elevated temperatures. It was revealed that the stability of the polyperoxides was not significantly affected at 30 °C, and marked reductive decomposition of the polyperoxides together with thermal decomposition took place at elevated temperatures. For the block PhPs, which are highly compatible with the polyperoxides, the decomposition promotion effect increased with increasing the steric hindrance of the blocking agents, and the controlled decomposition of the polyperoxides was successfully achieved. Moreover, the addition of the blocked PhP resulted in the complete solubilization of sorbic ester-based cross-linked polyperoxides by heating, which was not able to be achieved without the blocked PhP. The performance of the debondable adhesive by using the sorbic ester-based cross-linked polyperoxides was improved by the addition of the blocked PhP, although hazardous isocyanate formation during the activation process may limit the practical application. Specifically, a faster decrease in the lap-shear adhesion strength by heating was accomplished. Furthermore, the same level of dismantlability was achieved in the wide range of heating temperatures and time, which is an important requirement for polyperoxides undergoing significant exothermic decomposition bringing about undesired temperature rise.

Control of Droplet Movement on a Plate with Micro-wrinkle by Difference of Wettability

Kenji KATO, Eriko SATO, Shinya YOSHIOKA and Tatsuro WAKIMOTO

Exp. Fluid., Vol. 60, Article No. 140 (11 pages) (2019)

In this study, we consider the control of a liquid droplet movement rolling down on an inclined plate with gravitational force using a micro-wrinkle on a wall. The micro-wrinkle was manufactured by the buckling of a thin polymer film (poly(*N*-vinylcarbazole), PVK) on a base polymer (poly(vinyl chloride), PVC). The PVC was stretched once and then PVK (~ 100 nm thickness) was spin-coated on the surface of the base polymer at ambient temperature. When the strain was released in a thermostatic chamber heated above the glass transition temperature of PVC, a two-dimensional micro-wrinkle having a wavelength of several micrometers was formed on the surface. The advancing and receding contact angles were measured in

directions parallel and perpendicular to the wrinkle. It was observed that there were several degrees of contact angle anisotropy. When the droplet was set on the wrinkle surface inclined at 45° to the gravitational force, the direction of droplet movement could be changed by ~ 20° from the gravitational direction. The deflection angle was estimated from a theoretical model with the principle of minimum work of the contact line.

(This is identical to the abstract that appeared in the section of Mechanical and Physical Engineering)

Facile Synthesis of Graft Copolymers Containing Rigid Poly(dialkyl fumarate) Branches by Macromonomer Method

Eriko SATO, Noboru TAMARI and Hideo HORIBE

J. Polym. Sci.: Part A, Polym. Chem., in press. doi.org/10.1002/pola.29499

Graft copolymers show microphase separated structure as seen in block copolymers and have lower intrinsic viscosity than block copolymers because of a branching structure. Therefore, considering molding processability, especially for polymers containing rigid segments, graft copolymers are useful architectures. In this work, graft copolymers containing rigid poly(diisopropyl fumarate) (PDiPF) branches were synthesized by full free-radical polymerization process. First, synthesis of PDiPF macromonomers by addition-fragmentation chain transfer (AFCT) was investigated. 2,2-Dimethyl-4-methylene-pentanedioic acid dimethyl ester was found to be an efficient AFCT agent for diisopropyl fumarate (DiPF) polymerization because of the suppression of undesired primary radical termination, which significantly took place when common AFCT agent, methyl 2-(bromomethyl)acrylate, was used. Copolymerization of PDiPF macromonomer with ethyl acrylate accomplished the generation of the graft copolymer having flexible poly(ethyl acrylate) backbone and rigid PDiPF branches. The graft copolymer showed a microphase separated structure, high transparency, and characteristic thermal properties to PDiPF and poly(ethyl acrylate).

Functionalization of Network Polymers Based on Reaction Control

Eriko SATO

Journal of Network Polymer, Japan, Vol. 40(1), pp. 30-36 (2019) (in Japanese)

Network polymers show excellent properties such as a high mechanical strength and solvent resistance. On the other hand, the removal of network polymers is difficult due to insolubility. In order to solve the issue, de-cross-linkable network polymers have attracted much attention. In this review, the design of network polymers having degradable units is introduced with focusing on the main-chain degradable polyperoxides-based network polymers and curable hyperbranched polymers having dense degradable linkages. Curable adhesives are one of the applications of network polymers, and de-cross-linkable network polymers can be used as dismantlable adhesives, which demonstrate both sufficient bonding strength in use and easy debonding on demand. Increase in bonding strength by the network formation and debonding by decreasing a mechanical strength and solubilization in response to de-cross-linking are reported.

Design of Dismantlable Adhesives Using Reactive Polymers

Eriko SATO

Journal of The Adhesion Society of Japan, Vol. 55(3), pp. 111-118 (2019) (in Japanese)

Dismantlable adhesives, which achieve enough adhesion strength in use and easy debonding on demand, have attracted much attention from industrial and academic perspectives. Dismantlable adhesives are one of promising materials and technology for resource and energy savings. In this review article, the examples of dismantlable adhesives based on various stimuli-responsive polymeric materials were introduced. Especially, design and development of dismantlable adhesives using reactive polymers, such as degradable polymers, cross-linkable polymers, and side-chain reactive polymers, were explained in detail.

Intrinsically permeable polymer vesicles based on carbohydrate-conjugated poly(2-oxazoline)s synthesized using a carbohydrate-based initiator system

Tomoki NISHIMURA, Naoki SUMI, Yuta KODA, Yoshihiro SASAKI, Kazunari AKIYOSHI

Polym. Chem., Vol. 10, pp. 691-697 (2019)

Polymer vesicles with molecular permeability offer significant potential to contribute to the understanding of biocatalytic processes in nano/micro compartments and therapeutic enzyme reactors. However, constructing such permeable vesicles remains challenging, as clear guidelines for the design of permeable membranes

remain elusive. In the present study we focused on a hydrophobic polymer with hydrogen bond donor and acceptor moieties, i.e., a polymer that exhibits a lower-critical-solution-temperature (LCST)-like behavior, as a suitable component for the permeable bilayer membrane. We have developed a carbohydrate-based initiator system for the cationic ring opening polymerization of 2-oxazoline and synthesized molecular permeable polymer vesicles based on an amphiphilic block polymer composed of maltotriose and poly(*n*-propyl oxazoline) that exhibit LCST-like behavior. The resulting polymer vesicles are permeable to up to 1 kg mol⁻¹ of FITC-PEG. These findings represent a major milestone toward the development of (i) intrinsically permeable polymer vesicles and (ii) functional polymer vesicles for a broad range of fundamental and biomedical applications.

Amphiphilic Poly[poly(ethylene glycol) methacrylate]s with OH Groups in the PEG Side Chains for Controlling Solution/Rheological Properties and toward Bioapplication

Yuta KODA, Daiki TAKAHASHI, Yoshihiro SASAKI, Kazunari AKIYOSHI

ACS App. Bio Mater., Vol. 2, pp. 1920-1930 (2019)

Poly[poly(ethylene glycol) methacrylate]s with OH groups on the PEG side chains [poly(PEGOHMA)s] were synthesized using ruthenium-catalyzed living radical polymerization (Ru-LRP) to diversify the polymer design of PEGylated methacrylate-based copolymers. Poly(PEGOHMA)s could not be prepared using the approach previously reported for the synthesis of poly[poly(ethylene glycol) methyl ether methacrylate [poly(PEGMA)]; therefore, the polymerization was adapted for poly(PEGOHMA)s. As a result, both homopolymerization and random and block copolymerization of PEGOHMA with other hydrophobic monomers were successfully achieved, resulting in the preparation of amphiphilic random block and star polymers. The solution and bulk properties of PEGOHMA-based (co)polymers were markedly different from those of PEGMA-based (co)polymers. By reacting the OH groups with biotin, protein–poly(PEGOHMA) conjugates were successfully prepared; however, it was not possible to prepare protein–polymer conjugates using terminal biotinylated PEGMA-based copolymers, owing to the steric hindrance of the unreactive PEG side chains.

Unnatural Oligoaminosaccharides with *N*-1,2-Glycosidic Bonds Prepared by Cationic Ring-Opening Polymerization of 2-Oxazoline-Based Heterobicyclic Sugar Monomers

Yuta KODA, Takaya TERASHIMA, Makoto OUCHI

ACS Macro Lett., Vol. 8, pp. 1456-1460 (2019)

Glycoligomers and glycopolymers (glycocompounds) play important roles in maintaining homeostasis in biological systems. Glycobiology is a burgeoning area in the elucidation of biological systems for which the molecular design of glycocompounds requires further diversification, including both natural and unnatural glycocompounds. Herein, we proposed a synthesis strategy based on the chain polymerization of deliberately designed sugar monomers. Unnatural oligoaminosaccharides comprising *N*-1,2-glycosidic bonds were synthesized without enzymes through the cationic ring-opening polymerization of 2-oxazoline-based heterobicyclic sugar monomers. To achieve this, a heterobicyclic monomer [Glc(MeOx)], comprising protected glucosamine (GlcN) and 2-methyl-2-oxazoline (MeOx) rings, was designed. This monomer was polymerized using a binary initiating system of tert-butyl iodide (*t*-BuI) and GaCl₃ to afford oligo[Glc(MeOx)]. The resulting structure corresponded to the condensation product of GlcN with *N*-1,2-glycosidic bonds. After deprotection of oligo[Glc(MeOx)], the resulting oligoaminosaccharide had a secondary structure different to that of protected oligo[Glc(MeOx)]. Owing to the *N*-1,2-glycosidic bonds, the oligoaminosaccharide was not degraded by chitinase, which hydrolyzes the condensation product of GlcN with *O*-1,4-glycosidic bonds.

Crystallization-Induced Emission of 1,2-Bis(3-methyl-5-(4-alkylphenyl)-2-thienyl)perfluorocyclopentenes: A Mechanical and Thermal Recording System

Tatsumoto NAKAHAMA, Daichi KITAGAWA, Hikaru SOTOME, Syoji ITO, Hiroshi MIYASAKA, Seiya KOBATAKE

Dyes and Pigments, Vol. 160, pp. 450-456 (2019)

Organic luminescent materials have attracted much attention due to potential application to organic optoelectronics. Search for new molecules with high fluorescence quantum yield in solid states is one of the most important tasks in the research field of the organic luminescent materials. Here, we newly synthesized diarylethenes, 1,2-bis(3-methyl-5-(4-alkylphenyl)-2-thienyl)perfluorocyclopentenes having methyl, ethyl, *n*-propyl, and *n*-butyl substituents at the *p*-position of phenyl rings, and investigated their fluorescence

properties in the solid states. The diarylethenes in the crystalline phase exhibited strong fluorescence with relatively high fluorescence quantum yields (Φ_f) of 0.12–0.20 compared with those in the amorphous phase ($\Phi_f = 0.064$ –0.069), which indicates that the diarylethenes have crystallization-induced emission (CIE) characteristics. The diarylethene having methyl group as the alkyl chain has the highest Φ_f value among the diarylethenes that we synthesized in this work. We found that the amorphous solid of the diarylethene having methyl group was crystallized after mechanical scratching followed by heating at 90 °C. We successfully demonstrated reversible fluorescence recording based on CIE characteristics and mechanical scratching and heating induced crystallization.

Solid Emission Color Tuning of Polymers Consisting of BODIPY and Styrene in Various Ratios

Katsuya SHIMIZU, Daichi KITAGAWA, Seiya KOBATAKE

Dyes and Pigments, Vol. 161, pp. 341-346 (2019)

Random copolymers (poly(BO_x-co-St_y)) consisting of boron dipyrromethene (BODIPY) monomer (BO) and styrene (St) were synthesized to achieve multi-color and efficient emission in the solid state using St as a spacer. The emission color of the resulting copolymers changed from green to red by changing the content of BO from 0.042 to 100 mol%. Fluorescence quantum yield (Φ_f) also increased with the content of St ($\Phi_f = 0.05$ –0.88) because the intermolecular distance between the BO fluorophores became longer. The absorption and fluorescence properties of the copolymers in tetrahydrofuran were similar and independent of the compositional ratios, and Φ_f was relatively high (0.65–0.81), which indicates that the intermolecular interaction between BO fluorophores in the same polymer chain is small due to the lack of BO fluorophore aggregation. However, emission color changes in the bulk powder were mainly derived from the intermolecular interaction between BO fluorophores in inter-polymer chains because the polymers were intertwined with each other in the solid state. When the polymers in the solid state were annealed, the emission spectra were red-shifted and Φ_f decreased. It was concluded that the emission color changes of the polymers were mainly induced by intermolecular interaction between BO fluorophores in the inter-polymer chains.

Hybrid Organic-Inorganic Photon-Powered Actuators Based on Aligned Diarylethene Nanocrystals

Xinning DONG, Fei TONG, Kerry M. HANSON, Rabih O. AL-KAYSI, Daichi KITAGAWA, Seiya KOBATAKE, Christopher J. BARDEEN

Chem. Mater., Vol. 31(3), pp. 1016-1022 (2019)

When photochromic molecules are organized in a crystal, the small-scale forces generated by molecular photoisomerization events can combine together to generate work on micro- or macroscopic length scales. In this work, photomechanical nanocrystals themselves are organized on macroscopic length scales using a porous inorganic template. The organic diarylethene component provides the reversible photoresponse, whereas the porous alumina component provides structural support and directionality. This hybrid organic–inorganic photomechanical material acts as a bending actuator. Using ultraviolet and visible photons as power inputs, as little as 0.1 mg of reacted material generates enough force to tilt a 1.28 g mirror and steer a laser beam. The motion can be cycled multiple times in air and under water. Actuator figures-of-merit such as energy-to-work conversion efficiency and stiffness are probably limited by the high elastic modulus of the inorganic template, providing an obvious pathway for optimization.

1,2-Diarylbenzene as Fast T-type Photochromic Switch

Daichi KITAGAWA, Tatsumoto NAKAHAMA, Yoshihiro NAKAI, Seiya KOBATAKE

J. Mater. Chem. C, Vol. 7(10), pp. 2865-2870 (2019)

Fast T-type photochromic molecules that isomerize only under photoirradiation are promising materials for ophthalmic lenses, real-time holography, security systems, and super-resolution fluorescence microscopy. In this study, we successfully developed a novel fast T-type photochromic molecular system, 1,2-diarylbenzene (DAB), by introducing tetrafluorobenzene to the ethene bridge unit of the typical P-type photochromic diarylethene. DAB changed from colorless to blue only when irradiated with ultraviolet light because it underwent photocyclization and fast thermal cycloreversion with a half-life of 130 ms at room temperature. The dramatic acceleration of thermal cycloreversion was due to the significant increase in the energy gap between the open- and closed-ring isomers and decrease in activation energy at the ground state. In addition, DAB could undergo fast photochromic reaction even in the solid state. Thus, introduction of a benzene ring to the ethene bridge unit would lead to the development of new functions for 6 π -electron photochromic systems.

Cyclization Reaction Dynamics of an Inverse Type Diarylethene Derivative as Revealed by Time-Resolved Absorption and Fluorescence Spectroscopies

Hikaru SOTOME, Daichi KITAGAWA, Tatsumoto NAKAHAMA, Syoji ITO, Seiya KOBATAKE, Masahiro IRIE, Hiroshi MIYASAKA

Phys. Chem. Chem. Phys., Vol. 21(17), pp. 8623-8632 (2019)

Photocyclization reaction dynamics of an inverse type diarylethene derivative was investigated in alkane solutions by means of ultrafast laser spectroscopies. Femtosecond transient absorption spectroscopy showed that the Franck-Condon state formed by photoexcitation is geometrically relaxed to a transient species within 100 fs and subsequently the cyclization process takes place with a time constant of 36 ps. This time constant is much longer than those in normal type derivatives. Steady-state and time-resolved fluorescence measurements with the aid of quantum chemical calculations revealed that there exist three kinds of conformers, one parallel and two anti-parallel forms, in the ground state. One of the anti-parallel conformers undergoes the cyclization reaction, while the other two conformers are nonreactive species and their major relaxation processes are radiative decay and intersystem crossing into the triplet states. The triplet states thus formed no longer undergo the cyclization reaction in the late time region.

Plasmon Enhanced Optical Responses of Diarylethene Molecules Adsorbed on Gold Nanorods

Syogo NODA, Seiju HASEGAWA, Hiroyuki HAMADA, Seiya KOBATAKE, Kohei IMURA

Chem. Lett., Vol. 48(6), pp. 537-540 (2019)

Assemblies of gold nanorods capped with poly-diarylethene (DE) were chemically prepared in a solution. Plasmon assisted optical responses of the poly(DE) have been studied. Fluorescence from the open-form of DE was mostly quenched near 550nm due to interband transition of gold, while fluorescence near 700 nm was slightly enhanced by the longitudinal plasmon resonance. Cycloreversion reaction of the gold nanorod-poly(DE) has been also studied, and it has been found that the reaction rate is enhanced by the plasmon excitation and increases nearly two-fold in the assembly. The magnitude of the enhancement is qualitatively consistent with the spatially and orientationally averaged value of the simulated optical field enhancements in the vicinity of the nanorod.

Photomechanical Bending Behavior of Photochromic Diarylethene Crystals Induced under Polarized Light

Akira HIRANO, Daichi KITAGAWA, Seiya KOBATAKE

CrystEngComm, Vol. 21(15), pp. 2495-2501 (2019)

Materials that change their shape by external stimuli have been attracting much attention as artificial mesoscopic actuators. In particular, photoresponsive molecular crystals are promising materials as photoactuators. Although many kinds of crystals exhibiting photomechanical motions have been reported so far, in many cases, light is irradiated to the crystal homogeneously. The details of the effect of irradiation conditions have not been specifically examined. Herein, the effect of polarized ultraviolet (UV) light on the photomechanical bending motion of diarylethene crystals was investigated. The bending speed upon polarized UV light irradiation depended on the polarization angle. The dependence of the bending speed was well correlated with the absorption anisotropy of the open-ring isomer in the crystal, which indicates that the photochromic reaction depth from the crystal surface played an important role in controlling the bending speed.

Efficient “Turn-off” Fluorescence Photoswitching in a Highly Fluorescent Diarylethene Single Crystal

Sanae ISHIDA, Daichi KITAGAWA, Seiya KOBATAKE, Sunnam KIM, Seiji KURIHARA, Tuyoshi FUKAMINATO

Chem. Commun., Vol. 55(40), pp. 5681-5684 (2019)

A highly fluorescent diarylethene single crystal was successfully designed and prepared. The crystal shows efficient “turn-off” fluorescence photoswitching with full reversibility. This might have originated from the amplified fluorescence quenching due to the intermolecular energy transfer process in the densely packed and well-ordered single crystal.

Photoreversible Interference Color Modulation to Multicolor in Photochromic Molecular Crystals

Kohei MORIMOTO, Hajime TSUJIOKA, Daichi KITAGAWA, Seiya KOBATAKE

Bull. Chem. Soc. Jpn., Vol. 92(8), pp. 1299-1304 (2019)

Functional molecular crystals responsive to external stimuli represent a new frontier for material chemistry

and crystal engineering. Here, we report on the photoreversible interference color change in single crystals composed of a photochromic diarylethene derivative, 1,2-bis(2-ethyl-5-phenyl-3-thienyl)perfluorocyclopentene. When the crystal was observed by rotating the sample stage at 45° from the extinction position under crossed Nicols, it showed an interference color. Upon irradiation with ultraviolet light, the interference color changed dramatically and instantaneously in response to photoirradiation due to the photocyclization reaction from the open-ring form to the closed-ring form. The change was quite sensitive to the photochromic reaction. It is attributable to the large decrease in retardation induced by the photocyclization reaction in crystals. These results might provide new opportunities for application of photochromic crystals.

Effects of Template and Molecular Nanostructure on the Performance of Organic-Inorganic Photomechanical Actuator Membranes

Xinning DONG, Tianyi GUO, Daichi KITAGAWA, Seiya KOBATAKE, P. PALFFY-MUHORAY, Christopher J. BARDEEN

Adv. Funct. Mater., Vol. 30 (2), Article No. 1902396 (9 pages) (2020)

Porous anodic aluminum oxide (AAO) membranes template the growth of photochromic crystalline nanowires. The resulting organic-inorganic composite can function as a photomechanical bending actuator. In order to investigate how the nanostructural properties of both the organic and inorganic components affect the photomechanical response, the composite mechanical properties are characterized using a variety of methods. There is a significant variation in both morphology and elastic modulus for two commercially available AAO templates with nominally identical pore diameters of 200 nm. After these templates are filled with diarylethene molecules that undergo a ring-open to ring-closed photoisomerization, the light-generated curvature and mechanical work are evaluated using two different methods. The templates with a lower average elastic modulus (16 GPa vs 68 GPa) generate almost an order of magnitude more photomechanical work. The dependence of the photomechanical response on the chemical structure of the photochrome is assessed by comparing the performance of a diarylethene that undergoes a crystal expansion to that of one that undergoes a contraction, which leads to a decrease in curvature. Both the inorganic template and the organic active component play important roles in the overall photomechanical response, with substantial room to improve

Molecular Design for a Write-by-Light/Erase-by-Heat Recording System Using Photochromic Diarylethenes with Thermal Cycloreversion

Yuta SATO, Daichi KITAGAWA, Seiya KOBATAKE

Tetrahedron, Vol. 75(35), Article No. 130487 (7 pages) (2019)

We designed and synthesized photochromic diarylethenes for a write-by-light/erase-by-heat recording system. The introduction of polar substituents at both sides of the diarylethene maintained the photocyclization and photocycloreversion reactivities, but significantly affected the thermal cycloreversion reactivity. The introduction of electron-withdrawing substituents accelerated the thermal reaction and the introduction of electron-donating substituents suppressed the thermal reaction. The rate constants of the thermal reaction were well correlated with Brown-Okamoto's substituent constant σ^+ that is a modified value of Hammett's substituent constant σ . The large rate constants are ascribed to the lower activation energy for the thermal reaction. These results provide new knowledge for the molecular design of diarylethenes for a write-by-light/erase-by-heat recording system.

Photoluminescence ON/OFF Switching of CdSe/ZnS Core/Shell Quantum Dots Coated with Diarylethene Ligands

Yuya SETO, Rie YAMADA, Daichi KITAGAWA, DaeGwi KIM, Seiya KOBATAKE

Chem. Lett., Vol. 48(11), pp. 1394-1397 (2019)

CdSe/ZnS core-shell quantum dots coated with diarylethene ligands were successfully synthesized, and the photoluminescence ON/OFF switching behavior of the quantum dots accompanying with the photochromic reactions of the diarylethene was investigated. The quantum dots exhibited a fast speed of photoluminescence ON/OFF switching even in the low photocyclization conversion ratio of the diarylethene.

Photochromism

Seiya KOBATAKE

Frontiers in Photochemistry – Fundamentals of Organic Photochemistry for Future Materials, Kagakudojin, pp. 271-284 (2018) (in Japanese)

Photochromic compounds are classified into two types, T- and P-types. Among T-type photochromic compounds, when the colored isomers are thermally stable and react to the colorless isomers by visible light, such a phenomenon is called negative photochromism. The photochromic behavior of T- and P-type photochromic compounds and negative photochromic compounds was described in this book.

Organic Crystals Transforming into Various Shapes Depending on Photoirradiation Direction

Seiya KOBATAKE

Optical (Kogaku), Vol. 48(2), pp. 53-58 (2019) (in Japanese)

Photochromic compounds undergo a photochemically reversible transformation reaction between two isomers. Such molecules in organic crystals may be potentially useful for optoelectronic devices. To apply photochromic diarylethene crystals, the materials are required to change large physical property by photoirradiation. The photoinduced crystal shape changes of diarylethene microcrystals have been so far reported. In the photoinduced crystal shape changes, there are contraction/expansion, bending, twisting, and so on, which depend on the molecular structure and the size of the crystal. This paper has focused on the photoinduced crystal shape changes of diarylethene crystals depending on the crystal size, irradiation power, irradiation wavelength, and the direction of the incident light.

Actuator Functions of Diarylethene Molecular Crystals, Chapter 5

Seiya KOBATAKE

Novel Approaches to Photofunctional Molecular and Polymeric Materials, CMC, pp. 50-60 (2019) (in Japanese)

Photomechanical behavior of molecular crystals consisting of photochromic diarylethenes was described in this book.

30 Years Passing

Seiya KOBATAKE

Newsletter, The Technical Association of Photopolymers, Japan, Vol. 87, pp. 1-2 (2019) (in Japanese)

The development from micromachines to molecular machines and photochromic molecular crystal actuators were described as a preface in this newsletter.

Functionalization and Creation of Photofunctional Photochromic Materials

Seiya KOBATAKE

Chemical Engineering (Kagaku kogaku), Vol. 83(11), pp. 699-702 (2019) (in Japanese)

Function of photochromic diarylethene derivatives, such as multicolor photochromism, light-starting thermosensors, and photoactuators, was introduced.

Simultaneous Control of Crystal Habit and Particle Size of Ecabet Sodium Hydrate with Rapid Cooling Crystallization and Temperature Cycling

Muneki KISHIDA, Koichi IGARASHI, Masayuki AZUMA and Hiroshi OOSHIMA

Journal of Chemical Engineering of Japan, Vol.52, pp.455-464(2019)

A practical strategy for the simultaneous control of particle size and shape of active pharmaceutical ingredients has been investigated using ecabet sodium (Na-ECA) hydrate, which tends to generate large plate-like crystals, as a model compound. In conventional batch-cooling crystallization, particle size and relative thickness decreased with increasing cooling rates. However, the particle size was still too large following fast cooling at a rate of 40°C/h. In rapid cooling crystallization with water, achieved by mixing hot Na-ECA solution with cold water, the particle size and relative thickness became 1/3.8 and 1/3, respectively, compared to that under batch-cooling crystallization at a rate of 40°C/h. It was also revealed that both the particle size and relative thickness increased with temperature cycling; however, the morphology of the obtained particles was still plate-like. In rapid cooling crystallization in aqueous NaCl, the particle size was reduced further to 1/4.7, and the relative thickness of the particle increased sixfold over that obtained in water. Moreover, the shape of the particle evolved effectively by temperature cycling. Consequently, granular and smaller particles could be obtained successfully. The mechanism of shape evolution was also discussed with respect to contact angles. Based on the qualitative analysis results obtained using Young's equation, we propose that shape evolution is induced by surface free energy, which drives the progression towards equilibrium shape during repeated partial dissolution and crystal growth.

GLUT1-Mediated Endocytosis Could Be a Major Pathway for Internalization of Kojic Acid-Appended Carborane Conjugate into Melanoma Cells

Satoshi DOWAKI, Koki MATSUURA, Riku KAWASAKI, Mitsunori KIRIHATA, Yoshihide HATTORI, Yoshinori SAKURAI, and Takeshi NAGASAKI

KURNS Progress Report 2018 pp. 85 (2019).

It is well known that the expression level of glucose transporter and uptake of glucose are increased in cancer cells. We have previously reported the inclusion complex of kojic acid-appended carborane (CKA) with hydroxypropyl- β -cyclodextrin (HP- β -CD) as a novel boron agent is potent for melanoma targeting BNCT. CKA/HP- β -CD complex showed melanoma cells selectivity, unique nuclear localization, and high tumor-suppression effect on BNCT toward melanoma-bearing mice. Herein, mechanism of highly efficient internalization of CKA/HP- β -CD complex into melanoma cells is evaluated. Clear suppression of CKA uptake by melanoma cells were observed in the presence of WZB117 inhibitor and siRNA for GLUT1. Furthermore, CKA uptake obviously reduced when melanoma cells were incubated in the normal medium with glucose. These results suggested that the internalization of CKA/HP- β -CD complex into melanoma cells is enhanced with GLUT1-mediated endocytosis.

Chitin degradation enzyme-responsive system for controlled release of fibroblast growth factor-2

Akira TACHIBANA, Daisuke YASUMA, Ryo TAKAHASHI, Toshizumi TANABE

Journal of Bioscience and Bioengineering, in press (2019)

Chitin is widely found in fungal cell walls and arthropod exoskeletons, and is used as a biomedical material. However, chitin is not water-soluble, restricting its use for controlled release materials. We found that water-soluble chitosan can be acetylated to produce a chitin equivalent, or chitin gel. Chitin gel, produced by mixing chitosan solution with acetic anhydride, can be degraded by lysozyme and fetal bovine serum, so could provide an ideal means for controlled release in biological systems. We tested a combination of chitin gel with a chitin binding domain (CBD) fusion protein as a controlled release system regulated by chitin degradation. A fusion protein consisting of fibroblast growth factor 2 (FGF-2) fused to CBD bound the chitin gel, and was released time-dependently rather than as an initial burst during lysozyme degradation, suggesting that this system could provide a means for controlled drug release in biological systems. Contrastingly, the trinitrophenyl residue (TNP-X) covalently bound to chitin gel, and was released by lysozyme degradation with an initial burst. If release of CBD-FGF-2 were simply dependent on lysozyme degradation of the chitin gel, the release behavior of CBD-FGF-2 would be similar to that of TNP-X, with an initial burst. Therefore, we propose that CBD-FGF-2 repeats the cycle of binding, release, and re-binding to the chitin gel during degradation. This system allows for a time-dependent, controlled release of CBD-FGF-2 without an initial burst.

Promoted performance of microbial fuel cells using *Escherichia coli* cells with multiple-knockout of central metabolism genes

Yoshihiro OJIMA, Taichi KAWAGUCHI, Saki FUKUI, Ryota KIKUCHI, Kazuma TERAOKA, Daisuke KOMA, Takashi OHMOTO, Masayuki AZUMA

Bioproc. Biosyst. Eng., in press

The effect of central metabolic activity of *Escherichia coli* cells acting as biocatalysts on the performance of microbial fuel cells (MFCs) was studied with glucose used as the energy source. Milliliter-scale two-chambered MFCs were used with 2-hydroxy-1,4-naphthoquinone (HNQ) as an electron mediator. Among the single-gene deletions examined, *frdA*, *pdhR*, *ldhA*, and *adhE* increased the average power output of the constructed MFC. Next, multiple-gene knockout mutants were constructed using P1 transduction. The $\Delta 5$ ($\Delta frdA \Delta pdhR \Delta ldhA \Delta adhE \Delta pta$) strain showed the highest ave. power output (1.82 mW) and coulombic efficiency (21.3%). Our results show that the combination of multiple-gene knockout in *E. coli* cells leads to the development of an excellent catalyst for MFCs. Finally, preventing a decrease in the pH of the anodic solution was a key factor for improving the power output of the $\Delta 5$ strain, and a maximum ave. power output of 2.21 mW was achieved with 5% NaHCO₃ in the buffer. The ave. power density of the constructed MFC was 0.27 mW/cm³, which is comparable to an enzymatic fuel cell of a Milliliter-scale using glucose dehydrogenase.

Knockout of *pgdS* and *ggt* gene changes poly- γ -glutamic acid production in *Bacillus licheniformis* RK14-46

Yoshihiro OJIMA, Joji KOBAYASHI, Takeru DOI, Masayuki AZUMA

J. Biotechnol., Vol. 304, pp. 57-62 (2019)

Poly-gamma-glutamic acid (γ -PGA) is a water-soluble, nontoxic biocompatible polymer, which is extensively used in medicines, foodstuffs, cosmetics, and in water treatment. We previously isolated a novel γ -PGA producing strain *Bacillus licheniformis* RK14 from soil and developed a hyper-producing mutant strain RK14-46 by an ethyl methanesulfonate (EMS) treatment. In this study, endo-type (*pgdS*) and exo-type γ -PGA hydrolases (*ggt*) were disrupted by integrating plasmids into the genomic DNA of *B. licheniformis* RK14-46 strain. Unexpectedly, we observed strong inhibition of γ -PGA production following deletion of the *pgdS* gene, suggesting that *pgdS* is essential for γ -PGA biosynthesis in strain RK14-46, and in its parent strain RK14. In contrast, γ -PGA production increased by the deletion of the *ggt* gene and reached 39 g/L in the presence of 90 g/L glucose and elevated oxygen supply. Furthermore, γ -PGA from the *ggt*-disrupted mutant (Δ *ggt*) maintained a larger molecular mass throughout the culture period, whereas that from the original RK14-46 strain had degraded after glucose consumption. γ -PGA-containing culture supernatants from Δ *ggt* strain showed greater flocculation efficiency in sewage sludge than supernatants from the RK14-46 strain, reflecting greater production of γ -PGA with larger molecular mass by the Δ *ggt* strain. This is the first report concerning the deletion of *pgdS* and *ggt* genes in *B. licheniformis* strain and the properties of γ -PGA obtained from the mutant strain.

Recovering metals from aqueous solutions by biosorption onto phosphorylated dry baker's yeast

Yoshihiro OJIMA, Shogo KOSAKO, Maya KIHARA, Norikazu MIYOSHI, Koichi IGARASHI, Masayuki AZUMA,

Sci. Rep., 9:225 (2019)

Biosorption is a cost-effective and simple technique for removing heavy metals and rare earth elements from aqueous solution. Here, metals were recovered from aqueous solutions using phosphorylated dry baker's yeast cells. The cells were phosphorylated using cyclo-triphosphate, $\text{Na}_3\text{P}_3\text{O}_9$. The total P content of the phosphorylated cells was ~ 1.0 mmol/g dry cell weight (DCW). The zeta potential of the phosphorylated cells was -45 mV, two times higher than for the non-phosphorylated cells. The strong negative charges of the phosphorylated cells allowed the cells to adsorb heavy metal ions such as Cd^{2+} , Cu^{2+} , Pb^{2+} , and Zn^{2+} , the adsorption capacities of which reached ~ 1.0 mmol/g DCW. This adsorption capacity was the highest level found in the previous studies using yeast dead biomass. The adsorbed metal ions were easily desorbed in 0.1 M HCl. The phosphorylated cells also adsorbed rare earth ions including Ce^{3+} , Dy^{3+} , Gd^{3+} , La^{3+} , Nd^{3+} , Y^{3+} , and Yb^{3+} with high efficiency. Furthermore, the phosphorylated yeast cells selectively adsorbed the rare earth ions (Nd^{3+} and Yb^{3+}) from a solution containing heavy metals and rare earth ions because trivalent positively charged ions were adsorbed preferentially over divalent ions. Thus, phosphorylated yeast cells therefore have great potential for use as novel bioadsorbents. It is also expected that this technique can be applied to many microbial materials as well as yeast.

Inducing flocculation of non-floc-forming *Escherichia coli* cells (Review)

Yoshihiro OJIMA, Masayuki AZUMA, Masahito TAYA,

World J. Microbiol. Biotechnol., 34:185 (2018)

The present article reviews several approaches for inducing flocculation of *Escherichia coli* cells. The common industrially used bacterium *E. coli* does not naturally have floc-forming ability. However, there are several approaches to induce flocculation of *E. coli* cells. One is induction by flocculants— polyvalent inorganic salts, synthetic polymeric flocculants, or bio-based polymeric materials, including polysaccharide derivatives. Another method is the induction of spontaneous flocculation by changing the phenotypes of *E. coli* cells; several studies have shown that physical treatment or gene modification can endow *E. coli* cells with floc-forming ability. Coculturing *E. coli* with other microbes is another approach to induce *E. coli* flocculation. These approaches have particular advantages and disadvantages, and remain open to clarification of the flocculation mechanisms and improvement of the induction processes.

Crumbs3 is a critical factor that regulates invasion and metastasis of colon adenocarcinoma via the specific interaction with FGFR1.

Hidekazu IIOKA, Ken SAITO, Masakiyo SAKAGUCHI, Taro TACHIBANA, Keiichi HOMMA, Eisaku KONDO.

Int. J. Cancer 145(10):2740-2753. (2019)

Epithelial cell polarity regulator Crumbs3 (*Crb3*), a mammalian homolog within the *Drosophila* *Crb* gene family, was initially identified as an essential embryonic development factor. It is recently implicated in

tumor suppression, though its specific functions are controversial. We here demonstrate that Crb3 strongly promotes tumor invasion and metastasis of human colon adenocarcinoma cells. Crb3 centrality to tumor migration was supported by strong expression at invasive front and metastatic foci of colonic adenocarcinoma of the patient tissues. Accordingly, two different Crb3-knockout (KO) lines, Crb3-KO (Crb3 $-/-$) DLD-1 and Crb3-KO WiDr from human colonic adenocarcinomas, were generated by the CRISPR-Cas9 system. Crb3-KO DLD-1 cells exhibited loss of cellular mobility in vitro and dramatic suppression of liver metastases in vivo in contrast to the wild type of DLD-1. Unlike DLD-1, Crb3-KO WiDr mobility and metastasis were unaffected, which were similar to wild-type WiDr. Proteome analysis of Crb3-coimmunoprecipitated proteins identified different respective fibroblast growth factor receptor (FGFR) isoforms specifically bound to Crb3 isoform a through their intracellular domain. In DLD-1, Crb3 showed membranous localization of FGFR1 leading to its functional activation, whereas Crb3 bound to cytoplasmic FGFR4 in WiDr without FGFR1 expression, leading to cellular growth. Correlative expression between Crb3 and FGFR1 was consistently detected in primary and metastatic colorectal cancer patient tissues. Taking these together, Crb3 critically accelerates cell migration, namely invasion and metastasis of human colon cancers, through specific interaction to FGFR1 on colon cancer cells.

GPAT2 is required for piRNA biogenesis, transposon silencing, and maintenance of spermatogonia in mice.

Yusuke SHIROMOTO, Satomi KURAMOCHI-MIYAGAWA, Ipppei NAGAMORI, Shinichiro CHUMA, Tatsuhiko ARAKAWA, Toru NISHIMURA, Hidetoshi HASUWA, Taro TACHIBANA, Masahito IKAWA, Toru NAKANO.

Biol. Reprod. 101(1):248-256. (2019)

PIWI-interacting RNAs (piRNAs), a subclass of germ cell-specific noncoding small RNAs, are essential for de novo DNA methylation of retrotransposon genes in embryonic testes. PIWIL2/MILI, one of three mouse PIWI family members, is indispensable for piRNA production, DNA methylation of retrotransposons presumably via piRNA, and normal spermatogenesis. In vitro analysis using germline stem cells (GS cells) revealed that glycerol-3-phosphate acyltransferase 2 (GPAT2), which is a mitochondrial outer membrane protein involved in generation of lysophosphatidic acid (LPA) and highly expressed in testes, plays important roles in spermatogenesis. Namely, GPAT2 binds to PIWIL2 and is closely involved in the biogenesis of piRNAs; this process is independent of its enzymatic activity on LPA. However, GS cells recapitulate only a limited phase of spermatogenesis and the biological functions of GPAT2 remain largely unknown. In this study, we generated GPAT2-deficient mice and conducted comprehensive analyses. The deficient mice showed defective piRNA production and subsequent de-silencing of IAP and Line-1 retrotransposons in fetal testes. In addition, apoptosis of pachytene spermatocytes was observed. These abnormalities were all common to the phenotype of PIWIL2-deficient mice, in which piRNA production was impaired. GPAT2-deficient mice exhibited apoptosis in spermatogonia at the neonatal stage, which was not observed in PIWIL2-deficient mice. These data show that GPAT2 plays a critical role in preventing apoptosis in spermatogonia.

Architecture and Building Engineering

Load-Carrying Capacity of Semi-Rigid Double-Layer Grid Structures with Initial Crookedness of Member

Huijun LI and Yoshiya TANIGUCHI

Engineering Structures 184 (2019) 421-433

The main aim of the present study is to investigate the effect of joint bending stiffness and initial crookedness of member on load-carrying capacity of double-layer grid with different member slenderness ratios. Firstly, a mechanical model of semi-rigidly jointed double-layer grid with initial crookedness of member is developed, followed by verification of two simple grid structures. Then, the influence of joint bending stiffness and random initial crookedness of member on load-carrying capacity of double-layer grid is systematically investigated. Finally, failure mechanism and destructive process of the double-layer grid are discussed. The results indicate that the load-carrying capacity of double-layer grid with initial crookedness of member is remarkably affected by joint bending stiffness, especially for double-layer grid with slender member. The limit load of double-layer grid markedly decreases when κ less than 1.5–2. The effect of initial crookedness of member on load-carrying capacity of double-layer grid has a close relationship with member slenderness ratio. With the increase of member slenderness ratio, the limit load reduction gradually increases. The distribution of random initial crookedness of member distinctly affects the limit load of double-layer grid, and some of them can observably reduce the limit load, especially for double-layer grid with large member slenderness ratio. The failure mode of imperfect double layer grid is affected by distribution of initial crookedness of member and joint bending stiffness. The existence of random initial crookedness of member can aggravate P- Δ effect, and some compression members of double layer grid lose their stability prematurely, which further leads to the instability of whole double-layer grid.

Load Carrying Capacity of Three-Way Single-Layer Reticulated Dome with Initial Member Crookedness of Prescribed Probabilistic Amplitude

Huijun LI and Yoshiya TANIGUCHI

Journal of the International Association for Shell and Spatial Structures, Vol.60(2019), No.2, pp.133-144

Single-layer reticulated dome is a typical imperfection-sensitive structure. Initial crookedness of member as a typical imperfection innately exists in reticulated dome. The approach to establish reticulated dome with crooked member is firstly presented, followed by the study of its effect on load-carrying capacity of single-layer three-way reticulated dome. The main conclusions are summarized as follows: load-carrying capacity of the reticulated dome is influenced by initial member crookedness. Compared with the perfect dome, mean of limit load reductions of imperfect ones is 9.35%. The limit load reduction of the imperfect dome is closely related to the distributions of crooked member, and some of them can evidently reduce the limit load. Limit load of the dome obeys extreme I type distribution. Instability modes of imperfect domes considered here belong to nodal instability triggered by member buckling, and there is a dimple in each imperfect dome. The position of dimple is not unique, and it appears in different locations depending on the shape of the imperfect dome. Moreover, the member buckling and the overall buckling of imperfect domes happen simultaneously, i.e. the synchronous instability.

Prediction Method of Bearable PGA for Single Layer Lattice Domes under Vertical Loading

Yoshiya TANIGUCHI, Tomoya MATSUI, Susumu YOSHINAKA

Proceedings of the 12th Asian Pacific Conference on Shell & Spatial Structures, APCS2018, 458-467

This paper focuses on the elasto - plastic behavior of static and dynamic responses for single layer lattice domes, which are subjected to vertical loads. The purpose is to make clear the relationship between seismic responses and static responses from the view point of input strain energy properties after and before yielding, and to estimate bearable seismic levels with the information of static elasto – plastic behaviors. The static response compared is the relationships between equivalent velocities of strain energies and displacements. The dynamic response compared is that between earthquake input acceleration PGA and equivalent velocities of strain energies.

Evaluation of XIMIS for assessing extreme pressure coefficients

Eri GAVANSKI, Nicolas J. Cook (Independent researcher in UK)

Front. Built Environ. 5:48. Doi: 10.3389/fbuil.2019.00048

Commonly used methods to estimate peak wind pressures on buildings are summarized. The Harris (2009) penultimate XIMIS method is described and calibrated against Gumbel epochal extreme-value analysis (EVA), as well as with the Hermite-Davenport peak factor method by Yang et al. (2013) (YGP) using a very long record of

wind tunnel data from many pressure taps. The “industry standard” EVA, comprising 16 ten-minute epochs, gives the best accuracy, but is inefficient in its use of data. YGP is the least accurate, with the largest anomalies underestimating in reattachment zones. XIMIS is comparable to EVA for the same record lengths and remains better than YGP for records up to six times shorter.

Examination on characteristics of negative peak wind pressures acting on multi-span saw-tooth and gable roofs for cladding and components design

Eri GAVANSKI, Takuya UMEGUCHI (Osaka City University), Hiroaki NISHIMURA (Association for Disaster Prevention Research)

National Symposium on Wind Engineering, (3-5 Dec 2018, Tokyo, Japan)

The characteristics of negative peak external wind pressures acting on single and multi-span saw-tooth and gable roofs were examined by using wind tunnel test results performed on models with various roof slopes and the number of spans. Differences in roof shape and slope change the location of negative peak pressure on the roof and its magnitude. The difference in the number of spans between 1 and more than 1 span has significant effect on the distribution of negative peak wind pressure. However, the increase of the number of spans more than 2 does not change the wind pressure distribution. Comparisons with the specified values in ASCE7 in the United States were also performed.

Thermal environment ranges providing good sleep quality in bedrooms during summer -Analysis of university students in Osaka

Noriko Umemiya, Hirona Bessho, Tomohiro Kobayashi, Yoshiki Tachibana and Yusuke Nakayama

Proceedings of the 10th Windsor Conference, Windsor, UK, 1210-1217, (2018).

A questionnaire survey and bedroom thermal environment measurements were conducted for 24 university students for 581 nights in the peak of summer for three years to clarify subjective ranges of thermal comfort and good sleep quality. Results revealed the following. 1) Thermal comfort decreased as the standard effective temperature (SET*) increased when SET* was more than 21°C. 2) The SET* range at which more than 80% voted in three central categories of seven-point thermal sensation scale was 19.3–22.7°C, ‘thermally acceptable’ temperatures were 17.7–28.0°C. The good side of the sound sleep evaluation scale was 20.1–23.7°C. 3) Subjective sleep quality decreased gradually when SET* exceeded 22°C. However, sleep quality related to Drowsiness and Fatigue recovery increased when SET* exceeded 26°C. 5) The ratio of ‘thermal comfort’ for air conditioner (AC) non-use nights peaked when SET* was 20°C, although it peaked at 25°C for AC use nights. 6) Subjective sleep quality decreased as SET* increased for AC non-use nights, although it peaked at 25°C for AC use nights.

Simplified estimation on wind-induced natural ventilation rate caused by turbulence for a room with minute wind pressure difference

Tomohiro Kobayashi, Mats Sandberg, Takuya Fujita and Noriko Umemiya

Proceedings of Roomvent 2018, Espoo, Finland, (2018).

The goal of this study is to propose a new prediction method of the wind-induced natural ventilation rate that works well for minute wind pressure difference. In this study, a rectangular single room model provided with two openings is studied by Large Eddy Simulation (LES). First, the flow rate is measured by tracer gas method in a wind tunnel, and it is simulated by LES to verify the accuracy. Then, a parametric study is performed by varying the opening position and corresponding wind pressure coefficient difference (ΔC_p). Finally, an equation to estimate the flow rate is proposed where the standard deviation of ΔC_p and mean velocity in the vicinity of the opening are considered as a key parameter to account for the effect of the turbulence on flow rate.

General wind pressure coefficient database and its application for estimation of natural ventilation rate of mid- to high-rise office building

Yoshiko Kawawake, Tomohiro Kobayashi and Noriko Umemiya

Proceedings of Roomvent 2018, Espoo, Finland, (2018).

The final purpose of this study is to propose a simple estimation method of natural ventilation (hereinafter referred to as NV) rate for mid- to high-rise office buildings. In this study, flow rate of the existing NV building is evaluated by two types of wind pressure coefficient (C_p value), i.e., database values and experimental values obtained from wind tunnel test with its scaled model. In the previous study, the database was organized by wind tunnel test with the simplified city block model, which was aimed to obtain C_p values for various business districts with ease. Comparing the flow rate calculated by database C_p values and that by the C_p values from the wind tunnel test for actual city block, the usefulness of the database was investigated for shaft type NV system. However, in the shaft type NV system, the main driving force is buoyancy, and C_p value is not dominant. In this paper, therefore, the

validity of the database is studied also for other types of NV system utilizing wind. Namely, three different ventilation types, cross-vent type, shaft type, and combined type are studied. It is finally shown that the Cp value database arranged in the previous study can work well to predict NV rate even for cross-vent type and combined type NV systems.

Relation among gazing point distribution, pupil size and illuminance for elderly people when walking

Umemiya Noriko, Shiramoto Yudai and Quiao Wei

Proceedings of the 11st Asia Lighting Conference, Kobe, Japan, 79-82, (2018).

Gazing points and pupil size of elderly people were measured when walking with face illuminance to prevent fall accidents. Relations between gazing characteristics and illuminance were analysed, clarifying the following points.

- 1) Mean pupil sizes differed among participants, but the 25–75 percentile values were similar.
- 2) Individual differences in the gradient of pupil size regression by illuminance were large. The pupil size changed little for about 35% of participants when the illuminance changed. Pupil responses against illuminance change were slight for them.
- 3) Gazing points were distributed vertically for participants, showing steep gradients, but the points were concentrated for participants showing moderate gradients.
- 4) Gazing points were distributed more evenly for participants who walked more than two hours per day.

Extending the Verbal Map Navigation System for Visually Impaired People and a Method of Virtual Walk Experiment

Hiroko MATSUMOTO, Takashi UCHIDA, Risa SAKAGUCHI

Japan Society of Traffic Engineers, Papers on Traffic Engineering, No. 38, pp. 243-248 (2018) (in Japanese)

Posterior Evaluation of the Small-Size River Development for the Nature-Friendly Environment and the Water Amenity in the Built-Up Area—Analyses Based on the Actual Use Situation

Yasumasa FUKUSHIMA and Takashi UCHIDA

Journal of Japan Society of Civil Engineers, Ser. D3, Vol.74, No.5, pp.1_117-1_128 (2018) (in Japanese)

In recent years the development of the urban river has been focusing on efforts for the environment and the water amenity besides the flood control and the water utilization, in some cases however, the residents along the river have failed to value and then water amenity has made little progress.

This paper takes a case of the waterfront development of the small size river in an emerging built-up area. Going through several years after the project implementation, we take hold of the actual condition and the attitudes of residents by means of hearing survey to the inhabitants. This study performs analyses on the results of actual condition survey towards the smooth implementation of the enterprise and the consensus formation and in urban riverside development considering development methods in order to promote the utilization with high evaluations from the inhabitants as concrete strategies.

Examination of Dialogue Scenario Evaluation Index in Development of Dialogue Robot to Increase Motivation of Going Out for Visually Impaired and Elderly People

Yuriko YOSHIKANE, Hiroko MATSUMOTO, Riho MORISAWA and Takashi UCHIDA

Japan Society of Civil Engineers, Proceedings of Infrastructure Planning, No. 58, pp.206_1-4 (2018) (in Japanese)

Micro Traffic Simulation to Examine Congestion-control Measures Using Pace Maker Lights

Takahiro IGAKI and Takashi UCHIDA

Osaka City University, Memoirs of the Faculty of Engineering, Vol. 59, pp.7-17 (2018)

One cause of congestion on highways is “sag”: a section where the road gradient changes gradually from downward to upward. Drivers unconsciously reduce speed without anticipating the uphill part of this section. That speed reduction is imitated by other drivers, creating congestion. Some attempts to use pace maker lights have been undertaken as measures against traffic congestion occurring at a sag. Some trial operations are being conducted on various highways.

For this study, a micro traffic simulation using a car-following model with pace maker lights installed. Then a simulation was conducted of traffic conditions at the sag using time–space diagrams. Results confirmed the characteristics of the car-following model. Results demonstrated that different driving behaviors among drivers affect congestion.

Possibility of Development of Educational Measures by Enacting the Ordinance for Safer Use of Bicycles in Local Governments

Yasuyuki TAKEDA, Yasuo HINO and Takashi UCHIDA

Japan Society of Civil Engineers, Proceedings of Infrastructure Planning, No. 58, pp.136_1-6 (2018) (in Japanese)

Recently the movement of enacting the ordinance for promoting safer use of bicycles has been progressing in local government, because of increasing the ration of traffic accidents concerned with bicycles. However, the effects for enacting ordinance according to each concrete contents have not been yet clear.

Then in this study, based on a series of studies in corporation with the local governments enacted the ordinance for safer use of bicycles, the effects and further required issues of educational measures by enacting ordinance were analyzed. As a result, the effects of educational measures based on the ordinance were confirmed by using some specific indicators. In addition, the possibility of progressing measures for road safety education was able to be referred, by holding these information un common among local governments.

Vital Reactions as a Measure of Stress Levels in Bicycle Riders According to Degree of Task

Katsumasa TATSUNO and Nagahiro YOSHIDA

Japan Society of Traffic Engineers, Papers on Traffic Engineering, No. 39, pp. 63-68 (2018) (in Japanese)

In this study, in order to obtain basic knowledge on the method of measuring the relationship between stress factors and reactions relating to the usage environment, stress generated in bicycle users are analyzed using a plurality of biological reaction indices in a plurality of traffic environments having different composition contents of stress factors. We embody it using individual differences as driving experience and complexity of driving tasks as a driving course so that you can explicitly consider the driving experience difference related to stress and the complexity of driving task required for bicycle use environment. And we compared differences in biological reaction by influence of individual differences such as driving experience and complexity of driving tasks. Results indicated that vital reactions while riding on the paths requiring multitasking showed an increase on all indices compared to the reactions under single-task conditions. In addition, it was found that the vital reactions in daily users tended to be larger under any driving conditions compared to the reactions of occasional users.

Empirical analysis of hazard perception and driving behaviors among high school and college students on motorcycles in Phnom Penh, Cambodia

Takuya KONISHI and Nagahiro YOSHIDA

The International Association of Traffic and Safety Sciences, IATSS Research, Volume 42, Issue 4, pp. 171-179 (2018)

In Cambodia, motorcycle use has spread rapidly in recent years, and serious accidents involving motorcycles have increased. Motorcycle accidents involving young people are particularly common, and there are various issues concerning traffic safety. To understand the situation in Phnom Penh, Cambodia, we conducted a questionnaire survey on driving attitude and behavior of motorcycle users targeted at high school and college students and a video observation survey of motorcycle driving conditions. Based on the survey analysis results, we held a traffic safety workshop (WS) comprising practical skills and classroom learning centered on hazard anticipation. In this study, we conducted a statistical comparative analysis of driving behavior frequency on non-intersection intervals of arterial roads before and after the WS, based on observational results from video cameras mounted on motorcycles. The results showed that the WS effects were associated with a reduction in average travel speeds and changes in driving behavior, such as frequency of lane changing. Different responses to the WS were observed according to attributes, and thus, the relationship between the content of this kind of traffic safety WS and behavioral changes needs to be clarified and a more advanced traffic safety WS program developed.

A Study on the effect of Motorcycle Traffic Safety Workshop using Travel Speed and Vehicle Density in Phnom Penh, Cambodia

Toshiki KOYANAGI, and Nagahiro YOSHIDA

Osaka City University, Memoirs of the Faculty of Engineering, Vol. 59, pp.19-25 (2018)

In Cambodia, motorcycle use has spread rapidly in recent years, and serious accidents involving motorcycles have increased. In particular, many young motorcyclists have been involved in traffic accidents, and various issues in traffic safety are remained. To understand the current situations related to these issues in Phnom Penh, Cambodia, a video observation survey on driving situations of motorcycle users in high school and university were conducted. Based on the results, a traffic safety workshop was held to improve their risk perception ability and basic riding skills. In this study, a statistical analysis was conducted to compare travel speed with vehicle density on arterial roads before and after the workshop. The results showed that travelling speed decreased to be effects of the traffic safety workshop, and the vehicle density could be an explanatory variable to represent various driving conditions of motorcycles including psychological effects.

Latent Opportunities for the Use of Two-Rider Bicycles and Associated Challenges by Welfare Service Providers

Takuya KONISHI, and Nagahiro YOSHIDA

Osaka City University, Memoirs of the Faculty of Engineering, Vol. 59, pp.27-30 (2018)

For persons with reduced mobility (PRM), the two-rider bicycle might be a potential, practical means of transportation, and the development of bicycles that meet these needs is in progress. While it revealed that there were many limits imposed on their use as a private use in a previous study, the opportunities for business use or associated challenges remain unclear. Thus, the purpose of this study is to understand the

latent opportunities or use of two-rider bicycles by welfare service providers, as well as the associated challenges. A hearing survey was conducted on various type of welfare service providers that operate transportation services for the elderly and people with disabilities. Furthermore, a questionnaire survey was conducted on potential users after providing opportunities to experience two-rider bicycles. The results confirmed that there were different types of latent opportunities for the use of two-rider bicycles by each type of welfare service providers.

Study on Measuring Level of Stress for Bicycle Facilities using Vital Reactions taking Task Complexity into Consideration

Katsumasa TATSUNO and Nagahiro YOSHIDA

Japan Society of Civil Engineers, Proceedings of Infrastructure Planning, No. 58, pp. 218_1-4 (2018) (in Japanese)

In this study, in order to obtain basic knowledge on the method of measuring the relationship between stress factors and reactions relating to the usage environment, stress generated in bicycle users are analyzed using a plurality of biological reaction indices in a plurality of traffic environments having different composition contents of stress factors. We embody it using individual differences as driving experience and complexity of driving tasks as a driving course so that you can explicitly consider the driving experience difference related to stress and the complexity of driving task required for bicycle use environment. And we compared differences in biological response by influence of individual differences such as driving experience and complexity of driving tasks.

Change of subjective and objective comfort for pedestrians and cyclists before and after Road space reallocation: Case study of Midosuji in osaka

Haruka KAWACHI, Takashi UCHIDA and Nagahiro YOSHIDA

Japan Society of Civil Engineers, Proceedings of Infrastructure Planning, No. 58, pp. 239_1-4 (2018) (in Japanese)

The road space reallocation project on Osaka's main street, Midosuji, started in 2017 to realize the concept of human-centered urban spaces in response to the change of social trends and conditions. The pilot project has been undertaken to increase spaces for pedestrians and cyclists. While the "Level of Service" concept was widely employed to evaluate user comfort issues in the transportation field, it is unknown whether it could apply to these space differences and evaluate the reallocation effect correctly. The objective of this study is to help proposal when we what comfort factor are. I conducted questionnaire and video survey on narrow road, wide road without rest space and wide road with rest space. The result shows possibility of effect to users' comfort by rest space and expected speed. So I analyzed the relationship between subjective comfort and traffic situation.

Analysis of Industrial Landscape Characteristics Considering Port Elements from Viewpoints on the Water in the Hanshin Industrial Region

Hayato KITAGAWA and Nagahiro YOSHIDA

Japan Society of Civil Engineers, Proceedings of the annual meeting in Kansai, 2 pages (2019) (in Japanese)

Distributed around rivers and harbors such as the Yodo River and Osaka Bay, the Hanshin Industrial Region is Japan's leading industrial area. The area developed around the steel and shipbuilding industries before the war, while after the war, many food manufacturers located here, and recent redevelopments have resulted in a variety of landscapes existing in the industrial region. The Hanshin Industrial Region has high historical value, and it is hoped that the landscape will be preserved and utilized as industrial heritage. However, the composition of elements making up the many viewpoints and landscapes in the region has not been determined. Therefore, after fixing viewpoints out at sea and organizing/classifying the landscape elements, this study conducted a fundamental analysis of the composition and locational characteristics of distinctive port landscapes.

A comparative study on saturation flow rate of mixed traffic before and after signal installation in Phnom Penh, Cambodia

Kazuto IMAI and Nagahiro YOSHIDA

Japan Society of Civil Engineers, Proceedings of Infrastructure Planning, No. 58, pp. 258_1-4 (2018) (in Japanese)

Change of Level of service on Sidewalk and Bicycle lane before and after installation the Rest Space on Road Space Reallocation at Midosuji Street in Osaka

Haruka KAWACHI, Nagahiro YOSHIDA

The 8th Japan Cycling Congress, Poster session (2018) (in Japanese)

Stress Evaluation using Vital Reaction Model for Bicycle Facilities

Katsumasa TATSUNO and Nagahiro YOSHIDA

The 8th Japan Cycling Congress, Poster session, (2018) (in Japanese)

Leaching characteristics of naturally derived toxic elements in the alluvial marine clay layer beneath Osaka Plain, Japan: implications for the reuse of excavated soils

Hiroko Ito (Geo-Research Institute), Harue Masuda (Faculty of Science), Akihiko Oshima

Environmental Earth Sciences (2019) 78:589

The contamination risks by naturally derived toxic elements must be assessed to achieve a sustainable geo-environment when utilizing excavated surplus soils. To estimate the controlling factors and risks of groundwater pollution associating with the application of recycled excavated surplus soils, the sequentially extracted fractions of major and toxic elements were analyzed and compared to the results of the simple batch leaching test. The concentrations of bulk B and Pb of the Holocene marine clay layer Ma13 were the maximum 75 ppm and 28 ppm at the middle depth and varied similar to the change of clay fraction, while the bulk As concentration was the maximum 12 ppm at the upper part of the Ma13. The B adsorbed onto the clay minerals was easily desorbed under the neutral pH condition. Arsenic was released especially from the transitional sandy silt layers at the upper and lower parts of Ma13 where contacting with oxic groundwater. The 0.45- μm filter required by Japanese regulations does not efficiently remove colloidal particles resulting in poor reproducibility of batch leaching tests, especially for Pb. Also, relative indices of metal mobility suggest that the long-term risk of groundwater contamination via the reuse of excavated surplus soils will not be accurately estimated only by the simple batch leaching test. The change of redox and pH conditions associating with relocation and preservation must be considered to fully evaluate the risk of toxic element mobilization of the excavated surplus soils.

Measures of Subsidence in Natural or Artificial Low Land without Ground Improvement III: Subsidence and Regional Ground Property

Akihiko Oshima,

Journal of the Society of Material Science Japan, Vol .68, No.5, pp. 450–455, 2019. (in Japanese)

Geotechnical problems and countermeasures in the Osaka Plain

Akihiko Oshima,

Geotechnical Engineering Magazine, Vol .67, No.9, pp. 43–50, 2019. (in Japanese)

Settlement Prediction Considering Cyclic Consolidation Behavior of Pleistocene Clay Layers by Groundwater Level Fluctuation of Confined Aquifer at Maishima, Osaka City

Koudai Takeno (Department of Urban Engineering), Akihiko Oshima, Shuhei Temma (Department of Urban Engineering), Masayoshi Nakao (Advanced Research Institute), Yauhisa Nakaso (Advanced Research Institute)

Proceedings of the Kansai Geo-Symposium 2019, No. 1-1, pp. 7–12, 2019. (in Japanese)

Site Investigation Results at Bentencho, Minato-ku in Osaka City

Akihiko Oshima, Kondo Masahiro (West Japan Railway Company), Sakamoto Hiroaki (West Japan Railway Company), Bando Masato (West Japan Railway Company), Nakai Takehiro (Kiso-Jiban Consultants) Fukai Haruo (Kiso-Jiban Consultants), Koji Kubota (Soil and Rock Engineering)

Proceedings of the Kansai Geo-Symposium 2019, No. 2-1, pp. 50–55, 2019. (in Japanese)

Comparison of evaluation liquefaction risk in Bentencho area, Minato-ku, Osaka

Atsushi Sagawa (Chuo Fukken Consultants), Akihiko Oshima, Hiroyuki Goto (Kyoto University), Kenichi Sueyoshi (Nippon Koei), Kai Seiji (Diaconsultants), Ken Kageyama (Kiso-Jiban Consultants), Mari Kasugai (Geo-Research Institute), Hisanori Nagai (Konoike Construction), Masato Bando (West Japan Railway Company), Haruo Fukai (Kiso-Jiban Consultants)

Proceedings of the Kansai Geo-Symposium 2019, No. 2-2, pp. 56–59, 2019. (in Japanese)

Prediction of site amplification and liquefaction potential on subsurface ground in Osaka area based on equivalent linear seismic response analysis

Kenichi Sueyoshi (Nippon Koei), Akihiko Oshima, Masataka Nakamura (All Nippon Engineering Consultants), Teruyuki Hamada (Geo-Research Institute), Mari Kasugai (Geo-Research Institute), Toshiyuki Hirai (Newjec)

Proceedings of the Kansai Geo-Symposium 2019, No. 2-3, pp. 60–65, 2019. (in Japanese)

Micro-tremor characteristics of large scale embankments in northern Wakayama city and construction age

Yasuyuki Nabeshima (Akashi College), Akihiko Oshima, Katsuyuki Kawai (Kinki University), Nobuyuki Endo (Newjec), Kenjiro Fukutsuka (Earthtech Toyo), Kohei Toyofuku (Pacific Consultants)

Proceedings of the Kansai Geo-Symposium 2019, No. 2-4, pp. 66–71, 2019. (in Japanese)

Long-term variation of groundwater level and ground settlement in Osaka area

Toru Inaba (Penta-Ocean Construction), Junichi Nagaya (Geo-Research Institute), Mari Kasugai (Geo-Research Institute), Akihiko Oshima, Eiichi Isono (Morikawasakusen), Naoko Kitada (Geo-Research Institute), Hironori Tanimoto (Kawasaki Geological Engineering)

Proceedings of the Kansai Geo-Symposium 2019, No.5-3, pp. 187–192, 2019. (in Japanese)

Example Collection of Liquefaction Countermeasure at City Area

Yuutatsu Nomaki (Oyo Corporation), Mari Kasugai (Geo-Research Institute), Akihiko Oshima, Seiji Suwa (Geo Office Suwa), Shigeyoshi Hirata (Daiwa House Industry), Akira Fukai (Sekisui House), Masashi Yoshikawa (Kinjo Rubber)

Proceedings of the Kansai Geo-Symposium 2019, No. 5-4, pp. 193–196, 2019. (in Japanese)

Experimental relation between shear strength under low pressure and S-wave velocity of rock subjected to mechanical weathering

Mohsin Usman Qureshi (Sohar University), Ikuo Towhata (The University of Tokyo), and Suguru Yamada
Soils and Foundations, In Press, Corrected Proof, Available online 27 September 2019.

The reduction in the shear strength of rock exposed on slope surfaces due to mechanical weathering is a ubiquitous phenomenon in regions where extreme environmental conditions prevail, i.e., repeated changes in temperature and moisture. In dealing with the slope instability problems in such regions, the long-term effects of weathering on the strength, deformation and durability characteristics of exposed rock are envisaged in this study. Therefore, in addition to conducting multiple-cycle standard slake durability tests on rock samples taken from the lithologies of Pakistan and Japan, and on artificial soft rock, the decrease in strength and stiffness is also studied by reproducing mechanical weathering in the laboratory. The reproduced laboratory weathering (RLW) is conducted with a new device that enables vacuumed saturation, freezing, thawing, drying and cooling under a maintained level of confining pressure. The decrease in strength, stiffness and durability is elucidated from the test results, which indicate that rock having a very low level of reference strain (shear strength/modulus at small strain) is resistant to RLW and slaking. Intact rock exhibits very low reference strain and this reference strain increases with an increase in the degree of weathering, which is the case of weathered rock. The decrease in the strength of rock is an important property for judging the safety of rock slopes undergoing weathering. Thus, the relation between the strength and the S-wave velocity of rock undergoing weathering is established. The authors recommend the use of this relation for a quick assessment of the strength of rock by briefly measuring the S-wave velocity of the weathered surface layer. The relationship will assist practitioners in quickly screening potentially unstable slopes.

Basic Study on the Characteristics of Microscopic Flow nearby Porous Media in Wave Field

Sota NAKAJO, Izumi KODUKA, Gozo TSUJIMOTO, Takaaki SHIGEMATSU

Journal of Japan Society of Civil Engineers, Ser. B2 (Coastal Engineering), Vol. 74, No. 2, I_991-I_996 (2018) (in Japanese).

The vertical two-dimensional microscopic flow nearby porous media in relatively long wave condition was measured by using Particle Image Velocimetry technique and refractive index matching method. The result on frequency analysis for time series of velocity in porous media shows considerable attenuation of wave

energy. The turbulent velocity component was defined by decomposition based on the moving average concept. The simplified assessment of the development process of turbulent velocity component was conducted by volume average value of velocity and turbulent properties. The results revealed some specific development processes although there are some similarities between the wave driven flow and the oscillatory flow field. In the case of this basic study, the turbulent velocity components in the vicinity of the bottom of wave flume were more predominant than that of water surface area. However, these results based on very limited condition, therefore we need more investigation based on various situations.

A Study on the Effect of Slit Specifications on Local Scouring Properties of the Pile-Supported Wave Absorbing Breakwater

Takashi YAMANO, Daiki SAKAI, Takaaki SHIGEMATSU, Ryuichi FUJIWARA

Journal of Japan Society of Civil Engineers, Ser. B2 (Coastal Engineering), Vol. 74, No. 2, I_835-I_840 (2018) (in Japanese).

About pile-supported wave absorbing breakwater having a horizontal slit, we confirmed that wave dissipation performance did not have the difference so far even if slit shapes were different. However, we have not been able to inspect it about the influence that slit specifications (shape, opening rate, position) give to local scouring properties enough. In this study, we confirmed that scouring in case of the horizontal slit structure grew big in comparison with vertical slit structure in breaking wave by a model experiment and guessed that the cause depended on synergy of the vortex of the perpendicular to have a horizontal axis in the retarding chamber and the vortex on the structure by numerical computation. In addition, in vertical slit structure, a slit opening rate greatly influences maximum scouring right under the pile, and a slit position influences the scouring of the lower slit wall.

A Study on the Scour Characteristics of Lower Vertical Plate in Wave Field

Yusuke NAKAHARA, Takaaki SHIGEMATSU

Journal of Japan Society of Civil Engineers, Ser. B2 (Coastal Engineering), Vol. 74, No. 2, I_829-I_834 (2018) (in Japanese).

Since local scouring occurring at the foot of a flow-sediment control structure impairs the stability of the structure itself, it is required to take some measures by predicting the scale of the scouring. In this study, the hydraulic experiment was carried out to investigate the effect of the vertical plate on the scouring characteristics by observing the flow and sand migration phenomena in the vicinity of the vertical plate on the flat sand bed in detail. Based on the experimental result, the mechanism of local scouring was intellectualized and factors affect the characteristics of the local scouring were considered.

Quantification of Ecosystem Services at Tidal Flats in Osaka Bay Using Tidal Flat Health Index: Characterization of the Tidal Flats by Comparison Between Tokyo Bay and Osaka Bay

Tomonari OKADA, Yugo MITO, Takanori SUGANO, Toshiyuki TAKAHASHI, Yoshihiro AKIYAMA, Hiroshi KUROIWA, Toru ENDO, Sosuke OTANI, Susumu YAMOUCHI, Yasunori KOZUKI, Takayuki KUSAKABE, Koji OTSUKA, Ryoichi YAMANAKA, Takaaki SHIGEMATSU, Kazuyuki NAKANO, Makoto USHIRO, Tomohiro KUWAE

Journal of Japan Society of Civil Engineers, Ser. B2 (Coastal Engineering), Vol. 74, No. 2, I_1417-I_1422 (2018) (in Japanese).

In this study, the tidal flat health index (THI) was applied to four tidal flats in Osaka Bay to confirm the versatility of THI and understand the features in each tidal flat by comparing them with four tidal flats in Tokyo Bay. The reference values (the best score of each health index) in the services, such as food supply and water purification, related to the ecosystem states, in Osaka Bay were almost equal to those of Tokyo Bay. The reference values in the services, such as tourism and recreation, influenced by the regional population, were higher in Tokyo Bay than in Osaka Bay. However, the reference value of education was higher in Osaka Bay compared to Tokyo Bay, suggesting that environmental learning is active in Osaka. Principal component analysis of the nine services in the eight tidal flats in Osaka Bay and Tokyo Bay revealed that 74% of the THI scores could be explained by 2 components: "utilization of people" and "biodiversity".

Turbulent Flow Induced by Oscillating Circular Cylinder Arrays

Takaaki SHIGEMATSU and Hiroshi Matsumoto

Proceedings of 36th Conference on Coastal Engineering, Vol. 38, <https://journals.tdl.org/icce/index.php/icce/>

[article/view/8380/7188](#).

Vegetation association plays important role in the shallower coastal zone for sediment control and the nutrient and carbon absorption. It is necessary to understand the fluid motion including turbulence in the vegetation so that we may evaluate precisely shallow water region including vegetation and wet land. As the first step of research on fluid motion in the vegetation, circular cylinders are sometimes used. Many researches on the fluid force acting on the circular cylinder and fluid motion around the cylinder have been achieved so far. However, the properties of turbulent flow induced around circular cylinders in a wave, especially turbulence transition mechanism and spatial-temporal distribution of turbulence, are not almost investigated. The purpose of this study is to understand the fluid flow including turbulent induced by wave transmitting vegetation association. In this study fluid motion was measured by oscillating circular cylinder arrays in a tank by using the PTV technique.

Practical Formula for Effective Height of Impermeable Hanging Curtain in Steady Water Flow

Masahide TAKEDA, Takaaki SHIGEMATSU, Yoshinosuke KURAHARA, Chisato HARA and Yamato NISHIYAMA

Journal of Japan Society of Civil Engineers, Ser. B3 (Coastal Engineering), Vol. 75, No. 2, I_409-I_414, (2019) (in Japanese).

This study aims to propose a new prediction formula of the effective height of a hanging curtain in steady water flow. According to the hydraulic experiments and numerical calculations, the more practical calculation formula of the effective curtain height was obtained using the ratio of dynamic pressure and weight and the ratio of the effective curtain height to the curtain length. Our formula is characterized in that the experimental coefficient is without user specification, and the weight is included in the formula, and the parameter using the ratio of the initial curtain height to the water depth is used.

Estimation of Characteristics of Micro-Barometric Wave and Its Effect on Longwave Propagation

Sota NAKAJO, Sooyoul KIM

Journal of Japan Society of Civil Engineers, Ser. B3 (Ocean Engineering), Vol. 74, No. 2, I_539-544, (2018) (in Japanese).

The characteristics of micro-barometric waves in Kyushu island estimated from analysis of high resolution stationary data was similar between each station. The propagation speed and direction was estimated based on cross-correlation analysis. Even if synoptic low-pressure development was similar, micro-barometric wave propagation process was different. Numerical simulation results show the possibility of significant meteorological tsunami caused by very small amplitude pressure waves, and importance of group wave characteristics, e.g. number of waves or wave length.

Proposal of an Empirical Equation for Storm Surges Employing a Stochastic Typhoon Model in the Sea of Aki and Iyo-Nada

Tomohiro YASUDA, Kanoto YOKOYAMA, Shota HIRAI, Sota NAKAJO, Sooyoul KIM

Journal of Japan Society of Civil Engineers, Ser. B3 (Ocean Engineering), Vol. 74, No. 2, pp. I_581-I_586, (2018) (in Japanese).

Recently, the climate has become extreme by the influence of global warming, and frequency of strong typhoon attack is getting increase. Particularly, storm surge disasters are influenced by intensified typhoons. The number of observations of storm surges are limited and insufficient because hazardous storm surges are low-frequency events. It is difficult to assess the probability of storm surges only based on observation data. This study simulates storm surges employing a stochastic typhoon model and a non-linear shallow water model, and proposes an empirical equation. Analysis assesses the effect of the number of data and the typhoon route on estimation accuracy by a proposed empirical equation targeting in Hiroshima (Aki-nada sea) and Matsuyama (Iyo-nada sea). As a result, errors and variations are reduced and the accuracy can be improved by increasing the number of data. Also, even if tropical cyclones have the same scale, storm surge are different by the difference of routes, which are dangerous semicircle and navigable semicircle. If compute the coefficient after classifying the routes, the proposed method can estimate storm surges of high accuracy at any locations.

Study for Impact of Climate Change on Typhoon and Wave in the Sea of Japan

Sooyoul KIM, Keishiro CHIYONOBU, Sota NAKAJO, Takao OTA, Tomohiro YASUDA

Journal of Japan Society of Civil Engineers, Ser. B2 (Coastal Engineering), Vol. 74, No. 2, pp. I_673-I_678,

(2018) (in Japanese).

In this study, the effect of the climate change on typhoons in the Sea of Japan and waves on the Sanin coast is examined. The global stochastic typhoon model is used to estimate typhoons in the present and future climates. The present typhoons of 5,382 in 1966 to 2008 and the future typhoons of 6,901 in 2088 to 2099 are estimated. The estimated typhoon is validated by IBTrACS with a linear interpolation method. It is found that the number of future typhoon increases in comparison to that of present typhoon. The future typhoon is averagely stronger than the present typhoon. However, the extremely strongest typhoon is revealed in the present climate. The moving speed of the future typhoon is faster than that of the present typhoon. Series of wave simulations with 10 strongest typhoons in the present and future climates showed that higher wave heights appear than designed wave heights in a port on the Sanin coast.

Sensitivity of Tropical Cyclone Track to Assessment of Severe Storm Surge Event at Tokyo Bay

Sota NAKAJO, Hideyuki FUJIKI, Sooyoul KIM, Nobuhito MORI

Coastal Engineering Proceedings, Vol. 36, No. 1, 10p, doi: 10.9753/icce.v36.papers.5, (2018)

In total 82 tropical cyclones data was used to determine scenarios of translation speed, minimum central pressure and track for risk assessment of storm surge at Tokyo Bay. The numerical simulation of waves and flows was conducted by solving non-linear long wave equations. The maximum surge height shows that the typhoon passing through along northeast directional track is dangerous for Tokyo Bay. This trend confirms the previous risk assessment was reasonable. However, it has been shown that the typhoon passing through along north directional track is also dangerous although the frequency is low. Especially, it is interesting that the typhoon passing through along northwest directional track causes distinctive resurgence and harbor oscillation.

Morphological Changes at the Mouth of the Shirakawa River after Kumamoto Earthquake

Ryota YAMAGUCHI, Gozo TSUJIMOTO, Takaomi HOKAMURA, Sota NAKAJO, Ngoc Than NGUYEN
Proceedings of the 28th International Ocean and Polar Engineering Conference, ISBN: 978-1-880653-87-6, ISOPE-I-18-155, (2018).

The river mouth delta of this study is located on the center of the eastern coast of Ariake Bay, Kumamoto, Japan. Two earthquakes scaled of 7 on the Japanese scale struck Kumamoto Prefecture on April 14 and 16, 2016, and then about the 0.4 m ground subsidence was occurred. A large amount of sediment from the Shirakawa River was discharged into the river delta due to a following-flood. The clinoform along the water-route approximately propagated 150 m in the offshore direction and the bed level increased by about 1.5m. The estimated sediment discharge was $1.1 \times 10^5 \text{m}^3/\text{yr}/\text{km}^2$ during 2014 to 2016, corresponds four times during 1978 to 1997.

Projection of Decrease in Japanese Beaches Due to Climate Change Using a Geographic Database

Nobuhito MORI, Sota NAKAJO, Syohei IWAMURA, Yoko SHIBUTANI

Coastal Engineering Journal, Vol. 60, Issue 2, pp. 239-246, <https://doi.org/10.1080/21664250.2018.1488513>, (2018)

This study models shoreline retreat due to sea level rise by using geographic data and applies the model to future projections of decreases in beach area for 806 beaches in Japan. The model uses a foreshore slope (angle) based on data from a digital elevation model, and influence of the present simplified method for estimation of the shoreline retreat is examined through comparisons with previous studies at typical locations. The proposed method gives a distance of shoreline retreat due to sea level rise similar to that predicted using the Bruun rule for minimal retreat less than 30 m, but the difference becomes substantial for more extensive decreases. The decrease in beach area is projected for different sea level rises based on four Representative Concentration Pathway (RCP) scenarios from the Fifth Assessment Report of the Intergovernmental Panel on Climate Change. The decrease in beach area becomes more severe for the RCP8.5 scenario, and the proposed method predicts that a third of current sandy beaches in Japan will disappear. The extent of the decrease depends not only on the sea-level-rise scenario but also on the SLR projection model.

An Experimental Study on the Interaction between Oscillatory Flow and Idealized Porous Bed

Takaaki SHIGEMATSU, Sota NAKAJO, Yuya OKADA

Journal of Coastal Research, Special Issue No. 85, pp. 981–985, (2018)

The microscopic structures of over and inside flow of a porous medium placed in oscillatory flow was measured by the Particle Tracking Velocimetry with the refractive index matching method in order to

investigate interaction between them. The strong shear flow was observed over the surface of the porous medium and the thickness of shear flow varied with the phase of the oscillatory flow. It was found that the thickness of non-dimensional shear flow was almost constant and that it did not depend on the Reynolds number. It was found that the thickness of non-dimensional shear flow was almost constant and it independent with the Reynolds number. Besides, it was also found that the phase difference between flows over and inside the porous bed occurred. The characteristics of the spatial variance of velocity components were shown in detail with the time phase variance. Further, the flow properties around the particle constitutes porous body were measured and investigated in detail.

Estuarine Circulation Patterns in a Complex Geometry Estuary: Dinh An Estuary, Mekong River

Ngoc Than NGUYEN, Sota NAKAJO, Toshifumi MUKUNOKI, Gozo TSUJIMOTO

Environmental Processes, Vol. 5, Issue 3, pp. 503-517, (2018)

Estuarine circulation (EC) is a natural phenomenon that contributes to the evolution of estuaries worldwide. This paper uses the Dinh An estuary, Mekong River as a case study to investigate patterns of EC in a complex cross-section estuary. An Acoustic Doppler Current Profiler (ADCP) measured a series of river discharge and current profiles at a transect near the mouth of the estuary between 15 and 30 September 2009. Tidal elevation was also recorded concurrently with the river discharge by using a leveling rod. The observed data reveal that the river-discharge phase lagged 6 h behind the tidal phase in the high-flow season (May to October). Four main types of EC were observed during the reversal time in the ebb tide with river discharges in a range of $-5000 \text{ m}^3/\text{s}$ to $13,600 \text{ m}^3/\text{s}$. There were two main flood tide patterns, which corresponded to the discharges from $-6000 \text{ m}^3/\text{s}$ to $5000 \text{ m}^3/\text{s}$. The classical EC type (seawater flows landward near the bed and river water flows seaward near the surface) appeared only in the deepest channel in the ebb tide as saline intrusion induced a density imbalance. The results suggest that tidal phase and bed geometry play important roles in forming EC patterns in estuaries. This paper provides essential information related to flow structure in complex bathymetry estuaries for further studies on saline intrusion, environmental processes, sediment dynamic and estuarine morphology.

Practical Formula for Effective Height of Impermeable Hanging Curtain in Steady Water Flow

Masahide TAKEDA, Takaaki SHIGEMATSU, Yoshinosuke KURAHARA,

Chisato HARA and Yamato NISHIYAMA

Journal of Japan Society of Civil Engineers, Ser. B3 (Coastal Engineering), Vol. 75, No. 2, 409-414(2018) (in Japanese).

This study aims to propose a new prediction formula of the effective height of a hanging curtain in steady water flow. According to the hydraulic experiments and numerical calculations, the more practical calculation formula of the effective curtain height was obtained using the ratio of dynamic pressure and weight and the ratio of the effective curtain height to the curtain length. Our formula is characterized in that the experimental coefficient is without user specification, and the weight is included in the formula, and the parameter using the ratio of the initial curtain height to the water depth is used.

Modeling a Coastal Ecosystem to Estimate Climate Change Mitigation and a Model Demonstration in Tokyo Bay

Akio SOHMA, Hisashi SHIBUKI (Mizuho Information and Research Inst.), Fumiyuki NAKAJIMA (The Univ of Tokyo), Atsushi KUBO (Shizuoka Univ.), Tomohiro KUWAE (Port and Airport Research Inst.)

Ecological Modelling, 384 pp. 261-289 (2018)

An ecosystem model called the “EMAGIN-B.C. ver 1.0 (Ecosystem Model for Aquatic Geologic Integrated Network for Blue Carbon)”, describing the Carbon-Nitrogen-Phosphorus-Oxygen-Calcium cycle was developed to estimate/predict carbon capture and storage in estuaries. EMAGIN-B.C. analyzes (1) carbon burial, wherein carbon is captured biologically in the pelagic and benthic ecosystems and stored in deeper sediments, (2) CO_2 uptake at the ocean surface while considering the carbonate chemistry with total alkalinity and Dissolved Inorganic Carbon (DIC) production/consumption due to biochemical processes, (3) DIC capture associated with grazing at the trophic level among phytoplankton, zooplankton, and benthic fauna, (4) the effects of hypoxia on benthic fauna and bacteria by precise modeling of the biochemical oxygen production/consumption and the resultant hypoxia, and (5) the carbon transport by integration with the hydrodynamic model. EMAGIN-B.C. was applied to Tokyo Bay, a eutrophic, shallow coastal area, and reproduced the observations well. From the model outputs, it can be observed that Tokyo Bay shows functions of climate change mitigation. In the one-year carbon budget, Tokyo Bay captured 16.6% of the

DIC from the atmosphere and river as organic matter by biological processes, and 3.9% of the total carbon flowing from the atmosphere and river was stored in the deeper sediment layer.

Ecosystem Model Study on Long-term Dynamics of Dissolved Oxygen and Its Factors at the Bottom Water in Tokyo Bay

Akio SOHMA and Takuro HARUTA

Journal of Japan Society of Civil Engineers, Ser. B2 (Coastal Engineering), Vol.74, No.2, pp. I_1273-I_1278, (2018) (in Japanese)

Hypoxia has been improving throughout Tokyo Bay, however, there are still seriously hypoxic areas. In this study, we analyzed the secular change of dissolved oxygen (DO) and consumption mechanism of the sea-floor due to reduction of nutrients and COD inflow from the land from 1979 to 2009, using the benthic-pelagic coupled ecosystem model, EMAGIN-H.P. As a result, the model demonstrated that there were at least three types of areas: zone A, in which DO increases; zone B, in which DO turns from a decrease to an increase; and zone C, where DO decreases. In addition, reduction of nutrients and COD inflow leads to (1) decrease of reduced substances (Mn^{2+} , Fe^{2+} , and S^{2-}) and increase of benthic fauna due to improvement of hypoxia at zone A, (2) decrease of reduced substances due to DO increase and decrease of benthic fauna due to food shortage at zone C, and (3) increase of benthic fauna until 1994 with the improvement of hypoxia and then a decrease due to food shortage at zone B. These results show that the optimal amount of nutrients and COD inflow in view of both the increase of benthic fauna and the improvement of hypoxia differs from area to area.

Annual Variation of Air-Sea CO₂ Flux at the River Mouth Area and Its Factors —Analysis of an Ecosystem Model, EMAGIN_B.C.—

Akio SOHMA, Mizuki NAKAI, Atsushi KUBO (Shizuoka Univ.), and Tomohiro KUWAE (Port and Airport Research Inst.)

Journal of Japan Society of Civil Engineers, Ser. B2 (Coastal Engineering), Vol.74, No.2, pp. I_1267-I_1272, (2018) (in Japanese)

The carbon capture and storage in the coastal shallow ecosystem is a hot topic because of its high potential. The release and uptake of atmospheric CO₂ at the air-sea boundary is an important element consisting the series of carbon capture and storage of the shallow waters. In this study, we applied an ecosystem model, EMAGIN_B.C., considering carbonate chemistry, food-web, and Carbon-Nutrients-Oxygen cycling in the benthic-pelagic coupled system to Tokyo Bay, and analyzed the dynamics of air-sea CO₂ flux and its factors especially focusing on the river mouth area. As the result of the model analysis, CO₂ was released from the ocean to air at the river mouth area on an annual average basis, although CO₂ was taken up at other areas in Tokyo Bay. In addition, the CO₂ release and CO₂ uptake are repeated in the period from the end of April to the end of November. The CO₂ absorption period is thought to be dominated by the consumption of DIC by photosynthesis, and the release period is thought to be dominated by consumption of total alkalinity by nitrification.

Estimation of Air-sea CO₂ Fluxes in Osaka Bay, Harima-hada and Ago Bay Bases on Spatial Distributions Survey of Dissolved Inorganic Carbon

Toru ENDO, Junpei SHIMANO, Kenji IKENAGA, Hideki KOKUBU

Journal of Japan Society of Civil Engineers, Ser. B2 (Coastal Engineering), Vol. 74, No. 2, I_1315-I_1320 (2018) (in Japanese).

To evaluate the air-sea CO₂ flux of Osaka Bay, Harima Nada and Ago Bay, we conducted the spatial distribution surveys of the dissolved inorganic carbon (DIC) and pH. There are low DIC concentration in the inner part of Osaka Bay where external load is large because DIC was consumed by photosynthesis of phytoplankton. On the other hand, there are high DIC concentration in the Ago Bay where much organic carbon was accumulated on the sea floor. We found that CO₂ was absorbed basically in all seas at daytime and, especially, Osaka bay had high CO₂ absorption potential compared with the other seas.

CO₂ fluxes were calculated based on a chemical equilibrium model of carbonic acid from the measurement data of DIC and pH, air to sea CO₂ flux was 12.6 to 14.0 CO₂/m²/hr in Osaka bay, 1.5 to 3.7 CO₂/m²/hr in Harima Nada and 0.8 mg CO₂/m²/hr in Ago Bay. The CO₂ Flux of Osaka Bay was larger than the averaged CO₂ fluxes of coastal seas reported in around the world.

Air-sea CO₂ Exchange and dissolved Inorganic Carbon in an Inner Part of Osaka Bay, Japan

Toru ENDO, Junpei SHIMANO, Noriko HARADA, Daiki SAKAI, Ryuichi FUJIWARA

Proceedings of the 10th International Conference on Asian and Pacific Coasts, 1073-1079. (2019)

The carbon captured by coastal oceans and ecosystems called "blue carbon" is attracting attention to reduce greenhouse gas. Recently, field surveys on air-sea CO₂ exchange have been conducted in various coastal seas to reveal the blue carbon function. In this study, we investigated the vertical distribution of the dissolved inorganic carbon (DIC) system in the inner part of Osaka Bay to reveal the air-sea CO₂ exchange characteristics in port and harbor area. Field surveys were conducted on a vertical seawall in Naruo-hama of Osaka Bay, Japan, during 12 months from November 2014 to October 2015 and during summer from August to September 2016. The vertical distributions of DIC and pH were measured on site, and the CO₂ partial pressure in water (pCO_{2w}) was calculated based on carbon acid equilibrium. Water temperature, salinity and DO were also measured to examine the relationships the vertical distribution of DIC system and water mass structure. Furthermore, the air-sea CO₂ flux (F_{CO2}) was estimated to examine the characteristics of the air-sea CO₂ exchange. DIC ranged from 787 to 2,111 μmol kg⁻¹, with seasonal and vertical change. DIC in the bottom layer increased during high water temperature period due to CO₂ production by respiration and decomposition, and DIC accumulated along with formation density stratification. The correlation between DIC and pCO_{2w} in surface layer was smaller than that in bottom layer because surface pCO_{2w} fluctuated due to inflow of river water or seawater mixing. This study area acts as CO₂ sinks under calm conditions (F_{CO2} = -3.4 mmol-C m⁻² d⁻¹), however the site acts CO₂ sources (1) when density stratification was relaxed (F_{CO2} = 2.1 mmol-C m⁻² d⁻¹); (2) when water was mixed by disturbance such as typhoon (F_{CO2} = 1.3 mmol-C m⁻² d⁻¹); and (3) when it rained (F_{CO2} = 15.5 mmol-C m⁻² d⁻¹).

List of Presentations

at

International Conferences

Presenters are underlined in the list of authors.

†Undergraduate or graduate students of the Faculty of Engineering, Osaka City University

Mechanical Engineering

Optical Control of Structural Transformation to Form Nano-scaled Phases Including sp³-like Interlayer Bonds in Graphite

Eiichi INAMI, Keita NISHIOKA, Jun'ichi KANASAKI, Katsumi TANIMURA

The 15th International Conference on Laser Ablation, Maui-Hawaii, USA, September 8-13, 2019 (poster).

Formation Process of Grain Boundary Steps on Ultra-Precision Cut Surfaces of Polycrystalline Copper and Zinc

T. MIYAGAWA[†], T. TOKUYAMA[†], H. KAWAKAMI, T TANAKA (Osaka Res. Inst. Indust. Sci. Tech.), Y. SATO

ICPE2018 17th International Conference on Precision Engineering, Kamakura, Japan, November 12-16, 2018.

Effects of Heating and Cooling Conditions on Mechanical Property of Stainless steel and Polyamide 6 Specimen under Tensile Test

H. KOBAYASHI[†], M. UCHIDA, H. KITANO and Y. KANEKO

The International Symposium on Joining Technologies in Advanced Automobile Assembly 2018, Kitakyushu, Japan, November 27-28, 2018.

EBSD Analysis on Microstructures Developed near Fracture Surface of a Fatigued Copper Single Crystal Oriented for Single Slip

S. OKA[†], Y. KANEKO, M. UCHIDA

The 14th Asia-Pacific Symposium on Engineering Plasticity and its Applications, Jeju island, Korea, December 2-6, 2018.

Macroscopic and Microscopic Non-uniform Deformations of Polycrystalline Pure Copper during Uniaxial Tensile Test with High Stress Gradient

A. TANIGUCHI[†], T. MAEYAMA[†], M. UCHIDA and Y. KANEKO

The 14th Asia-Pacific Symposium on Engineering Plasticity and its Applications, Jeju island, Korea, December 2-6, 2018.

Evaluation of Effect of Sample Size and Layer Direction on Mechanical Property of Specimen Manufactured by FDM-Type 3D Printer

H. AKIYAMA[†], M. UCHIDA and Y. KANEKO

The 14th Asia-Pacific Symposium on Engineering Plasticity and its Applications, Jeju island, Korea, December 2-6, 2018.

Deformed Structures of Multilayered Thin Films Fabricated by Electrodeposition

Y. KANEKO, T. KUBOMAE[†], M. UCHIDA

4th International Symposium on Long-Period Stacking Order Structures and Mille-feuille Structure, Kumamoto, Japan, December 3-5, 2018.

Electronics and Informatics

Applied Physics and Electronics

International Study of the Longer-lived Chemistry of Plasma Activated Water

Jun-Seok OH, Endre J. SZILI, Robert D. SHORT, Akimitsu HATTA, Mineo HIRAMATSU and Masafumi ITO
12th Asian-European International Conference on Plasma Surface Engineering, Sep. 1-5, 2019, Jeju, Korea (Invited)

Effects of Dielectric Coating of an Internal Electrode for Coaxial-type Plasma/Liquid Interfacial Processes

Hiroki NAKATANI[†], Jun-Seok OH, Tatsuru SHIRAFUJI

12th Asian-European International Conference on Plasma Surface Engineering, September 1-5, 2019, Jeju, Korea (Poster)

Polymerization of EDOT Using Gas-liquid Interfacial Plasma

Ryoga KONISHI[†], Shunta HIRANO[†], Shiori AZUMA[†], Jun-Seok OH, Tatsuru SHIRAFUJI

12th Asian-European International Conference on Plasma Surface Engineering, September 1-5, 2019, Jeju, Korea (Poster)

On the Preparation of Plasma Bullets Passing through a Dielectric Plate

Ryo MATOBA[†], Yuki HAMAMOTO[†], Masato OSHIRO[†], Jun-Seok OH, Ryo SUGAMA (Faculty of Medicine), Kumi ORITA (Faculty of Medicine), Hiromitsu TOYODA (Faculty of Medicine), Tatsuru SHIRAFUJI

12th Asian-European International Conference on Plasma Surface Engineering, September 1-5, 2019, Jeju, Korea (Poster)

Discharge Characteristics of Atmospheric-pressure Plasma Reactor

Soshi IMAI[†], Ikumi TAKAHASHI[†], Yusuke SASAKI[†], Tatsuru SHIRAFUJI and Jun-Seok OH

12th Asian-European International Conference on Plasma Surface Engineering, Sep. 1-5, 2019, Jeju, Korea (Poster)

Plasma-Activated Water Generated by Air Discharge in Atmosphere-Pressure Plasma Reactor

Yusuke SASAKI[†], Kenji MAEDA[†], Tatsuru SHIRAFUJI and Jun-Seok OH

12th Asian-European International Conference on Plasma Surface Engineering, Sep. 1-5, 2019, Jeju, Korea (Poster)

Lifetime of Bactericidal Efficacy in Oxygen-Radical-Activated Phenylalanine Solution

Naoyuki IWATA, Vladislav GAMALEEV, Hiroshi HASHIZIME, Jun-Seok OH, Takayuki OHTA, Kenji ISHIKAWA, Masaru HORI and Masafumi ITO

12th Asian-European International Conference on Plasma Surface Engineering, Sep. 1-5, 2019, Jeju, Korea (Oral)

Effective Treatment of Water by Low-Current Arc in Ambient Air

Vladislav GAMALEEV, Naoyuki IWATA, Jun-Seok OH, Mineo HIRAMATSU and Masafumi ITO

12th Asian-European International Conference on Plasma Surface Engineering, Sep. 1-5, 2019, Jeju, Korea (Oral)

On the Formation of Polymerized EDOT Films Using Gas-liquid Interfacial Plasma

Tatsuru SHIRAFUJI, Shiori AZUMA[†], Jun-Seok OH

34th International Conference on Phenomena in Ionized Gases / 10th International Conference on Reactive Plasmas, July 14-19, 2019, Sapporo, Japan (Poster)

Dynamic Analysis of Reactive Oxygen Nitrogen Species in Plasma-Activated Liquid by UV Absorption Spectroscopy

Jun-Seok OH, Endre J. SZILI, Masafumi ITO, Akimitsu HATTA

Joint Conference of XXXIV International Conference on Phenomena in Ionized Gases (XXXIV ICPIG) and the 10th International Conference on Reactive Plasmas (ICRP-10), Jul. 14-19, Sapporo, Japan (Invited)

Generation of Bactericidal Efficacy in Neutral pH Range Using Oxygen-Radical Treatment of Organic Compound

Naoyuki IWATA, Vladislav GAMALEEV, Hiroshi HASHIZIME, Jun-Seok OH, Takayuki OHTA, Kenji ISHIKAWA, Masaru HORI and Masafumi ITO

Joint Conference of XXXIV International Conference on Phenomena in Ionized Gases (XXXIV ICPIG) and the 10th International Conference on Reactive Plasmas (ICRP-10), Jul. 14-19, Sapporo, Japan (Oral)

Influence of DC Substrate Bias Voltage on Deposition of Carbon Nanoparticles Produced by Ar+CH₄ Multi-Hollow Discharge Plasma CVD method

Sung-Hwa HWANG, Kunihiko KAMATAKI, Naho ITAGAKI, Kazunori KOGA, Masaharu SHIRATANI, Jun-Seok OH and Tatsuyuki NAKATANI

Joint Conference of XXXIV International Conference on Phenomena in Ionized Gases (XXXIV ICPIG) and the 10th International Conference on Reactive Plasmas (ICRP-10), Jul. 14-19, Sapporo, Japan (Oral)

Analysis of Concentrations of Species Generated by Rotating Arc Jet in Gas Phase and Treated Liquid

Vladislav GAMALEEV, Naoyuki IWATA, Jun-Seok OH, Mineo HIRAMATSU and Masafumi ITO

Joint Conference of XXXIV International Conference on Phenomena in Ionized Gases (XXXIV ICPIG) and the 10th International Conference on Reactive Plasmas (ICRP-10), Jul. 14-19, Sapporo, Japan (Poster)

DC-Pulse Driven Plasma Jet Modulating Reactive Oxygen and Nitrogen Species

Jun-Seok OH, Endre J. SZILI, Akimitsu HATTA, Masafumi ITO and Tatsuru SHIRAFUJI

International Forum on Functional Materials (IFFM) 2019, June 23-26, Gangneung, Korea (Invited)

Free Standing Functional Membrane Formation Using Plasma-liquid Interface Processes

Tatsuru SHIRAFUJI

Awaji Island Conference on Electron Spin Science & Technology 2019, June 16-19, 2019, Awaji, Japan (Invited)

Non-Thermal Atmospheric Pressure Plasma Generated Reactive Species Delivery into Biological Systems

Jun-Seok OH, Endre J. SZILI, Hideo FUKUHARA, Keiji INOUE, Robert D. SHORT, Akimitsu HATTA, Masafumi ITO and Tatsuru SHIRAFUJI

the 6th Awaji International Workshop on "Electron Spin Science & Technology: Biological and Materials Science Oriented Applications, June 16-19, Hyogo, Japan (Invited)

Pressure Gradient Sputtering Technology (PGS: High Vacuum Sputtering)

Ken YONEZAWA, Hiroki OOTA, Jun-Seok OH, Kazunori KOGA, Tatsuyuki NAKATANI, Masafumi ITO and Masaharu SHIRATANI

The 15th International Symposium on Sputtering and Plasma Processes (ISSP 2019), June 11-14, Kanazawa, Japan (Poster)

Materials Processing by Efficient Utilization of Plasma-liquid Interface

Tatsuru SHIRAFUJI

24th International Symposium on Plasma Chemistry, June 9-14, 2019, Napoli, Italy (Invited)

Novel Bactericidal Method for Aquaculture Using Benzoic-Compound Solutions Treated with Oxygen Radicals

Naoyuki IWATA, Vladislav GAMALEEV, Jun-Seok OH, Hiroshi HASHIZIME, Takayuki OHTA, Kenji ISHIKAWA, Masaru HORI and Masafumi ITO

24th International Symposium on Plasma Chemistry (ISPC24), June 9-14, Naples, Italy (Oral)

Bactericidal Activity in Oxygen-Radical-Activated Water

Naoyuki IWATA, Vladislav GAMALEEV, Jun-Seok OH, Kenji ISHIKAWA, Masaru HORI and Masafumi ITO

24th International Symposium on Plasma Chemistry (ISPC24), June 9-14, Naples, Italy (Poster)

How the Cell Membrane Composition Influences Plasma-Induced Cellular Effects

Jonas Van der PAAL, Sung-Ha HONG, Maksudbek YUSUPOV, Nishta GAUR, Jun-Seok OH, Annemie BOGAERTS, Endre SZILI

24th International Symposium on Plasma Chemistry (ISPC24), June 9-14, Naples, Italy (Oral)

3D Numerical Simulation of APPJ on the Flowing Water Surface

Tatsuru SHIRAFUJI, Jun-Seok OH, Masafumi ITO (Meijo Univ.)

10th International Workshop on Microplasmas, May 20-24, 2019, Kyoto, Japan (Poster)

Microplasma Jet Contributes to Investigation of RONS Chemistry of Plasma-Activated Water

Jun-Seok OH and Tatsuru SHIRAFUJ

10th anniversary of International Workshop on Microplasmas, May 20-24, Kyoto, Japan (Oral)

Functional Thin Film Formation Localized at Plasma/Liquid Interface: A New Perspective of Plasma Polymerization, Dedicated to Prof. Riccardo d'Agostino (June 17, 1942-April 21, 2018)

Tatsuru SHIRAFUJI

11th International Symposium on Advanced Plasma Science and its Applications for Nitrides and Nanomaterials /
12th International Conference on Plasma-Nano Technology & Science, March 17-21, 2019, Nagoya, Japan (Invited)

The Influence of Pulse Voltage Polarity on Au-nanoparticle-embedded Film Formation on Aqueous Solution in Contact with DBD

Shunta HIRANO[†], Shiori AZUMA[†], Yusuke NAKAMURA[†], Toshiyuki ISSHIKI (Kyoto Inst. Technol.), Jun-Seok. OH, Tatsuru SHIRAFUJI

11th International Symposium on Advanced Plasma Science and its Applications for Nitrides and Nanomaterials /
12th International Conference on Plasma-Nano Technology & Science, March 17-21, 2019, Nagoya, Japan (Poster)

The Performance of Three-dimensionally Integrated Micro Solution Plasma Assisted with Argon Micro-bubble

Reiya NAKAGAWA[†], Hiroto MASUNAGA[†], Jun-Seok OH, Tatsuru SHIRAFUJI

11th International Symposium on Advanced Plasma Science and its Applications for Nitrides and Nanomaterials /
12th International Conference on Plasma-Nano Technology & Science, March 17-21, 2019, Nagoya, Japan (Poster)

The APPJ Treatment for Improving Water Permeability of a Bone-regeneration Scaffold with Grounded Electrode

Yuki HAMAMOTO[†], Masato OSHIRO[†], Jun-Seok OH, Kumi ORITA (Faculty of Medicine), Hiromitsu TOYODA (Faculty of Medicine), Tatsuru SHIRAFUJI

11th International Symposium on Advanced Plasma Science and its Applications for Nitrides and Nanomaterials /
12th International Conference on Plasma-Nano Technology & Science, March 17-21, 2019, Nagoya, Japan (Poster)

Simultaneous Achievement of Bactericidal Efficacy and Plant-growth in Neutral pH Range using Radical-Activated Benzoic Compounds

Naoyuki IWATA, Vladislav GAMALEEV, Jun-Seok OH, Hiroshi HASHIZIME, Takayuki OHTA, Kenji ISHIKAWA, Masaru HORI and Masafumi ITO

11th International Symposium on Advanced Plasma Science and its Applications for Nitrides and Nanomaterials /
12th International Conference on Plasma-Nano Technology and Science, March 17-21, Nagoya, Japan (Oral)

International Study of Plasma Activated Water: Chemical Composition of RONS

Jun-Seok OH, Endre SZILI, Rrobert SHORT, Akimitsu HATTA, Mineo HIRAMATSU and Masafumi ITO

11th International Symposium on Advanced Plasma Science and its Applications for Nitrides and Nanomaterials /
12th International Conference on Plasma-Nano Technology and Science, March 17-21, Nagoya, Japan (Oral)

Measurement of Water Cluster Ions in Plasma Plume of an Atmospheric Pressure He Plasma Jet

Jun-Seok OH, Yoshihiro NAKAI, Toshiyuki KAWASAKI, Tatsuru SHIRAFUJI, Masaru HORI, Mineo HIRAMATSU and Masafumi ITO

40th International Symposium on Dry Process (DPS2018), Nov. 13-15, Nagoya, Japan (Poster)

Analysis of Radical-Treated Amino Acid Using UV Absorption Spectroscopy for Plasma-Medical Application

Noyuki IWATA, Hiroshi HASHIZUME, Jun-Seok OH, Masaru HORI and Masafumi ITO

40th International Symposium on Dry Process (DPS2018), Nov. 13-15, Nagoya, Japan (Poster)

Terahertz Emission from Coherent Longitudinal Optical (LO) Phonons and LO-phonon-plasmon Coupled modes in a Low-Temperature-Grown GaAs Epitaxial Layer

Hideo TAKEUCHI, Takuya NISHIMURA[†], Masaaki NAKAYAMA, Andra CHEN, Richard L. FIELD, III, and Rachel S. GOLDMAN
The 21st International Conference on Electron Dynamics in Semiconductors, Optoelectronics and Nanostructures (EDISON21), Nara Japan (July 14 – 19, 2019)

Applied Chemistry and Bioengineering

Hydrogen Reduction Synthesis of Lithium Titanium Oxides as a High Rate Electrode without Conductive Additive

K. ARIYOSHI, T. INO[†], Y. YAMADA

The 22th International Symposium on Batteries, Fuel Cells and Capacitors, Osaka, November 27-29, 2018

Preparation of Mesoporous Assemblies Composed of Prussian Blue Nanospheres

S. YOROZU[†], M. YAMANE[†], H. TABE, Y. YAMADA

The 10th OCARINA International Symposium, Osaka, Japan, March 5-6, 2019 (poster)

Synthesis of Coordination Polymers Involving 1,10-phenanthroline-5,6-diolate Iron(III) Complex as a Monomer Unit

Y. KIMOTO[†], H. TABE, Y. YAMADA

The 10th OCARINA International Symposium, Osaka, Japan, March 5-6, 2019 (poster)

Structure Analyses of the Solid Organic Molecule Hydrogen Peroxide Adducts

M. MAETANI[†], H. TABE, Y. YAMADA

The 10th OCARINA International Symposium, Osaka, Japan, March 5-6, 2019 (poster)

Immobilization of Enzymes in a Bottom-up Mesoporous Silica Nanoparticles Assembly

H. OSHIMA[†], H. TABE, S. IKEYAMA, Y. AMAO, Y. YAMADA

The 10th OCARINA International Symposium, Osaka, Japan, March 5-6, 2019 (poster)

pH-dependent Catalytic Activity of Prussian Blue Analogs with CN-deficient Sites for Hydrolysis of Organophosphates

M. YAMANE[†], H. TABE, Y. YAMADA

The 10th OCARINA International Symposium, Osaka, Japan, March 5-6, 2019 (poster)

High Stability of Ir(OH)₃ Supported on a Bottom-Up Mesoporous Silica During Photocatalytic Water Oxidation

G. SAKAMOTO[†], H. TABE, Y. YAMADA

The 10th OCARINA International Symposium, Osaka, Japan, March 5-6, 2019 (poster)

Catalytic Activity of Cyano-Bridged Polynuclear Metal Complexes for Organophosphate Hydrolysis

Y. YAMADA

World Chemistry Forum 2019, Barcelona, Spain, May 22-24, 2019

High Stability of Ir(OH)₃ Supported on a Bottom-up Mesoporous Silica for Photocatalytic Water Splitting

G. SAKAMOTO[†], H. TABE, Y. YAMADA

3rd Young Meeting of the International Solar Fuels Conference, Hiroshima, Japan, November 19-20, 2019 (poster)

Immobilization of Enzymes in a Bottom-up Mesoporous Silica Nanoparticles Assembly to Enhance Catalytic Activity and Recyclability

H. OSHIMA[†], H. TABE, S. IKEYAMA, Y. AMAO, Y. YAMADA

3rd Young Meeting of the International Solar Fuels Conference, Hiroshima, Japan, November 19-20, 2019 (poster)

Photocatalytic H₂-evolution Systems Constructed in Porous Protein Crystals

H. TABE, H. TAKAHASHI[†], S. ABE, T. UENO, Y. YAMADA

3rd Young Meeting of the International Solar Fuels Conference, Hiroshima, Japan, November 19-20, 2019

Subsurface Contribution to Photocatalytic Water Oxidation Catalysis of Cyano-bridged Coordination Polymer Nanoparticles

H. TABE, A. KITASE[†], Y. YAMADA

3rd International Solar Fuels Conference and International Conference on Artificial Photosynthesis-2019, Hiroshima, Japan, November 20-24, 2019

Workshop Instructor on “Micro and Energy Dispersive XRF”

K. TSUJI

68th Annual Conference on Applications of X-ray Analysis Denver X-ray Conference, Lombard, Illinois, U.S.A., August 5-9, 2019 (invited)

Workshop Instructor on “Trace Analysis”

K. TSUJI

68th Annual Conference on Applications of X-ray Analysis Denver X-ray Conference, Lombard, Illinois, U.S.A., August 5-9, 2019 (invited)

Scanning and Full Field X-Ray Fluorescence Imaging with Laboratory X-ray Source

K. TSUJI, M. NAKANISHI[†], R. OZEKI[†], T. MATSUYAMA

PSA-19, 8th International Symposium on Practical Surface Analysis, Hokkaido, Japan, November 3-8, 2019 (invited)

Total Reflection X-Ray Fluorescence Analysis Using Carbon Coated Glass Substrate

K. TSUJI, S. MURAKAMI[†], T. MATSUYAMA

18th International Conference on Total Reflection X-ray Fluorescence Analysis and Related Methods (TXRF2019), Girona, Spain, June 25-28, 2019

Full Field Energy Dispersive X-Ray Fluorescence Imaging Under Glancing Incidence Condition

K. TSUJI, A. YAMAUCHI, T. MATSUYAMA

18th International Conference on Total Reflection X-ray Fluorescence Analysis and Related Methods (TXRF2019), Girona, Spain, June 25-28, 2019 (poster)

Trace Elemental Analysis of High Matrix Samples with Total Reflection X-Ray Fluorescence Spectrometry

H. TAKAHARA, W. MATSUDA, Y. KUSAKABE, A. OHBUCHI, S. IKEDA, N. KAWAHARA[†], T. FURUSATO[†], K. TSUJI

18th International Conference on Total Reflection X-ray Fluorescence Analysis and Related Methods (TXRF2019), Girona, Spain, June 25-28, 2019

Rapid and Effective Sample Preparation for TXRF Analysis of Drinking Water Containing Uranium at Reference Level of Risk

T. MATSUYAMA, Y. IZUMOTO, Y. SAKAI, K. TSUJI, H. YOSHII

18th International Conference on Total Reflection X-ray Fluorescence Analysis and Related Methods (TXRF2019), Girona, Spain, June 25-28, 2019

TXRF Analysis Using Carbon Coated Glass Substrate in Comparison with Conventional Sample Preparation

T. MATSUYAMA, H. YOSHI, K. TSUJI

68th Annual Conference on Applications of X-ray Analysis Denver X-ray Conference, Lombard, Illinois, U.S.A., August 5-9, 2019

Full Field Energy Dispersive X-Ray Fluorescence Imaging and Compressed Sensing Analysis for Super-Resolution Analysis

K. TSUJI, A. YAMAUCHI, T. MATSUYAMA

68th Annual Conference on Applications of X-ray Analysis Denver X-ray Conference, Lombard, Illinois,

U.S.A., August 5-9, 2019 (poster)

Confocal Line XRF Analysis in Comparison with Confocal Point Micro XRF Analysis

T. MATSUYAMA, S. SONODA[†], H. NAKANO[†], K. TSUJI

68th Annual Conference on Applications of X-ray Analysis Denver X-ray Conference, Lombard, Illinois, U.S.A., August 5-9, 2019 (poster)

Controlled Degradation of Polyperoxides for Application to High Performance Dismantlable Adhesives

Eriko SATO

An International Conference on Colloid & Surface Science (Okinawa Colloids 2019), Okinawa, Japan, November 3-8, 2019 (invited)

Monofunctional Dual Stimuli-Responsive Organogels: Thermo- and Photo-Responsive Behavior of Coumarin Polymer-Based Organogel

Seidai OKADA[†], Eriko SATO, Yuta KODA, Hideo HORIBE

An International Conference on Colloid & Surface Science (Okinawa Colloids 2019), Okinawa, Japan, November 3-8, 2019 (oral and poster)

Cononsolvency and Thermo-Responsive Behavior of Coumarin Derivative Polymers in Non-Hydrogen Bonding Organic Solvents

Seidai OKADA[†], Eriko SATO

2nd G'Lowing Polymer Symposium in KANTO (GPS-K 2019), Tokyo, Japan, November 30, 2019

Controlled Reductive Decomposition of Alternating Copolymers of Oxygen and Dienes Having Different Regioselectivity and Their Application to Debondable Adhesives

Eriko SATO

The 16th Pacific Polymer Conference (PPC-16), Suntec, Singapore, December 8-12, 2019 (invited)

Photoinduced Shape Change of Crystals Composed of a Diarylethene with a Long Alkyl Chain

Takuya HIGASHIGUCHI[†], Daichi KITAGAWA, Seiya KOBATAKE

10th OCARINA International Symposium, Osaka, Japan, March 5-6, 2019 (poster)

Photoluminescence Switching of Quantum Dot Coated with Diarylethenes by Photochromic Reaction

Yuya SETO[†], Daichi KITAGAWA, DaeGwi KIM, Seiya KOBATAKE

10th OCARINA International Symposium, Osaka, Japan, March 5-6, 2019 (poster)

Bright and Tunable Emission of BODIPY in Solid State

Katsuya SHIMIZU[†], Seiya KOBATAKE

10th OCARINA International Symposium, Osaka, Japan, March 5-6, 2019 (poster)

Unusual Photomechanical Behavior of Photochromic Diarylethene Crystals

Seiya KOBATAKE

24th International Conference on the Chemistry of the Organic Solid State (ICCOSS XXVI 2019), New York, U.S.A., June 16-21, 2019 (invited)

Effect of Illumination Conditions on Photomechanical Response of Diarylethene Crystals

Daichi KITAGAWA, Seiya KOBATAKE

24th International Conference on the Chemistry of the Organic Solid State (ICCOSS XXVI 2019), New York, U.S.A., June 16-21, 2019

Mechanism of Photoinduced Birefringence Change in Diarylethene Single Crystals

Kohei MORIMOTO[†], Hajime TSUJIOKA[†], Daichi KITAGAWA, Seiya KOBATAKE

24th International Conference on the Chemistry of the Organic Solid State (ICCOSS XXVI 2019), New York, U.S.A., June 16-21, 2019 (poster)

Photo-Functional Materials using Photochromic Diarylethenes

Daichi KITAGAWA

Inner Mongolia-Japan International Joint Research: Functional Molecular Chemistry Lecture Meeting, Inner Mongolia, China, August 21-22, 2019 (invited)

Irradiation Method Dependence of Photoinduced Shape Change of Diarylethene Crystals

Seiya KOBATAKE, Daichi KITAGAWA, Akira HIRANO[†]

9th International Symposium on Photochromism (ISOP2019), Paris, France, September 23-27, 2019

Synthesis and Fluorescence Switching of Hyper-Branched Polymers Having Diarylethene at Branching Point

Katsuya SHIMIZU[†], Rémi MÉTIVIER (ENS Paris-Saclay), Seiya KOBATAKE

9th International Symposium on Photochromism (ISOP2019), Paris, France, September 23-27, 2019 (poster)

Development of Novel Photomechanical Phenomena of Photoresponsive Molecular Crystals by High-order Photoexcitation

Seiya KOBATAKE

Final International Symposium on Photosynergetics, Osaka, Japan, October 23-26, 2019

One-step optical resolution of alanine by preferential crystallization combined with enzymatic racemization

T. FUJIMURA[†], and K. IGARASHI

18th Asian Pacific Confederation of Chemical Engineering (APCChE) Congress, Sapporo, Japan, September 27-27, 2019 (oral and poster)

Enhancement of crystal nucleation of L-alanine by plastic piece moving in the solution

M. HANADA[†], T. KOBAYASHI, and K. IGARASHI

18th Asian Pacific Confederation of Chemical Engineering (APCChE) Congress, Sapporo, Japan, September 27-27, 2019 (oral and poster)

Small scale continuous crystallizer to produce uniform small crystals

A. OKADA[†], H. OOSHIMA and K. IGARASHI

18th Asian Pacific Confederation of Chemical Engineering (APCChE) Congress, Sapporo, Japan, September 27-27, 2019 (oral and poster)

Functional Evaluation of Kojic Acid Modified Carborane Developed as a Boron Drug for Melanoma BNCT

Satoshi DOWAKI[†], Koki MATSUURA[†], Riku KAWASAKI[†], Yoshihide HATTORI, Yoshinori SAKURAI, Shin-ichiro MASUNAGA, Mitsunori KIRIHATA, and Takeshi NAGASAKI

The 18th International Congress on Neutron Capture Therapy, Taipei, Taiwan, October 28-November 2, 2018; Preprints.

Cellular Uptake Mechanism of Kojic Acid Modified o-Carborane as a Boron Drug toward Melanoma-Targeting BNCT

Takeshi NAGASAKI, Satoshi DOWAKI[†], Riku KAWASAKI[†], Yoshihide HATTORI, Yoshinori SAKURAI, Shin-ichiro MASUNAGA, and Mitsunori KIRIHATA

The 10th Young Researchers BNCT Meeting, Helsinki, Finland, September 26- September 29, 2019; Preprints.

Maximum oxygen transfer capacity with different shaking diameters in elevated viscosity media

Yoshihiro OJIMA, René HANKE (RWTH Aachen University), David WOLLBORN (RWTH Aachen University), Jochen BÜCHS (RWTH Aachen University)

18th Asian Pacific Confederation of Chemical Engineering Congress (APCChE 2019), K313, Sapporo, Japan, September 23-27, 2019

Identification and analyses of cell surface proteins involved in emulsification and macrophage activation from *Saccharomyces cerevisiae*

Mana UEDA[†], Daiki SAITO[†], Yoshihiro OJIMA, Masayuki AZUMA
18th Asian Pacific Confederation of Chemical Engineering Congress (APCCChE 2019), PL328, Sapporo, Japan, September 23-27, 2019 (Poster)

Efficient formation of *Escherichia coli* flocs by glycerol addition

Hiroaki HOMMA[†], Mio OTSUKA[†], Yoshihiro OJIMA, Masayuki AZUMA
18th Asian Pacific Confederation of Chemical Engineering Congress (APCCChE 2019), PL329, Sapporo, Japan, September 23-27, 2019 (Poster)

Promoted secretory protein production by constructing hyper-vesiculation strains of *Escherichia coli*

Tomomi SAWABE[†], Katsuya KONAMI[†], Yoshihiro OJIMA, Masayuki AZUMA
The 14th Asian Congress on Biotechnology (ACB2019), P2-122, Tamsui, Taiwan, July 1-4, 2019 (Poster)

Construction of superior catalyst suitable for microbial fuel cell and effect of anode composition on power of the fuel cell

Ryota KIKUCHI[†], Taichi KAWAGUCHI[†], Daisuke KOMA (Osaka Research Institute of Science and Technology), Takashi OHMOTO (Osaka Research Institute of Science and Technology), Yoshihiro OJIMA, Masayuki AZUMA
The 14th Asian Congress on Biotechnology (ACB2019), P2-143, Tamsui, Taiwan, July 1-4, 2019 (Poster)

Increased poly- γ -glutamic acid production by disruption of *ggt* gene in *Bacillus licheniformis* RK14-46 strain and its application for flocculation of real sewage sludge

Yoshihiro OJIMA, Joji KOBAYASHI[†], Masayuki Azuma
The 14th Asian Congress on Biotechnology (ACB2019), S17-04, Tamsui, Taiwan, July 1-4, 2019

Urban Engineering

Urban Design and Engineering

A Study on the Effect of Motorcycle Traffic Safety Workshop for High School and University Students in Phnom Penh, Cambodia

Toshiki KOYANAGI, Nagahiro YOSHIDA, and Yuto KITAMURA (The University of Tokyo)
Transportation Research Board, Washington, D.C., The United States of America, 13-17 January 2019.

Latent Opportunities for Two-rider Bicycles and Associated Challenges based on Assessments of its Use by People with Reduced Mobility

Nagahiro YOSHIDA
VELO-CITY GLOBAL 2019, Dublin, Ireland, 25-28 June 2019. (Poster Session)

Changes in Subjective and Objective Comfort for Pedestrians and Cyclists After Road-Space Reallocation: A Case Study of Midosuji, Osaka

Nagahiro YOSHIDA, Haruka KAWACHI[†], Pola BERENT (University College London), and Taku FUJIYAMA (University College London)
The 13th International Conference of the Eastern Asia Society for Transportation Studies (EASTS), Colombo, Sri Lanka, 9-12 September 2019.

Evaluation of Road Space Reallocation for Pedestrians and Cyclists Using the Level of Service Concept on Midosuji Street in Japan

Haruka KAWACHI[†], Nagahiro YOSHIDA, and Atsushi TAKIZAWA
The 20th International Walk21 Conference on Walking and Liveable Communities, Rotterdam, Netherlands, 7-10 October 2019.

The relationship between businesses' handled amount and released/transferred amount of chemical substances according to the PRTR system

Satoshi MIZUTANI, Ryusuke SUGIURA[†], Satoshi NAKAMURA, Yoshinori YABUKI, Yusuke TAWA, Kazushi NORO, Yoshinori KANJO
Proc. of the 5th 3R International Scientific Conference on Material Cycles and Waste Management (3RINCs), Bangkok, Thailand, 27-28 February, 1 March 2019

An Experimental Study on the Interaction between Oscillatory Flow and Idealized Porous Bed

Takaaki SHIGEMATSU, Sota NAKAJO, Yuya OKADA
The 15th International Coastal Symposium (ICS), Busan, Republic of Korea, 13th-18th May, 2018.

Morphological Changes at the Mouth of the Shirakawa River after Kumamoto Earthquake

Ryota YAMAGUCHI, Gozo TSUJIMOTO, Takaomi HOKAMURA, Sota NAKAJO, Ngoc Than NGUYEN
The 28th International Ocean and Polar Engineering Conference, Sapporo, Japan, 10th-15th June, 2018.

Sensitivity of Tropical Cyclone Track to Assessment of Severe Storm Surge Event at Tokyo Bay

Sota NAKAJO, Hideyuki FUJIKI, Sooyoul KIM, Nobuhito MORI
The 36th Conference on Coastal Engineering, Baltimore, Maryland, 30th July-3rd August, 2018.

Turbulent Flow Induced by Oscillating Circular Cylinder Arrays

Takaaki SHIGEMATSU and Hiroshi Matsumoto
The 36th Conference on Coastal Engineering, Baltimore, Maryland, 30th July-3rd August, 2018.

Projection of Future Change in Storm Surges by Artificial Neural Network and d4PDF

Yuji ARAKI, Tomohiro YASUDA, Nobuhito MORI, Sota NAKAJO
The 15th Annual Meeting Asia Oceania Geosciences Society, Honolulu, Hawaii, 3rd-8th June, 2018

Modelling the life cycles of harmful diatoms and its application to the benthic-pelagic coupled ecosystem model, to reveal the mechanisms of the bleaching in aquacultured nori

Akio SOHMA, Riku IMADA[†], Tetsuya NISHIKAWA (Hyogo Prefectural Technology Center for Agriculture, Forestry and Fisheries), Hisashi SHIBUKI (Mizuho Information and Research Inst.)
Proc. of the international Society for Ecological Modelling Global Conference 2019, GEN01.04, Salzburg, AUSTRIA (2019.10) (on WEB)

Estimation on spatial distribution and ecosystem network of ayu *Plecoglossus altivelis altivelis* in the inner part of Osaka Bay

Toru ENDO, Kentaro HIRANO[†], Sosuke OTANI, Ryoichi YANAGAWA, Yasunori KOZUKI
12th International Conference on the Environmental Management of Enclosed Coastal Seas, Pattaya, Thailand, November 4-8, 2018. (poster)

Air-Sea CO₂ Exchange and Dissolved Inorganic Carbon Distribution in an Inner Part of Osaka Bay, Japan

Toru ENDO, Junpei SHIMAN, Noriko HARADA[†], Daiki SAKAI, Ryuichi FUJIWARA
10th International Conference on Asian and Pacific Coasts, 2019, Hanoi Vietnam, September 25-28, 2019.

This is the final print issue of “*Memoirs of the Faculty of Engineering, Osaka City University.*” This series of *Memoirs* has been published for the last decade in print edition as well as in electronic edition. From the next issue, the *Memoirs* will be published only electronically. The forthcoming issues will be available at the internet address: <https://www.eng.osaka-cu.ac.jp/en/about/publication.html>. The past and present editors take this opportunity to express gratitude to the subscribers for all their support and hope them to keep interested in the *Memoirs*.

